NTNU
Norwegian University of
Science and Technology

2D experimental and numerical study of moonpool with recess

Sebastian Erik Eriksson

Marine Technology
Submission date: June 2018
Supervisor: Trygve Kristiansen, IMT
Co-supervisor: Babak Ommani, SINTEF Ocean AS

Norwegian University of Science and Technology
Department of Marine Technology

Preface

This thesis is the final part of my master's degree in Marine Technology, with specialization within Marine Hydrodynamics. The thesis is written during the spring semester of 2018, at the Department of Marine Technology(IMT) at the Norwegian University of Technology and Science(NTNU), Trondheim. The work has been done under the supervision of Professor Trygve Kristiansen, and the workload of the thesis corresponds to 30 ECTS.

During this master's thesis project, I have got the opportunity to investigate various interesting elements of hydrodynamics. I have been able to discover how experimental, numerical and analytical tools can be combined and utilized together.

Trondheim, 2018-06-11

Sebastian Erik Eriksson

Acknowledgment

I would like to thank Professor Trygve Kristiansen for excellent advice and guidance as my supervisor during this master's project. Sharing of his knowledge and understanding of hydrodynamics has been greatly appreciated.

I would also like to thank my co-supervisor Babak Ommani for helping me set up the numerical simulations.

Gratitudes are also due to Professor Bernard Molin, for constructive advice on the methods of matched eigenfunction expansions.

Through meaningful conversations, I have received valuable advice from PhD candidate Senthuran Revinthrakumar, and this I am thankful for.

For my two periods in the laboratory, I want to express my gratitude to the lab personnel for helping me rigging my experiments. Special mention goes to Torgeir Wahl, Terje Rosten, Trond Innset and Ole Vinje.

S.E.E

Abstract

The background for this master's thesis is the complications that is faced in the industry with regards to operational time inside moonpools. This thesis focuses on moonpools with recess, and the fluid resonant phenomena piston mode and sloshing. The main idea is that recess length, water depth in the shallow water zone above the recess and heave amplitude are important parameters. Strengths of model experiments, numerical simulations and potential theory is utilized.

In order to establish an overview of the background of this thesis, relevant work carried out by others are presented through a literature review. Relevant theory is presented, and special attention is paid to potential theory. In detail the methods of matched eigenfunction expansions are described. The theory presented by Molin (2017) is utilized and adapted in order to match the present experimental setup investigated. Expressing the velocity potential in three subdomains by means of eigenfunction expansions, yields an eigenvalue problem providing estimates of the natural periods of piston mode and sloshing modes. These are used to construct compact experimental test matrices, and are also compared against experimental results. Findings show that the estimated natural periods are somewhat smaller than the ones obtained from experiments. A similar approach is used in order to implement the theory in six subdomains. This yields a boundary value problem in which results like Response Amplitude Operators(RAO) are obtained.

Two-dimensional forced heave experiments are conducted over two lab periods in the NTNU laboratory Ladertanken. Experiments are executed around piston mode and the first sloshing mode natural periods. Results indicate a strong dependency of draft on the linearity of the free surface in the shallow water zone above the recess. Results show that strong second harmonic oscillations are excited, and discussions are made on the applicability of theory on shallow and intermediate water sloshing in tanks with secondary resonance. Together with draft, recess length prove to be an important factor. The largest second harmonic response is obtained for recess length of half the moonpool length, at the shallowest drafts. The largest amplification of the first harmonic response is obtained for the second largest draft, with recess length of half the moonpool length. Strong viscous effects are observed with regards to forcing amplitude. Small resonance amplitudes are observed at piston mode resonance, which is consistent with similar experiments on clean moonpools.

Numerical simulations are carried out in OpenFOAM by implementing the hybrid code Potential Viscous Code 3D(PVC3D) developed at SINTEF Ocean. As the free surface is governed by linear potential flow conditions, investigations are made on its applicability in the shallow water zone above the recess. Numerical results are compared with experiments, and good correspondence are found for the largest draft tested with a deviation of 2.18%. A brief refinement investigation is carried out, showing a clear mesh dependency on the accuracy. The code is also tested for more shallow drafts, and results indicates that the non-linearities are problematic for the solver. Neither the first or second harmonic signals are captured with satisfactory accuracy.

Sammendrag

Bakgrunnen for denne masteroppgaven er utfordringene opplevd i industrien, med resonansproblematikk i forbindelse med moonpooloperasjoner. Denne oppgaven tar for seg moonpool med recess, og resonansfenomen som piston mode og sloshing. Hovedideene baserer seg på at parametere som recesslengde, vanndyp i gruntvannsonen og hivamplitude er viktige. Styrker fra modellforsøk, numeriske simuleringer og potensialteori blir anvendt.

For å gi leseren et overblikk over relevant arbeid på hovedtemaene til denne oppgaven, blir et litteratursøk presentert. Følgelig blir relevant teori presentert, med fokus på potensialteori. Spesielt blir metoder innen matchede egenfunksjonsekspansjoner beskrevet. Teorien presentert av Molin (2017) blir anvendt, og tilpasset til det eksperimentelle tilfellet denne oppgaven undersøker. Ved å uttrykke hastighetspotensialene i tre ulike subdomener ved hjelp av egenfunksjonsekspansjoner, finnes estimater for egenperioder i piston mode og sloshemoder ved å løse et egenverdiproblem. Disse estimatene brukes til å konstruere kompakte forsøksmatriser, og estimatene sammenlignes mot eksperimentelle resultat. Resultat viser at de estimerte egenperiodene generelt er litt lavere enn de eksperimentelle. En tilsvarende metode beskrives også for seks subdomener. Denne metoden tar hensyn til fluidet utenfor modellen, og gir følgelig et grenseverdiproblem med resultater i form av RAOer.

Todimensjonale eksperiment i tvungen hiv er gjennomført over to labperioder i NTNU sitt laboratorium Ladertanken. Eksperimentene er konsentrert rundt egenperiodene i piston mode og første sloshemode, og resultatene viser en sterk avhengighet av dypgang på lineariteten av vannoverflaten i gruntvannssonen over recessen. Sterke andre-harmoniske oscillasjoner blir eksitert, og det blir diskutert hvorvidt teori om gruntvannssloshing i rektangulære tanker med sekundær resonans er anvendbar. Sammen med dypgang, viser lengde av recess seg som en viktig faktor. De sterkeste andre-harmoniske responsene oppnås med recesslengde lik halve moonpoollengden ved de laveste dypgangene. Den største amplifikasjonen av første-harmonisk responsamplitude er observert ved nest størst dypgang og recess lengde lik halve moonpoollengden når første sloshemode er eksitert. Med hensyn til eksitasjonsamplitude i hiv, vises sterk viskøs avhengighet på resonansamplituder i RAOer. Små resonansamplituder observeres ved piston mode resonans, i samsvar med tilsvarende forsøk på moonpool uten recess.

Numeriske simuleringer er gjennomført i OpenFOAM ved bruk av hybridkoden PVC3D utviklet ved SINTEF Ocean. Siden den frie vannoverflaten er beskrevet av lineær potensialteori, blir anvendeligheten av koden i gruntvannssonen undersøkt. Numeriske resultater er sammenlignet med eksperimentelle resultat, og tilfredsstillende samsvar oppnås for den største undersøkte dypgangen med avvik på 2.18%. Nøyaktigheten i simuleringene viser en klar avhengighet av raffineringsnivå av det numeriske gridet. Ved lavere dypganger vises det at PVC3D ikke samsvarer godt nok med eksperiment, noe som tyder på at koden har problemer med de sterke ikke-linearitetene. Verken første eller andre-harmoniske signaler beskrives med tilfredsstillende nøyaktighet.

Contents

Nomenclature

Acronyms

BEM	Boundary Element Method
CFD	Computational Fluid Dynamics
DLF	Dynamic Load Factor
DOF	Degrees of Freedom
FDPSO	Floating, Drilling, Production, Storage and Offloading
FFT	Fast Fourier Transform
FVM	Finite Volume Method
PVC3D	Potential Viscouse Code 3D
RAO	Response Amplitude Operator
STL	Stereolithography
VOF	Volume of Fluid

Greek Letters

β	Standard deviation of band-pass filter
η_{osc}	Heave forcing amplitude
γ	Cubic stiffness parameter
μ	Dynamic viscocity
ω_n	Natural frequency
ϕ	Velocity potential
ρ	Water density
σ_i	Natural frequency of mode i

ζ_a	Wave amplitude

Roman Letters

$\mathbf{V}$	Velocity vector
A_M	Model water line area
A_T	Tank water line area
C_g	Group velocity
H_R	Height of recess
L_B	Length of hull box
L_G	Length of moonpool gap
L_R	Length of recess
L_T	Tank length
W_B	Width of hull box
W_T	Tank width
g	Acceleration of gravity
P	Pressure
Q	Source strength
r	Radial distance
u	x-component of velocity vector $\mathbf{V}$
v	y-component of velocity vector $\mathbf{V}$
w	z-component of velocity vector $\mathbf{V}$

Chapter 1

Introduction

Due to harsh sea and weather conditions, there are in some cases a need for shelter when executing certain operations at sea. Some vessels are equipped with a moonpool to enable lowering and diving operations in calmer environment. A moonpool is a vertical opening on the vessel, giving access to the free surface. The physics of a moonpool are similar to those in between multiple hulls on a vessel, or between a tanker and a LNG-terminal for instance. In some cases, a moonpool is combined with a shallow water working zone, commonly referred to as a recess. A recess introduces additional challenges, exciting sloshing modes that may cause large motions when oscillating over the shallow water zone of the recess. Figure 1.1 shows a moonpool with the recess configuration investigated in this thesis.

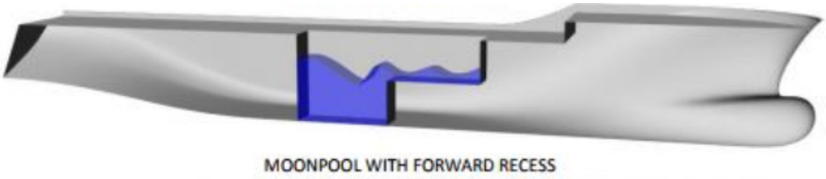

Figure 1.1: Moonpool with recess configuration investigated in this thesis (Törnblom and Hammargren, 2012)

The main motivation behind this master's thesis is the challenges faced in the industry, with regards to resonant fluid motions during moonpool operations. The natural periods of moonpool resonance are typically around 7-8s, which is likely to be excited in a sea state. The thesis will investigate resonant phenomena like piston mode and sloshing. Piston mode is vertical oscillations of the fluid inside the moonpool, while sloshing refers to oscillations back and forth like in a tank. An ill-designed moonpool may encounter violent resonant motions when these phenomena are excited, and this is a limiting factor for operational time for moonpool operations. With high rental rates for such specialized vessels, a bad moonpool design could prove very costly in the long run. The thought is that recess length, water depth in the shallow water working zone and heave amplitudes are important parameters, in order to understand the resonant motions. The tasks are tackled with experimental, numerical and analytical tools.

Figure 1.2 show a snapshot from a video where moonpool operations were not possible, due to violent moonpool flow in calm sea conditions.

Figure 1.2: Snapshots from video showing calm sea conditions, while moonpool operations were not possible due to resonant flow (Kristiansen et al., 2013)

1.1 Literature review

This section will present an overview of published research, that has contributed to the present knowledge on the physics of moonpools.

Aalbers (1984) suggested to treat the water column inside the moonpool as a mass-spring system, and showed that the equation of motion was very useful in order to understand the moonpool dynamics. This approach were later utilized by other authors, which will be presented in more detail in Section 2.1.1.

Molin (2001) utilized linearized potential theory, to present estimates of the natural modes of the free surface, and corresponding natural frequencies. The fluid domain is decomposed into two subdomains, the moonpool domain and the semi-infinite domain below the keel. Solutions are found for each subdomain by use of eigenfunction expansions. Molin (2001) carried out his procedure in both two and three dimensions, under the assumptions of an infinitely large barge with infinite water depth.

There has been some work presented related to motion minimization by careful design of the moonpool. With ricer fatigue problems encountered upon deep water oil production outside the coast of Brazil, Torres et al. (2004) studied the possibilities of reducing vertical motions by tuning some design parameters of the moonpool. They found that vertical motions of the floating unit could be reduced.

Experimental and linear theoretical results were compared by Faltinsen et al. (2007), with regards to different configurations of clean moonpool, that is a moonpool without any recess or other blockage. The experiments were carried out in a two-dimensional basin, with the hull made up by two rectangular boxes of equal length. The gap length between the boxes was changed between experiments, along with the draft. Through all tests the water depth was kept constant. The cases investigated are given in Table 1.1.

Cases	Gap length [m]	Box length [m]	Draft [m]	Depth [m]
1	0.18	0.36	0.18	1.03
2	0.18	0.36	0.27	1.03
3	0.36	0.36	0.18	1.03

Table 1.1: Moonpool configuration cases investigated by Faltinsen et al. (2007)

Faltinsen et al. (2007) showed that the piston mode resonance amplitudes strongly depend on the relationship between length of the hull boxes, and the length of the moonpool gap. Findings showed that case 1 and 2 produced relatively similar RAOs, with case 2 showing a small phase shift in resonance peak compared to theory. Faltinsen et al. (2007) concluded that the deviations between experiments and theory could be reduced by accounting for viscous damping. For case 3, the length of the moonpool gap is 0.36m, equal to the length of hull boxes. This configuration resulted in RAOs with resonance peaks from experiments closer to the linear results, and smaller than for case 1 and 2. Like in case 2, case 3 show a phase shift of resonance peak. The behaviour near resonance was such that Faltinsen et al. (2007) conclude that the differences could not be described solely on damping issues. Figure 1.3 shows the comparisons of case 1 and 3, with theoretical estimates.

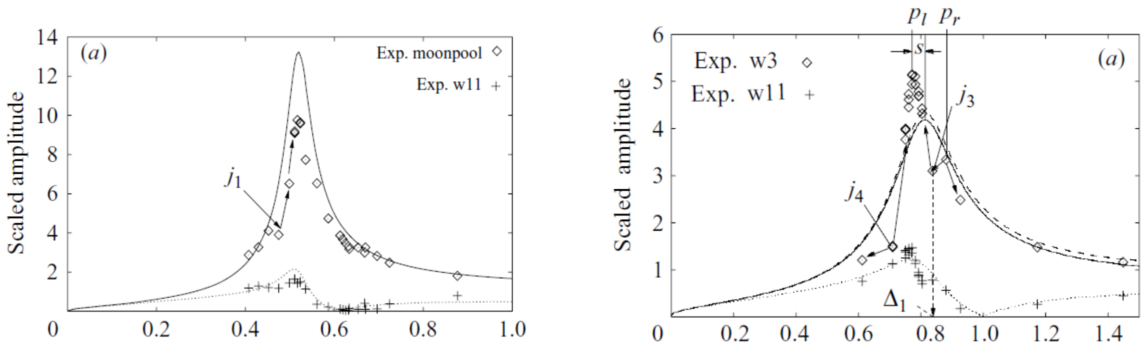

(a) Case 1 with reference to Table 1.1

(b) Case 3 with reference to Table 1.1

Figure 1.3: Comparison of wave elevation inside clean moonpool for ratio between box length and moonpool length = 0.5(a) and 1(b)

Lin et al. (2010) presented comparisons between potential theory, Navier-Stokes based Computational Fluid Dynamics(CFD) and experimental results. Their paper presents good agreements between experiments and CFD, while the potential theory greatly over predicts the motions. Their findings for the corresponding setup are presented in Figure 1.4. Lin et al. (2010) pointed out that despite failing to estimate the piston mode amplitude with sufficient accuracy, potential theory works well in finding the piston mode frequency.

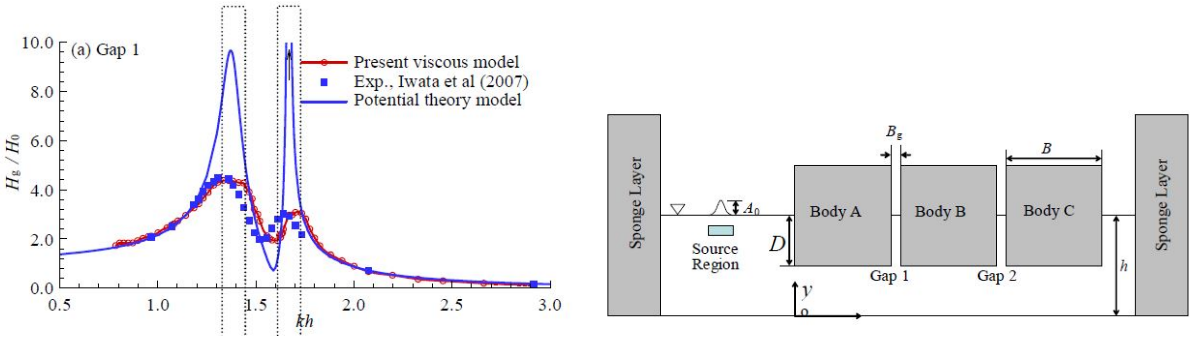

(a) Differences between potential theory, experiments and CFD

(b) Experimental setup

Figure 1.4: Findings by Lin et al. (2010) on differences of predicted wave heights for experiment, CFD and potential theory

Sauder et al. (2010) investigated the gap resonance problem between a moored LNG carrier and a bottom mounted offshore terminal, through CFD simulations. The CFD simulations were carried out using a Navier-Stokes solver in OpenFOAM, based on the Finite Volume Method(FVM). The results showed that convergence of the CFD simulations were difficult, and that the results by using a Boundary Element Method(BEM) combined with vortex tracking method were more precise. Also, the computational time was relatively high for the full CFD. However, the CFD simulations proved to be more robust. Sauder concluded that the CFD method provided results suitable for calibration of dissipation models in potential theory.

Despite the recent improvements in computational power, there are still limitations with regards to CFD calculations as an engineering tool. Kristiansen and Faltinsen (2011) presents a hybrid methodology that combines potential theory and Navier-Stokes in different subdomains. Where viscous features are prominent, Navier-Stokes equations are solved. The rest of the fluid domain is governed by potential theory. Kristiansen et al. (2013) presents a validation study of the method implemented in a code named Potential Viscous Code 3D(PVC3D), in the context of a clean moonpool. The paper points at equal computational time as pure potential flow simulations, while still capturing the flow separations in the Navier-Stokes domain. Kristiansen and Faltinsen (2011) presents results of piston mode amplitude for a 2D moonpool setup, while Kristiansen et al. (2013) presents results for the 3D case. The validations against both setups show equally good correspondence with experiments, with low computational requirements. In Figure 1.5 the principle of the hybrid method is visualized.

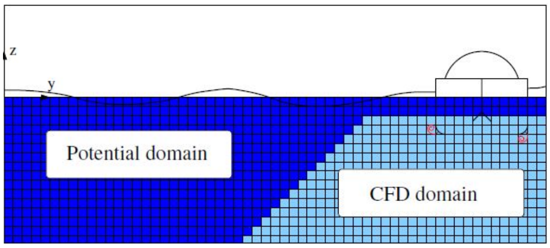

Figure 1.5: Illustration of domain in hybrid code PVC3D, using domain decomposition (Kristiansen et al., 2013)

Inspired by the hybrid method by Kristiansen and Faltinsen (2011), Fredriksen et al. (2012) proposed a hybrid numerical setup to investigate moonpool resonance at forwards speed. In order to capture the wave-current interaction, a perturbation method up to second order in surface elevation ζ, for the free surface condition around z = 0 was used. By doing this, they hoped to maintain the low computational time like the methodology by Kristiansen and Faltinsen (2011). Results showed that experiments and numerics correlated well, and that a slight decrease in piston mode amplitude was observed for increasing Froude numbers. With increasing forcing amplitudes larger differences between numerics and experiments were observed, as vorticity reached the intersection to the potential domain.

With regards to the case when a shallow water recess is present in the moonpool, some work has been done. While work has not yet been published on the application of PVC3D in the case of a recess inside the moonpool, some work that could represent similar features are done. Following studies on clean moonpools, some attention has been shown to the blockage effect caused by objects inside the moonpool. The recess could be seen upon as such an object, and Kristiansen et al. (2015) present comparisons between PVC3D, experiments and potential theory for the case of an object inside a moonpool, as shown in Figure 1.6. It is seen that PVC3D show good agreements with the experiments, especially compared with potential theory.

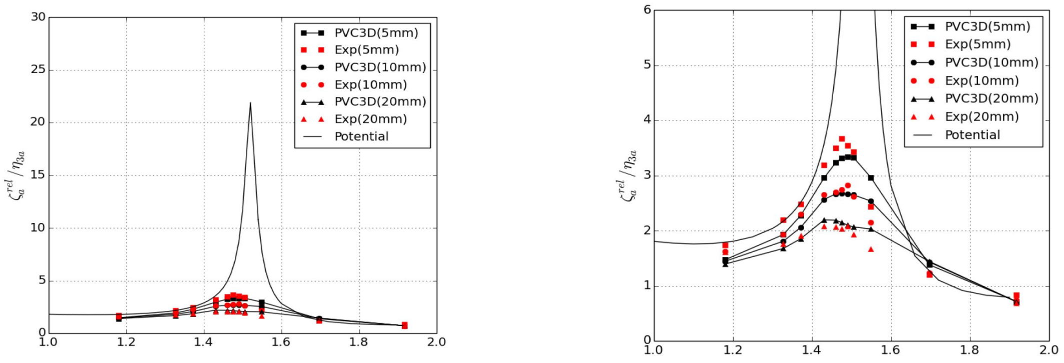

(a) RAO of moonpool with blockage

(b) Zoomed in on (a)

Figure 1.6: Comparison between potential theory, PVC3D and experiments for piston mode in moonpool with blockage object (Kristiansen et al., 2015)

Guo et al. (2016) presents results from numerical 3D potential theory simulations, validated by experimental results. Their work investigates the hydrodynamic effects of a moonpool with recess, on the six degree of freedom(DOF) RAOs of a Floating, Drilling, Production, Storage and Offloading(FDPSO) type of drilling ship. The paper also presents RAOs of the wave elevation inside the moonpool, at three different wave probes. The 3D model was moored by four above water lines and subjected to incident waves with various headings. Figure 1.7 present the RAO of wave elevation in the middle of the moonpool, consistent with Figure 1.7b.

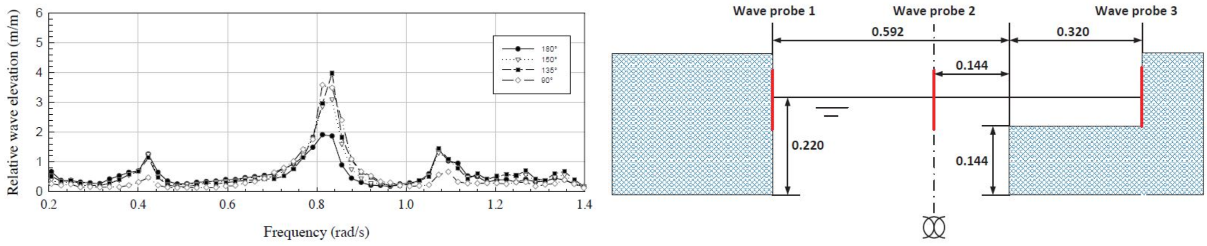

(a) RAO of wave elevation at center of moonpool with recess

(b) Cross section of moonpool with recess

Figure 1.7: RAO of wave elevation in moonpool with recess (Guo et al., 2016)

Molin (2017) used the methods presented in Molin (2001), and extended it to account for the case with a recess inside the moonpool. In this paper Molin (2017) present a simple formula, which prove to give a good approximation of the piston mode frequency, my taking the fluid inside the moonpool as a solid element. A particular finding by Molin is that the largest point of motion at piston mode, occurs by the moonpool wall above the recess.

1.2 Scope of work

Because of the challenges that is faced in the industry with regards to operational time inside moonpools, this master's thesis project will investigate the resonant motions in the shallow water zone above a recess. Important factors of the shallow water behaviour are believed to be recess length, heave amplitude and water depth in the shallow water zone. In order to contribute to the present knowledge on moonpool resonance behaviour, the main objectives of this master's thesis are summarized by the bullet points below

- Present a literature review highlighting studies and research that is relevant to this thesis
- Give an overview of important theory and utilize the strengths of potential theory to complement the experimental and numerical results. Special attention will be shown to domain decomposition and matched eigenfunction expansions.
- Conduct experiments to investigate the effect of recess length, draft and forcing amplitude, on resonance amplitudes and the linearity of the free surface inside the moonpool.

- Verify and compare experiments with numerical simulations, and examine the applicability of the hybrid code PVC3D in the shallow water zone.

1.3 Limitations

The scope of this master's thesis is limited to two-dimensional studies.

1.4 Structure of thesis

This section will briefly describe the structure of this thesis.

Chapter 1 provides the background of the thesis, with an outline of motivation. A literature review is presented, and the main objectives of the thesis are formulated.

In Chapter 2 an outline of important theory is presented, under the scope of this thesis with focus on the formulated objectives. Special attention is turned to potential theory, as it will be at the core of the thesis. The methods of matched eigenfunction expansions are described with domain decomposition. The method is applied to both three and six subdomains of the fluid domain in the case of a moonpool with recess.

Chapter 3 and Chapter 4 describes the numerical and experimental procedures respectively, and how these are structured and executed in order to obtain precise results.

In Chapter 5 the main results of this thesis are presented and discussed upon. Section 5.1 presents findings and discussions from experiments, while numerical results and discussions are presented in Section 5.2.

The thesis ends with conclusive remarks and suggestions of further work in Chapter 6.

Chapter 2

Theory

This chapter will present theory and governing equations that are of importance in the context of this thesis. The motivation for including the various topics, and how they relate to the scope will be briefly discussed first. As potential theory is widely applied both by matched eigenfunction expansions and in PVC3D, an outline of the governing equations are presented. Shortcomings of the theory will also be discussed, to understand possible deviations to experimental results. As PVC3D combine strengths from both potential theory and Navier-Stokes, a section on Navier-Stokes will be presented. With the presence of the recess, shallow water effects are investigated. Hence, some shallow water theory is described to discuss the applicability of this in the present case. In the literature review in Chapter 1 it was shown that some authors treated the moonpool flow as a mass-spring system. An outline of dynamic systems will be presented, both in terms of a general linear case and special non-linear cases.

2.1 Potential theory

In the following, an outline of potential theory will be presented. Governing equations and assumptions will be outlined, and strengths as well as limitations of the theory will be discussed. The chapter is mainly based on Faltinsen (1993). Figure 2.1 shows an overview of the control volume relevant for the scope of this thesis, in the frame of potential theory.

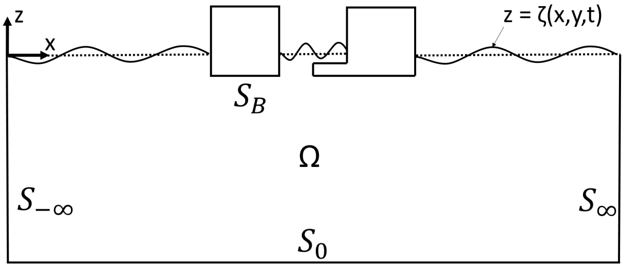

Figure 2.1: Fluid domain defined in the scope of potential theory. Ω defines the whole fluid domain, S_0 the domain bottom, S_B the model surface and $S_{-\infty}$ and S_∞ vertical boundaries of the domain.

The main assumptions within potential theory is ideal fluid. That is, the fluid is assumed to be inviscid, irrotational and incompressible. The first two assumptions obviously need to be treated carefully in typical marine technology applications, as the fluid is viscous and more or less rotational. As the flow is assumed irrotational, it is known from mathematics that the velocity vector can be expressed by a velocity potential, i.e. $\mathbf{V} = \nabla\phi$. The velocity potential ϕ is a scalar function, and this simplifies the proceeding calculations. Perturbation theory is utilized, and one expresses the total velocity potential as a power series of potentials, i.e. $\phi = \phi_1 + \phi_2 + ...$, with $\phi_1 = \mathcal{O}(\epsilon)$, $\phi_2 = \mathcal{O}(\epsilon^2)$ etc. The same procedure goes for the free surface elevation, ζ. Following the assumption that the flow is incompressible, the divergence of the velocity vector is zero, i.e. $\nabla \cdot \mathbf{V} = 0$. Inserting the irrotational expression, shows that the flow satisfies the Laplace equation in eq. 2.1 inside the fluid domain Ω.

$$\frac{\partial^2\phi}{\partial x^2} + \frac{\partial^2\phi}{\partial y^2} + \frac{\partial^2\phi}{\partial z^2} = 0 \quad \text{in}\,\Omega \tag{2.1}$$

To find a solution for the velocity potential in a fluid-body problem, one needs to make use of the right boundary conditions. In potential theory, these are the kinematic and dynamic boundary conditions. The kinematic boundary condition ensures impermeability at the body surface, and it implies that a particle on the free surface stays on the free surface. To express the kinematic boundary condition, the mathematical properties of the substantial derivative is utilized. This procedure is in detail outlined by Faltinsen (1993), and will thus not be repeated in the following. Following this procedure, the kinematic boundary condition in eq. 2.2 is found

$$\frac{\partial\zeta}{\partial t} + \frac{\partial\phi}{\partial x}\frac{\partial\zeta}{\partial x} + \frac{\partial\phi}{\partial y}\frac{\partial\zeta}{\partial y} - \frac{\partial\phi}{\partial z} = 0 \quad \text{on z} = \zeta\text{(x,y,t)} \tag{2.2}$$

The dynamic free surface condition implies that the pressure at the free surface is equal to the atmospheric pressure. If one choses the constant C in the Bernoulli equation to be $\frac{p_0}{\rho}$, one finds the following non-linear dynamic free-surface condition as eq. 2.3

$$g\zeta + \frac{\partial\phi}{\partial t} + \frac{1}{2}\left(\left(\frac{\partial\phi}{\partial x}\right)^2 + \left(\frac{\partial\phi}{\partial y}\right)^2 + \left(\frac{\partial\phi}{\partial z}\right)^2\right) = 0 \quad \text{on z} = \zeta\text{(x,y,t)} \tag{2.3}$$

Eq. 2.2 and 2.3 are the non-linear boundary conditions needed in order to solve fluid-body problems in potential theory. By linearizing the problem, it is possible to solve the problems despite not knowing where the free surface is beforehand. One can Taylor expand the free surface conditions from the free surface $z = \zeta(x, y, t)$ to the known mean free surface z = 0. In linear potential theory one keeps the terms in the velocity potential that is proportional to the wave amplitude, and neglects higher order terms. This is valid if the wave amplitude is small relative to the wave length and body dimensions. These simplifications yield the following linear expressions for the kinematic and dynamic boundary conditions, respectively in eq. 2.4 and 2.5.

$$\frac{\partial \zeta}{\partial t} = \frac{\partial \phi}{\partial z} \quad \text{on z=0} \tag{2.4}$$

$$g\zeta + \frac{\partial \phi}{\partial t} = 0 \quad \text{on z=0} \tag{2.5}$$

By combining eq. 2.4 and eq. 2.5, the combined free surface condition can be expressed as

$$\frac{\partial^2 \phi}{\partial t^2} + g\frac{\partial \phi}{\partial z} = 0 \quad \text{on z=0} \tag{2.6}$$

With the velocity potential oscillating harmonically in time with circular frequency ω, eq. 2.6 can be expressed as

$$-\omega^2 \phi + g\frac{\partial \phi}{\partial z} = 0 \quad \text{on z=0} \tag{2.7}$$

In addition to the free surface conditions, impermeability conditions can be established on the solid boundaries of the domain, as the body surface S_B and the bottom of the domain S_0

$$\frac{\partial \phi}{\partial n} = U \cdot n \quad \text{on } S_B \text{ and } S_0 \tag{2.8}$$

2.1.1 Initial analytical approaches

Prior to doing extensive numerical calculations or experiments, quick analytical estimates are useful. For instance, having an idea about what natural frequencies one should expect when planning experiments. This enables the researcher to execute the experiments around the relevant frequencies, which makes the experiments more compact. Below, two analytical approaches for calculating natural frequencies are presented. In general, the natural frequency of an undamped system is expressed as

$$\omega_n = \sqrt{\frac{k}{M+A}} \tag{2.9}$$

where k is stiffness, M is mass and A is added mass.

A good starting point for understanding the physics of the moonpool, is presented by Faltinsen (1993). The example is illustrated in Figure 2.2.

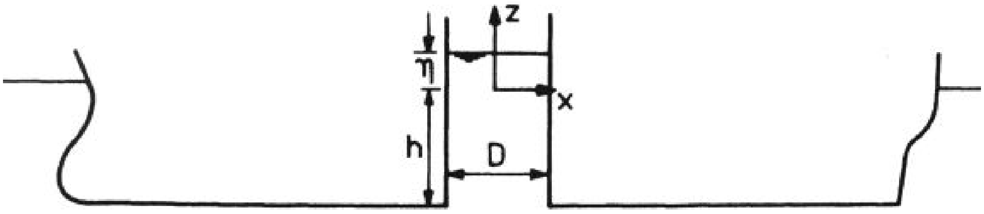

Figure 2.2: Moonpool and piston mode example (Faltinsen, 1993)

This example assumes that the water inside the moonpool can be approximated as a solid element, using linearized potential theory. The fluid acceleration is expressed through the fluid-momentum equation given by the Euler equation

$$\rho\frac{d^2\zeta}{dt^2} = -\frac{\partial p}{\partial z} - \rho g \tag{2.10}$$

which accordingly gives the fluid acceleration as

$$\frac{d^2\zeta}{dt^2} = -\frac{1}{\rho}\frac{\partial p}{\partial z} - g \tag{2.11}$$

Integrating eq. 2.11 from -h to ζ gives

$$\frac{d^2\zeta}{dt^2} + \frac{g}{h}\zeta = -\frac{1}{h}\frac{\partial\phi}{\partial t}\bigg|_{z=-h} \tag{2.12}$$

Writing the free surface elevation as $\zeta = \zeta_a \cos\omega t$ and inserting into eq. 2.12 yields a differential equation of ω. Then the homogeneous solution is expressed as

$$\frac{d^2\zeta}{dt^2} + \frac{g}{h}\zeta = 0 \rightarrow \left[-\omega_n^2 + \frac{g}{h}\right]\zeta = 0 \tag{2.13}$$

which gives the final expression for the natural frequency ω_n

$$\omega_n = \sqrt{\frac{g}{h}} \tag{2.14}$$

where h is the distance from the free surface to the bottom of the moonpool and g is acceleration of gravity. In this case h can be seen as a measure of the mass of the solid element, while g represents the system stiffness.

Another approach to find analytical expressions for the natural frequencies, is presented by Molin (2001). In addition to the piston mode, Molin presents solutions for higher order sloshing modes, along with corresponding mode shapes. Molin assumes infinite water depth and infinite length and beam of a barge, along with linearized potential theory. The solutions are derived by utilizing domain decomposition. Molin decompose the fluid domain into two parts, inside the moonpool and the semi infinite lower half-plane. The fluid domain is described by Figure 2.3.

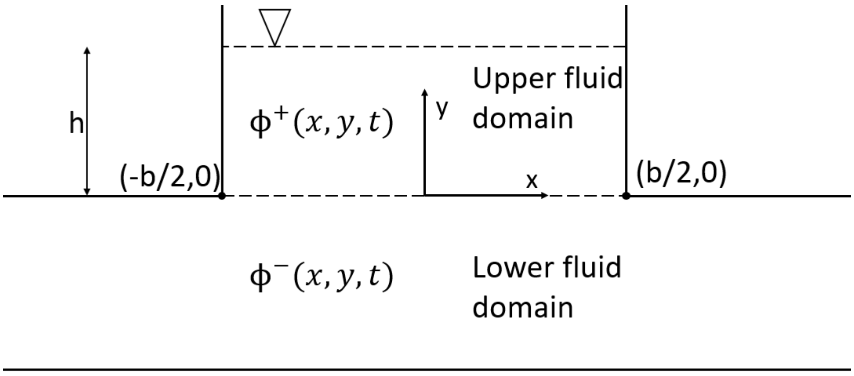

Figure 2.3: Definition of fluid domain in Molin (2001). Figure inspired by Reiersen (2016)

With $\phi_1^-(x,0,t)$ being the vertical velocity at the boundary between the two domains, the complex velocity potential in the lower domain is given as

$$f^-(z,t) = -\frac{1}{\pi}\int_{-b/2}^{b/2} \phi_y^-(\zeta,0,t)\ \ln\,(z-\zeta)d\zeta \tag{2.15}$$

where the coordinate system is based in the center of the moonpool base, b is the moonpool length in the x-direction and $z = x + iy$. With the assumption of infinite beam, eq. 2.15 produces a singular potential at infinity when there is a non-zero mass flux through the moonpool base. To model the fact that the water will flow around the keel and radiate waves at the free surface, Molin places two sinks at $x = \pm\lambda B/2$, where λ is somewhat larger than 1 and B is the beam of the barge. By introducing these sinks, the velocity potential in the the lowest domain can now be written as

$$f^-(z,t) = -\frac{1}{\pi}\int_{-b/2}^{b/2} \phi_y^-(\zeta,0,t)[\ln(z-\zeta) - \frac{1}{2}\ln(z-\lambda B/2) - \frac{1}{2}\ln(z+\lambda B/2)]d\zeta \tag{2.16}$$

By allowing an error $\mathcal{O}(b^2/(\lambda B)^2)$, the velocity potential on the intersection between the two domains is given by

$$\phi^-(x,0,t) = -\frac{1}{\pi}\int_{-b/2}^{b/2} \phi_y^-(\zeta,0,t)\ln\frac{|x-\zeta|}{\lambda B/2}d\zeta \tag{2.17}$$

As the matching procedure is that the velocity potential and their derivatives are equal on the intersections between the domains, eq. 2.17 is the lower boundary condition for $\phi^+(x,0,t)$. Solving the spectral problem, fulfilling the no-flow condition and the Laplace equation, gives an approximation for the piston mode frequency. The approximation assumes that the water inside the moonpool can be evaluated as a solid element

$$\omega_n = \sqrt{\frac{g}{h + (b/\pi)(\frac{3}{2} + \ln(\lambda B/2b))}} \tag{2.18}$$

By recalling the general expression for the undamped natural frequency in eq. 2.9 and comparing eq. 2.14 with eq. 2.18, it is seen that the term $(b/\pi)(\frac{3}{2} + \ln(\lambda B/2b))$ expresses the added mass in the formula by Molin.

2.1.2 Limitations of linear potential theory

While potential theory in many cases provides fast and precise results of loads, it is important to understand the limitations of the theory. In marine applications, the most obvious limitation is the assumption of inviscid fluid. Also, the assumption of irrotational flow is dubious, especially in the boundary layer. In relation to moonpool operations, viscous damping plays a significant role when calculating motions inside the moonpool as pointed out in the the literature review. Flow separation will occur both at bilge keels and at the entrance of the moonpool. This separation provides significant damping to both the body and the fluid motions.

As pointed out earlier in Section 2.1, the linear dynamic free surface condition in eq. 2.5 neglects the second order term in eq. 2.3. The implication of this simplification is visually described in Figure 2.4 by a tank exited at the first sloshing mode frequency by a piston. As seen in Figure 2.4, the difference between the linear and non-linear dynamic free surface conditions, is the quadratic term $\nabla\phi \cdot \nabla\phi$. If one take $\phi \sim \cos \omega t$, it is seen that $\nabla\phi \cdot \nabla\phi \sim \frac{1}{2}(1+\cos 2\omega t)$. This shows that the free surface in fact excites 2ω, which will not be accounted for by linear theory. This effect goes on and on, and higher order harmonics will be excited.

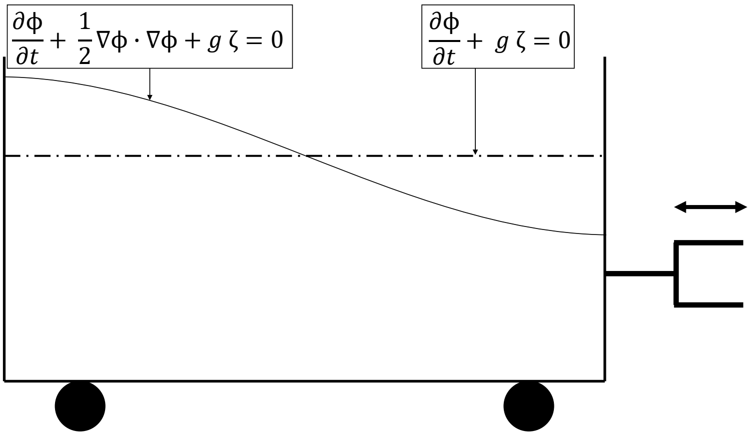

Figure 2.4: The dynamic free surface conditions in linear and non-linear potential theory

2.1.3 Practical implementation of potential theory

As discussed, potential theory comes with both pros and cons. For practical implementation of the theory, two different approaches will be presented in the following. In practical use, these methods are best suited for investigation of loads on large volume structures, where viscous load are less dominant.

Boundary element methods

BEM, or panel methods, are the most common way to implement potential theory (Faltinsen, 1993). The main idea with BEM is to distribute sinks and sources over the mean wetted surface of the body. To describe the procedure, a two-dimensional approach is used. The velocity potential at an arbitrary point P due to a source is given as

$$\phi = \frac{Q}{2\pi} \ln\, r \tag{2.19}$$

where Q is the strength of the source, and r is the radial distance from the point P. At the center of the source $r = 0$, there is obviously a singular point. In order to obtain finite potentials all across the fluid, use is made of a continuous representation of sources. By distributing sources over the body surface S, one can write

$$\phi(y,z) = \int_S q(s)\, \ln((y - \eta(s))^2 + (z - \zeta(s))^2)^{\frac{1}{2}} \tag{2.20}$$

where η and ζ are local coordinates on the body surface, s is an integration variable along the surface and (y,z) are coordinates in the fluid. In order to find the potential in eq. 2.20, reference are made to the thorough procedure outlined in chapter 4 of Faltinsen (1993).

Eigenfunction expansions

Depending on the geometry of the problem at hand, eigenfunction expansions can be utilized (Linton and McIver, 2001). That is, if one can express the velocity potentials as eigenfunction expansions through decomposition of the fluid domain. Generally, one will seek solutions of the Laplace equation on the form

$$\phi(x,y,z) = W(x,y)Z(z) \tag{2.21}$$

By substituting this into the Laplace equation, one gets

$$\frac{1}{W}\left(\frac{\partial^2 W}{\partial x^2} + \frac{\partial^2 W}{\partial y^2}\right) = -\frac{1}{Z}\frac{d^2 Z}{dz^2} = \alpha^2 \tag{2.22}$$

where α is the eigenvalue that is determined by the boundary conditions.

In a two-dimensional case, there will be no dependency of x in eq. 2.22. Then, a general solution will be

$$W(x,y) = X(x) = Ae^{-\alpha x} + Be^{\alpha x} \tag{2.23}$$

Lastly, by superimposing all possible modes, the velocity potential ϕ is obtained by an eigenfunction expansion

$$\phi(x,z) = \sum_{n=0}^{\infty} (A_n e^{-k_n x} + B_n e^{k_n x})\psi(z) \tag{2.24}$$

2.2 Matched eigenfunction expansions

In this section the usefulness of matched eigenfunction expansions are described. Findings by implementing the theory presented by Molin (2017) will be shown, in terms of estimates of the natural periods of piston mode and sloshing modes, for moonpool with recess configurations as in the experimental setup in Chapter 4. The theory is used to establish relevant and compact test matrices, and results are compared with experiments in Chapter 5. Also, an outline of how this is done for six subdomains will be presented. Dividing the fluid domain into six subdomains and by that accounting for the outer free surface, gives information like RAO, added mass, damping and amplitude of radiated waves. The background for matching eigenfunction expansions in six domains are provided through private communication with Professor Bernard Molin(2018)

2.2.1 Matching of eigenfunction expansions in three subdomains

This section presents findings from implementing the theory presented by Molin (2017). The fluid domain is decomposed into three subdomains, linear potential theory is utilized and the velocity potentials are written as eigenfunction expansions in each subdomain. The problem is illustrated in Figure 2.5.

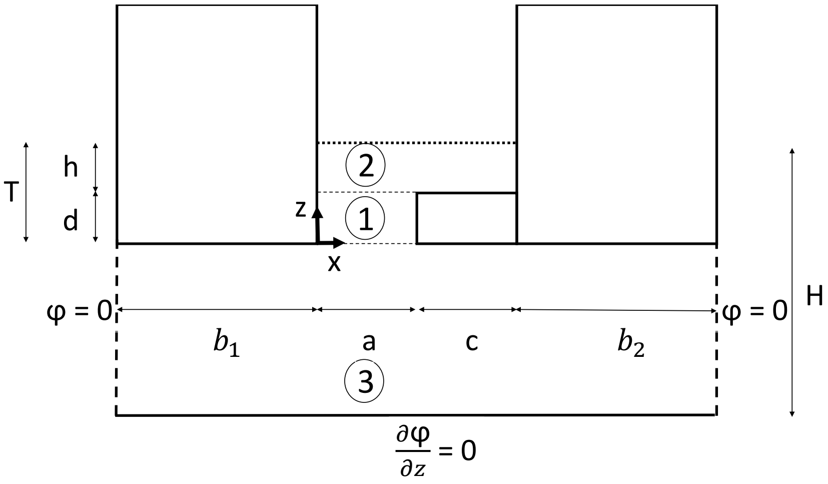

Figure 2.5: Fluid domain decomposed into three subdomains, where the velocity potentials are expressed by eigenfunction expansions in each subdomain

The potentials in subdomain 1 and 2 are written with inspiration from Molin (2017), subject to some adjustment to match the moonpool configuration investigated in this thesis. To account for the finite water depth in the basin, the potential in subdomain 3 is written as in Haiyang Huang (2018). The matching procedures are thoroughly described in Appendix A, and are similar to those described by an example for six subdomains in Section 2.2.2.

Domain 1 $(0 \le x \le a)$ $(0 \le z \le d)$

$$\phi_1(x,z) = A_0 + B_0\,\frac{z}{d} + \sum_{n=1}^{N_1}\Big(A_n \cosh\, k_n z + B_n \sinh\, k_n z\Big)\cos\, k_n x \tag{2.25}$$

$$k_n = \frac{n\pi}{a} \tag{2.26}$$

Domain 2 $(0 \le x \le a+c)$ $(d \le z \le d+h)$

$$\phi_2(x,z) = C_0 + D_0\,\frac{z-d}{h} + \sum_{n=1}^{N_2}\Big(C_n \cosh\, \lambda_n(z-d) + D_n \sinh\, \lambda_n(z-d)\Big)\cos\, \lambda_n x \tag{2.27}$$

$$\lambda_n = \frac{n\pi}{a+c} \tag{2.28}$$

Domain 3 $(-b_1 \le x \le a+c+b_2)$ $(-H+T \le z \le 0)$

$$\phi_3(x,z) = \sum_{n=1}^{N_3} E_n\,\frac{\cosh\, \mu_n(z+H-T)}{\cosh\, \mu_n(H-T)}\,\sin\, \mu_n(x+b_1) \tag{2.29}$$

$$\mu_n = \frac{n\pi}{b_1+a+b+b_2} \tag{2.30}$$

Figure 2.6 and 2.7 presents the natural periods for piston mode and the first sloshing mode, as a function of recess length and draft, respectively. For varying recess length a draft of 0.1m is presented. For varying draft, a recess length of 0.2m is shown. The expansions have been truncated to N_1, N_2 and $N_3 = 10$.

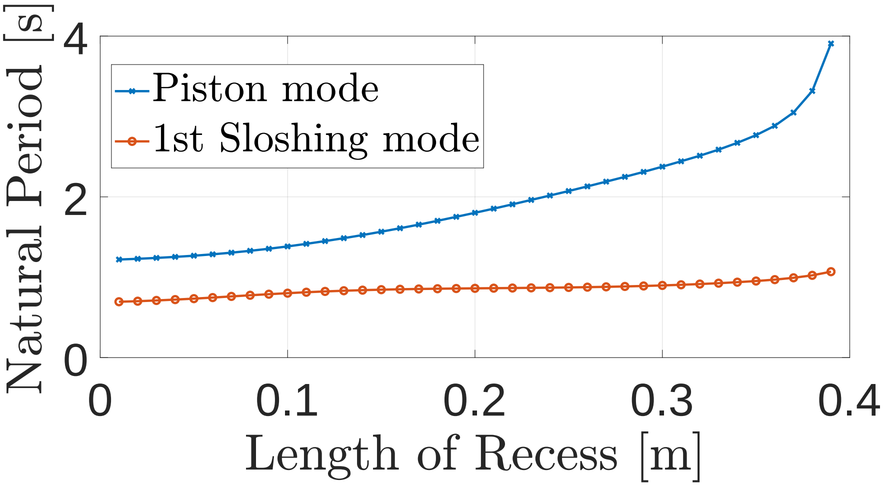

Figure 2.6: Natural periods of piston mode and first sloshing mode for varying recess lengths, with draft 0.1m

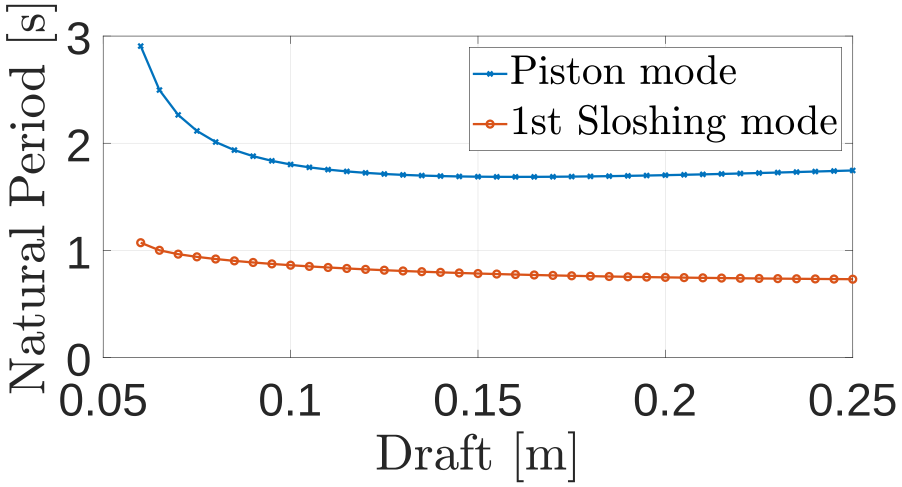

Figure 2.7: Natural periods of piston mode and first sloshing mode for varying drafts, with recess length 0.2m

Table 2.1 shows the natural periods for piston mode and the first three sloshing modes, for the drafts that experiments are presented for with recess length 0.2m. With the information obtained from the theory presented in Figure 2.6 and 2.7, it is possible to establish test matrices for each run.

Draft [m]	0.1	0.11	0.12	0.14	0.17
Piston [s]	1.8012	1.7534	1.7233	1.6933	1.6871
1st sloshing [s]	0.8616	0.8405	0.8228	0.7950	0.7665
2nd sloshing [s]	0.5499	0.5370	0.5283	0.5179	0.5108
3rd sloshing [s]	0.4313	0.4249	0.4207	0.4163	0.4140

Table 2.1: Natural periods for piston mode, and the three first sloshing modes, for various drafts with recess length 0.2m

2.2.2 Matching of eigenfunction expansions in six subdomains

This section will present how the methods of matched eigenfunction expansions can be applied for six subdomains. For a simpler general case, this method is described by Cointe and Geyer (1991), where they implement the method in relation to motions of a barge. Figure 2.8 shows how the domain decomposition of the fluid domain is structured. The time dependency is formulated as

$$\Phi(x,z,t) \;=\; \mathbb{R}\{\,\phi(x,y)\;e^{-i\omega t}\,\} \tag{2.31}$$

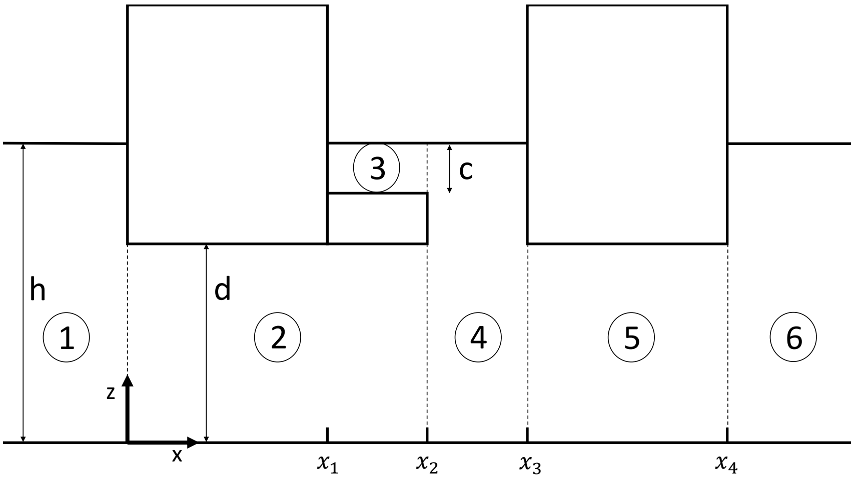

Figure 2.8: Main fluid domain decomposed into six subdomains

In the following, analytical expressions of the velocity potentials are expressed in each subdomain, by means of eigenfunction expansions. The velocity potentials satisfies the Laplace equation from eq. 2.1 in the fluid domain, and the linearized free surface condition from eq. 2.7. Also, the potentials obey no flow conditions $\frac{\partial\phi}{\partial z} = 1$ at horizontal parts of the model and $\frac{\partial\phi}{\partial x} = 0$ at vertical parts of the model. In domain 1 and 6, the potentials fulfills outgoing conditions by the exponential endings. At the bottom $\frac{\partial\phi}{\partial z} = 0$ is satisfied. k and μ are wave numbers for drafts of d and c respectively, and are established from the dispersion relations in eq. 2.33 and eq. 2.37. The following eigenfunction expansions are provided through private communication with Professor Bernard Molin.

Domain 1 $(-\infty \le x \le 0)$ $(0 \le z \le h)$

$$\phi_1\,(x,z) = A_0\,\frac{\cosh\,k_0 z}{\cosh\,k_0 h}\;e^{-ik_0 x} + \sum_{n=1}^{N_1} A_n\,\cos\,k_n z\;e^{k_n x} \tag{2.32}$$

$$\omega^2 \;=\; gk_0\,\tanh\,k_0 h \;=\; -gk_n\,\tan\,k_n h \tag{2.33}$$

Domain 2 $(0 \le x \le x_2)$ $(0 \le z \le d)$

$$\begin{aligned} \phi_2\,(x,z) = {} & \frac{z^2 - \left(x - \frac{x_2}{2}\right)^2}{2d} + B_0\frac{x}{x_2} + C_0\frac{x - x_2}{x_2} \\ & + \sum_{n=1}^{N_2} \cos\,\lambda_n z\left[B_n\frac{\sinh\,\lambda_n x}{\sinh\,\lambda_n x_2} + C_n\frac{\sinh\,\lambda_n(x-x_2)}{\sinh\,\lambda_n x_2}\right] \end{aligned} \tag{2.34}$$

$$\lambda_n = \frac{n\pi}{d} \tag{2.35}$$

Domain 3 $(x_1 \le x \le x_2)$ $(h - c \le z \le h)$

$$\begin{aligned} \phi_3\,(x,z) = {} & z + \frac{g}{\omega^2} - h + D_0\frac{\cosh\,\mu_0(z-h+c)}{\cosh\,\mu_0 c}\cos\,\mu_0(x - x_1) \\ & + \sum_{n=1}^{N_3} D_n\,\cos\,\mu_n(z-h+c)\,\frac{\cosh\,\mu_n(x-x_1)}{\cosh\,\mu_n(x_2-x_1)} \end{aligned} \tag{2.36}$$

$$\omega^2 = g\mu_0\,\tanh\,\mu_0 c = -g\mu_n\,\tan\,\mu_n c \tag{2.37}$$

Domain 4 $(x_2 \le x \le x_3)$ $(0 \le z \le h)$

$$\begin{aligned} \phi_4\,(x,z) = {} & \frac{\cosh\,k_0 z}{\cosh\,k_0 h}\left[E_0\,\cos\,k_0(x-x_2) + F_0\,\cos\,k_0(x-x_3)\right] \\ & + \sum_{n=1}^{N_4} \cos\,k_n z\left[E_n\frac{\cosh\,k_n(x-x_2)}{\cosh\,k_n(x_3-x_2)} + F_n\frac{\cosh\,k_n(x-x_3)}{\cosh\,k_n(x_3-x_2)}\right] \end{aligned} \tag{2.38}$$

Domain 5 $(x_3 \le x \le x_4)$ $(0 \le z \le d)$

$$\begin{aligned} \phi_5\,(x,z) = {} & \frac{z^2 - \left(x - \frac{x_3+x_4}{2}\right)^2}{2d} + G_0\frac{x-x_3}{x_4-x_3} + H_0\frac{x - x_4}{x_4 - x_3} \\ & + \sum_{n=1}^{N_5} \cos\,\lambda_n z\left[G_n\frac{\sinh\,\lambda_n(x - x_3)}{\sinh\,\lambda_n(x_4 - x_3)} + H_n\frac{\sinh\,\lambda_n(x-x_4)}{\sinh\,\lambda_n(x_4 - x_3)}\right] \end{aligned} \tag{2.39}$$

Domain 6 $(x_4 \le x \le \infty)$ $(0 \le z \le h)$

$$\phi_6\,(x,z) = I_0\,\frac{\cosh\,k_0 z}{\cosh\,k_0 h}\,e^{ik_0(x-x_4)} + \sum_{n=1}^{N_6} I_n\,\cos\,k_n z\,e^{-k_n(x-x_4)} \tag{2.40}$$

Matching procedure of potentials and derivatives

To find solutions for the velocity potentials, one has to find values for the unknown vectors $A = (A_0, A_1, ...A_{N1})$, $B = (B_0, B_1, ...B_{N2})$, ... , $I = (I_0, I_1, ...I_{N6})$. This is done by matching the velocity potentials and their derivatives at their vertical intersections. By carrying out the matching procedures at all vertical intersections, the following set of equations are obtained

$$A = R_2 + M_2\Big[D_2 B + D_3 C\Big] \tag{2.41}$$

$$B = R_4 + M_5 E + M_6 F \tag{2.42}$$

$$C = R_1 + M_1 A \tag{2.43}$$

$$D = R_3 + M_3 E + M_4 F \tag{2.44}$$

$$E = R_7 + M_{12} G + M13H \tag{2.45}$$

$$F = R_5 + M_7 B + M_8 C + M_9 D \tag{2.46}$$

$$G = R_8 + M_{14} I \tag{2.47}$$

$$H = R_6 + M_{10} E + M11F \tag{2.48}$$

$$I = R_9 + M_{15}\Big[D_4 G + D_5 H\Big] \tag{2.49}$$

The vectors are complex quantities, such that $A = A_r + iA_i$. A, D and I can be eliminated by inserting them into the equations for C, F and G respectively. The unknown vectors can be collapsed into a vector that can be found by solving the linear equation system, Ax=b.

$$A = \begin{bmatrix} -M_1 M_2 D2 & (Id - M_1 M_2 D3) & 0 & 0 & 0 & 0 \\ Id & 0 & -M_5 & -M_6 & 0 & 0 \\ -M_7 & -M_8 & -M_9 M_3 & (Id - M_9 M_4) & 0 & 0 \\ 0 & 0 & -M_{10} & -M_{11} & 0 & Id \\ 0 & 0 & Id & 0 & -M_{12} & -M_{13} \\ 0 & 0 & 0 & 0 & (Id - M_{14} M_{15} D_4) & -M_{14} M_{15} D_5 \end{bmatrix}$$

$$x = \begin{bmatrix} B_r + iB_i \\ C_r + iC_i \\ E_r + iE_i \\ F_r + iF_i \\ G_r + iG_i \\ H_r + iH_i \end{bmatrix}$$

$$B = \begin{bmatrix} R_1 + M_1 R_2 \\ R_4 \\ R_5 + M_9 R_3 \\ R_6 \\ R_7 \\ R_8 + M_{14} R_9 \end{bmatrix}$$

where Id in the A-matrix are identity matrices. The procedure of matching the potentials and their derivatives, will be exemplified by matching ϕ_5 and ϕ_6, and ϕ_{5x} and ϕ_{6x}, in x = x_4.

Example of matching of potentials

For x = x_4, it tells from eq. 2.39 and eq. 2.40 that

$$\phi_5\,(x_4,z) = \frac{z^2}{2d} - \frac{x_4^2 - 2x_4x_3 + x_3^2}{8d} + G_0 + \sum_{n=1}^{N_5} G_n \cos\lambda_n z \tag{2.50}$$

$$\phi_6\,(x_4,z) = I_0\,\frac{\cosh k_0 z}{\cosh k_0 h} + \sum_{n=1}^{N_6} I_n \cos k_n z \tag{2.51}$$

By setting $\phi_5(x_4,z) = \phi_6(x_4,z)$, the following equation is obtained

$$G_0 + \sum_{n=1}^{N_5} G_n \cos\lambda_n z = -\frac{z^2}{2d} + \frac{x_4^2 - 2x_4x_3 + x_3^2}{8d} + I_0\,\frac{\cosh k_0 z}{\cosh k_0 h} + \sum_{n=1}^{N_6} I_n \cos k_n z \tag{2.52}$$

To find expressions of G_0 and G_m, the properties of trigonometric and hyperbolic functions are utilized. In x = x_4, the following properties are used

$$\int_0^d \cos\lambda_n z\,dz = 0 \tag{2.53}$$

$$\int_0^d \cos\lambda_n z\,\cos\lambda_m z\,dz = 0 \quad \text{for n} \neq \text{m} \tag{2.54}$$

Thus, by integrating each side of eq. 2.52 from 0 to d, the following expression is found for G_0

$$G_0 d = -\frac{d^2}{6} + \frac{x_4^2 - 2x_4x_3 + x_3^2}{8} + I_0\frac{\sinh k_0 d}{k_0 \cosh k_0 h} + \frac{\sin k_n d}{k_n} \tag{2.55}$$

Then, the property of eq. 2.54 is utilized, by multiplying each side of eq. 2.52 with cos $\lambda_m z$ and integrating from 0 to d. The following expression for G_m is established

$$\begin{aligned} G_m \int_0^d \cos^2\lambda_m z\,dz &= -\int_0^d \frac{z^2}{2d}\cos\lambda_m z\,dz \\ + \frac{I_0}{\cosh k_0 h}\int_0^d \cosh k_0 z\,\cos\lambda_m z\,dz &+ \sum_{n=1}^{N_6} I_n \int_0^d \cos k_n z\,\cos\lambda_m z\,dz \end{aligned} \tag{2.56}$$

Eq. 2.55 and eq. 2.56 can be collected as

$$G = R_8 + M_{14}\,I \tag{2.57}$$

where G = $(G_0, G_1, ..., G_{N5})$ is a $(N_5 + 1, 1)$ column vector, R_8 is a $(N_5 + 1, 1)$ column vector, M_{14} is a full $(N5 + 1, N6 + 1)$ matrix and I = $(I_0, I_1, ..., I_{N6})$ is a $(N_6 + 1, 1)$ column vector.

Example of matching of derivatives

By taking the x-derivatives of eq. 2.39 and eq. 2.40 in x = x_4, one finds

$$\phi_{5x}\,(x_4,z) = \frac{x_3-x_4}{2d} + \frac{G_0+H_0}{x_4-x_3} + \sum_{n=1}^{N_5} \lambda_n \cos \lambda_n z \left[G_n \coth \lambda_n\,(x_4-x_3) + \frac{H_n}{\sinh \lambda_n(x_4-x_3)} \right] \tag{2.58}$$

$$\phi_{6x}\,(x_4,z) = ik_0 I_0 \frac{\cosh k_0 z}{\cosh k_0 h} - \sum_{n=1}^{N_6} k_n I_n \cos k_n z \tag{2.59}$$

In x = x_4, the following relationship hold between ϕ_{5x} and ϕ_{6x}

$$\phi_{6x}(x_4,z) = \begin{cases} = \ \ \phi_{5x}(x_4,z) \quad 0 \le \mathrm{z} \le \mathrm{d} \\ = \ \ 0 \quad \mathrm{d} \le \mathrm{z} \le \mathrm{h} \end{cases} \tag{2.60}$$

Now one can make use of the following property

$$\int_0^h \cos k_n z \cosh k_0 z \, dz = 0 \tag{2.61}$$

Multiplying both sides of eq. 2.60 by $\cosh k_0 z$ and integrating over the respective domains of validity as

$$\int_0^h \phi_{6x} \cosh k_0 z\, dz = \int_0^d \phi_{5x} \cosh k_0 z\, dz \tag{2.62}$$

yields the following expression

$$\begin{aligned} \frac{ik_0 I_0}{\cosh k_0 h} \int_0^h \cosh^2 k_0 z\, dz \ &= \ \frac{x_3-x_4}{2d}\,\frac{\sinh k_0 d}{k_0} + \frac{G_0+H_0}{X_4-X_3}\,\frac{\sinh k_0 d}{k_0} \\ + \sum_{n=1}^{N_5} \lambda_n \bigg[G_n \coth \lambda_n\,(x_4-x_3) \ &+ \ \frac{H_n}{\sinh \lambda_n(x_4-x_3)} \bigg] \int_0^d \cosh k_0 z \cos \lambda_n z\, dz \end{aligned} \tag{2.63}$$

Then, multiplying both sides of eq. 2.60 by $\cos k_m z$ and integrate over the respective domains of validity as

$$\int_0^h \phi_{6x} \cos k_m z\, dz = \int_0^d \phi_{5x} \cos k_m z\, dz \tag{2.64}$$

gives the final expression for I_m

$$\begin{aligned} -k_m I_m \int_0^h \cos^2 k_m z\, dz &= \frac{x_3-x_4}{2d}\,\frac{sin\; k_m d}{k_m} + \frac{G_0+H_0}{x_4-x_3}\,\frac{sink_m d}{k_m} \\ &+ \sum_{n=1}^{N_5} \lambda_n \left[G_n \coth \lambda_n\,(x_4-x_3) \ + \ \frac{H_n}{sinh\, \lambda_n\,(x_4-x_3)} \right] \end{aligned} \tag{2.65}$$

Eq. 2.63 and eq. 2.65 can be represented by the following expression

$$I = R_9 + M_{15}\Big[D_4 G + D_5 H\Big] \tag{2.66}$$

where R_9 is a $(N_6+1,1)$ column vector, M_{15} is a full $(N6+1, N5+1)$ matrix and H = $(H_0, H_1, ..., H_{N5})$ is a $(N_5+1,1)$ column vector and D_4 and D_5 are (N5+1,N5+1) diagonal matrices.

When matching at all intersections are done, it is important to verify that the potentials and their derivatives in fact match at their vertical boundaries. The velocity potentials should match perfectly with coinciding curves, while the derivatives will be somewhat oscillatory because of the Gibbs effect at the square corners. When series of trigonometric functions are used to describe a function that has a jump discontinuity, an overshoot occurs at the discontinuity (Zhu et al., 2011). This is seen in the matchings in Appendix B, at the sharp corners of the model. Figure 2.9 shows a preliminary RAO at position x = $\frac{1}{2}(x_1 + x_2)$, with h = 1m, d = 0.9m and c = 0.05m in accordance with Figure 2.8, with recess length of 0.2m. The problem has been solved with truncation orders of N1 = N4 = N6 = 15, N2=N5=13 and N3 = 10. The wave amplitude ζ_a is obtained as

$$i\,\omega\,\zeta_a\,e^{i\omega t} = \frac{\partial\phi}{\partial z}\,e^{i\omega t} \tag{2.67}$$

The dashed lines in Figure 2.9 shows how the estimated natural periods from Section 2.2.1 compare with the six domain findings.

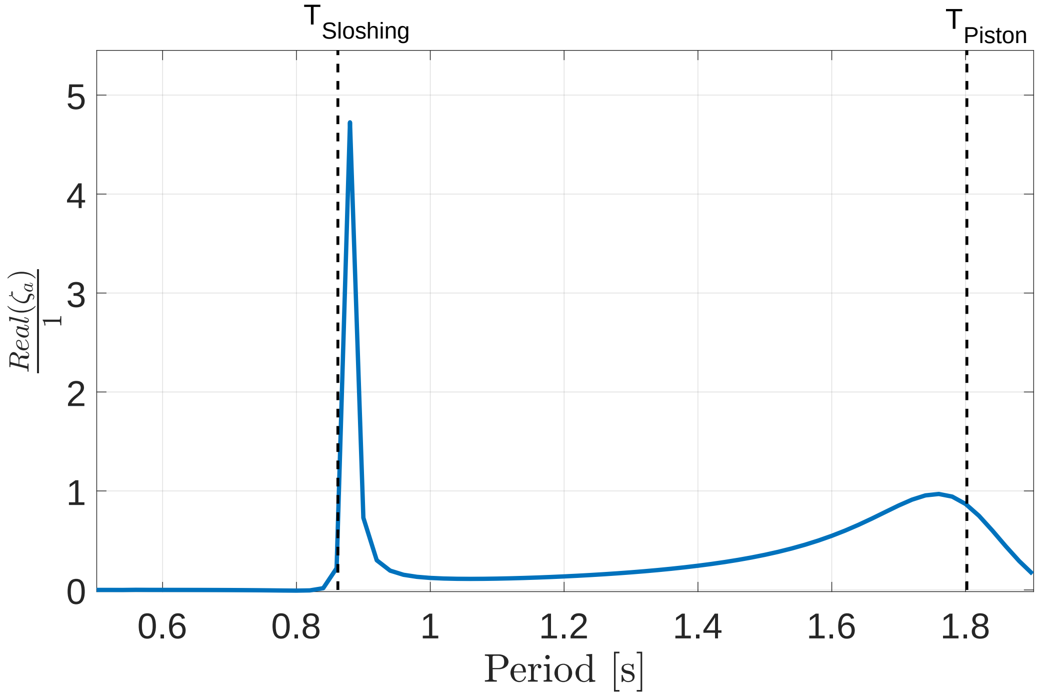

Figure 2.9: RAO by domain decomposition and matched eigenfunction expansions for velocity potential, with d=0.9m, c=0.05m, h=1m and recess length of 0.2m. The RAO is measured in x=$\frac{x_2+x_1}{2}$, in accordance with Figure 2.8

2.3 Navier-Stokes equation for incompressible, isothermal flow

In Section 2.1 potential theory was outlined. In that case, the main assumptions are that the fluid is incompressible, irrotational and inviscid. However, these assumptions are only applicable in certain situations. Another approach is to assume that the fluid is incompressible. In most cases this assumption holds for water, except in cases where acoustics matter. In marine technology applications this is typically related to slamming, at the bow of a ship or during lowering of e.g suction anchors (Faltinsen, 1993). Newtonian fluids are fluids where the shear stress is linearly proportional to the shear strain rate (Çengel, 2010). When assuming compressible fluid Cengel present a thorough derivation of the Navier-Stokes equation for incompressible, isothermal flow. Constant viscosity follows from the assumption of isothermal flow. The assumptions of incompressible flow simplifies the viscous stress tensor of Cauchy's equation. The derivation yields the governing equations in Cartesian coordinates where eq. 2.68 is the continuity equation for an incompressible fluid and eq. 2.69 is the x-component of the Navier-Stokes equations.

$$\frac{\partial u}{\partial x}+\frac{\partial v}{\partial y}+\frac{\partial w}{\partial z}=0 \tag{2.68}$$

$$\rho\left(\frac{\partial u}{\partial t}+u\frac{\partial u}{\partial x}+v\frac{\partial u}{\partial y}+w\frac{\partial u}{\partial z}\right)=-\frac{\partial P}{\partial x}+\rho g_x+\mu\left(\frac{\partial^2 u}{\partial x^2}+\frac{\partial^2 u}{\partial y^2}+\frac{\partial^2 u}{\partial z^2}\right) \tag{2.69}$$

where u,v and w are components of the velocity vector, ρ is density, P is pressure and μ is the dynamic viscosity.

2.4 Shallow water behaviour and limits

This section will look at two different parameters used in order to describe shallow water behaviour. The presented theory will be used in order to understand the behaviour in the shallow water zone above the recess inside a moonpool. In Section 5.1 further discussions will be presented, with regards to experimental results.

2.4.1 Draft to length ratio of planar tank

It is shown that in a confined tank, the sloshing phenomena at resonance condition is dependent on water depth. From Faltinsen and Timokha (2009), Figure 2.10 shows sloshing for shallow(a), intermediate(b), critical(c) and finite(d) water depths.

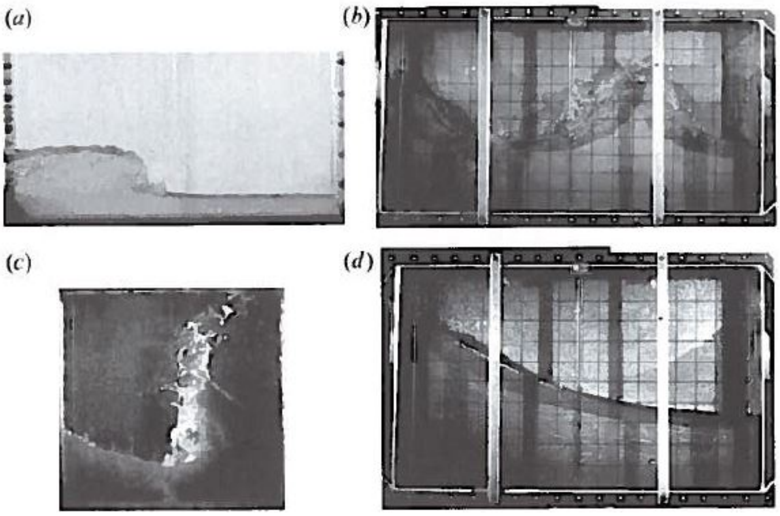

Figure 2.10: Sloshing phenomena at different water depths. a) Shallow water depth, b) Intermediate water depth, c) Critical water depth and d) Finite water depth (Faltinsen and Timokha, 2009)

The different scenarios presented in Figure 2.10 may be characterized by a depth-to-breadth ratio. It is also seen that this ratio is especially important when it comes to describing non-linearities. For a rectangular planer tank, Faltinsen and Timokha (2009) gives the exact analytical solution for the natural frequencies σ_i of sloshing modes i

$$\sigma_i = \sqrt{g\frac{\pi i}{l}\tanh\left(\frac{\pi i}{l}h\right)} \tag{2.70}$$

where l is tank length and h is water depth.

In relation to the four water depths in Figure 2.10 and eq. 2.70, it is possible to define limits for the different depths. As $\tanh\left(\frac{\pi i}{l}h\right)$ behave differently for different ratios h/l, Faltinsen and Timokha (2009) defines the limits in Table 2.2

Water depth	Limit
Shallow water	h/l $\lesssim$ 0.05 - 0.1
Intermediate water	0.05-0.1 $\lesssim$ h/l $\lesssim$ 0.2-0.25
Finite water	0.2-0.25 $\lesssim$ h/l $\lesssim$ 1, that is at least the lowest natural frequency σ_1 is dependent on h/l
Deep water	h/l is large → tanh(πh/l) ≈ 1

Table 2.2: Limits of water depth in a confined rectangular tank, based in h/l ratios

In the shallow water range it is seen that higher order sloshing modes σ_i becomes multiples of the lowest natural frequency σ_1, as in eq. 2.71

$$\sigma_i = n\sigma_1 \tag{2.71}$$

The consequence of eq. 2.71 is that fluid oscillations at several higher harmonic frequencies are excited when the forcing frequency is equal to the lowest natural frequency, σ_1. That means that in the shallow water region as defined above, one need a larger set of modes to describe the shallow water sloshing at resonance, $\sigma = \sigma_1$ (Faltinsen and Timokha, 2009).

The phenomenon described with higher modes excited non-linearly by the lowest natural mode, is called secondary resonance. Expanding from the equation for the natural frequency of each mode in eq. 2.70, the following general expression for when secondary resonance of the nth mode will occur for a planar rectangular tank is given

$$\frac{\sigma_1}{\sigma} \approx i_n = \frac{n\,T_n}{T_1} = \sqrt{\frac{n\,\tanh(\pi h(l))}{\tanh(n\pi h/l)}} \tag{2.72}$$

2.4.2 Ursell parameter

In 1847 Sir George Stokes discussed the importance of the parameter $\frac{A\lambda^2}{h^3}$ as a measure of the applicability of his second order wave theory. Following the work by Stokes, Fritz Ursell showed that the parameter was an useful measure between three different long wave theories (Svendsen, 2006). The parameter proposed by Stokes, included characteristic scale values, λ and A. The so called Ursell parameter is commonly adjusted for practical applicability. Wave amplitude is replaced by wave height H, and the horizontal scale λ is often replaced by wave length L.

$$\frac{A\,\lambda^2}{h^3} \sim U = \frac{H\,L^2}{h^3} \tag{2.73}$$

By utilizing the properties of the Ursell number, the following can be said of the shallow water waves

$$U = \begin{cases} \ll & \mathcal{O}(1) \quad \text{linear shallow water waves} \\ = & \mathcal{O}(1) \quad \text{cnoidal and solitary waves} \\ \gg & \mathcal{O}(1) \quad \text{non-linear shallow water waves} \end{cases} \tag{2.74}$$

In Section 5.1.4 a discussion is presented on the applicability of this parameter as a measure of the linearity of the free surface inside a moonpool with recess.

2.5 Dynamic systems

As pointed out earlier, seeing the moonpool fluid flow as a dynamic system is an useful approach. Hence, the theory of dynamic systems will be presented in the following. First the theory of linear dynamic systems will be presented, before an outlines of the so called duffing oscillator and Faraday waves will be given.

2.5.1 Linear dynamic system

To model physical oscillation phenomena, a linear relation between excitation and response is a common assumption. With constant coefficients m, c and k, the general one DOF linear equation of motion for a damped system becomes

$$m\ddot{x} + c\dot{x} + kx = F_0\, cos\, \omega t \tag{2.75}$$

where m is mass, c is damping, k is stiffness and F_0 is the excitation amplitude. $\ddot{x}, \dot{x}$ and x is acceleration, velocity and displacements respectively. Such system is commonly described as in Figure 2.11

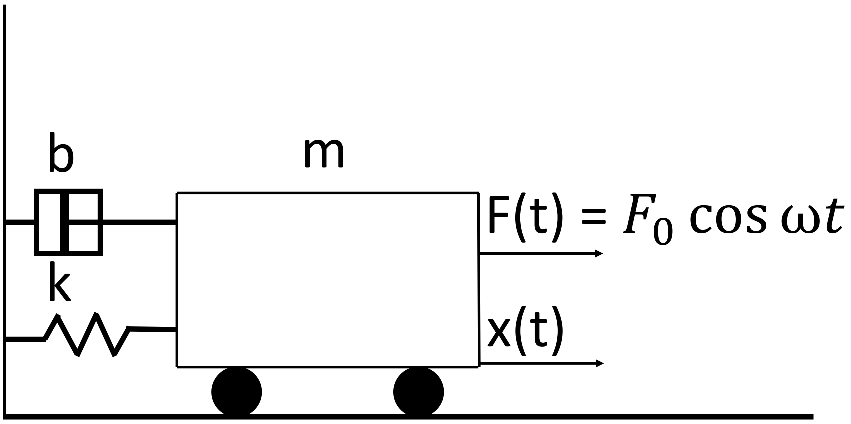

Figure 2.11: Forced damped dynamic system

Since the linear dynamic system serves as basics for the coming topics, a more thorough outline of how to obtain the Dynamic Load Factor(DLF) is given in Appendix C. The DLF is defined as

$$DLF = \left|\frac{u_{max}}{u_{st}}\right| = \frac{1}{\left[\left(1-\beta^2\right)\left(2\xi\beta\right)^2\right]^{\frac{1}{2}}} \tag{2.76}$$

where ξ is the damping ratio and β is frequency ratio.

Figure 2.12 shows the DLF for the linear dynamic damped system, exposed of external loading as a function of the frequency ratio

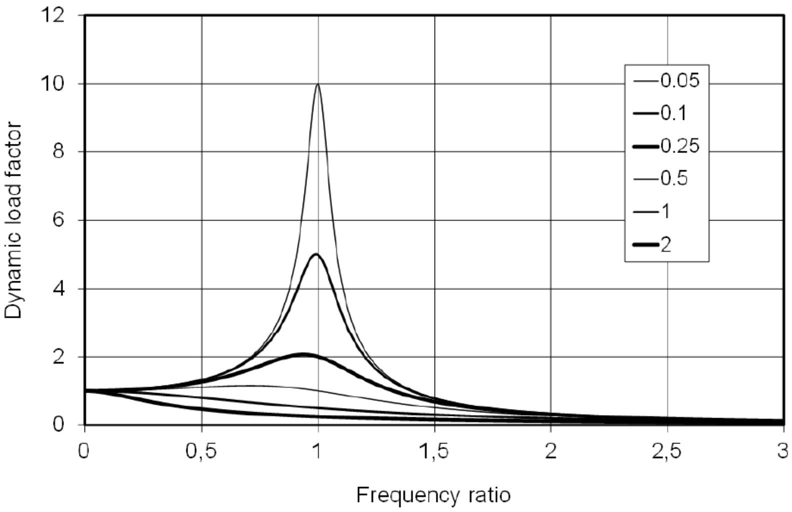

Figure 2.12: DLF of linear dynamic system, with damping and external excitation, for various damping ratios (Kovacic and Brennan, 2011)

2.5.2 Duffing oscillator

Despite the usefulness of describing a dynamic system by the differential equation in eq. 2.75, it has shortcomings in certain scenarios. In some situations, the stiffness of the system is dependent on displacement. This is in particular when excitation amplitudes is large. Hence, the excitation and displacement are no longer linearly dependent. In these situations, the dynamic behaviour of the system is described by different forms fo the so called duffing equation. If the stiffness of the system is equal in both tension and compression, the restoring force can be expressed through series expansions (Kovacic and Brennan, 2011). If the series are truncated after two terms, the restoring force can be written

$$F_{restoring} = k_1 y \pm k_3 y^3 \tag{2.77}$$

If the last term is positive the spring is hardening, while negative implies a softening spring. Figure 2.13 shows the relationship between displacement and restoring, when this relationship is both linear and non-linear. For the softening and harding cases, the cubic stiffness parameter $\gamma = 0.3$.

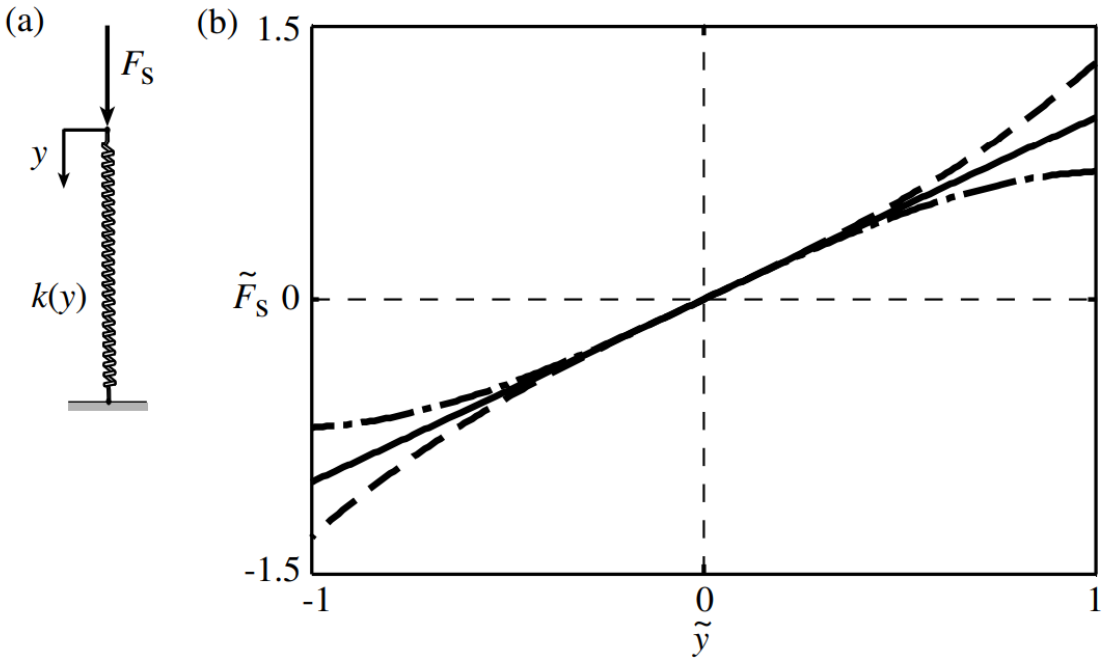

Figure 2.13: a) Spring b) Comparison between a hardening(dashed), a softening(dashed-dotted) and a linear(solid) spring. (Kovacic and Brennan, 2011)

To understand the applicability of the duffing oscillator in relation to moonpool dynamics, Kovacic and Brennan (2011) gives an outline of the equation with forced oscillations and damping. Eq. 2.78 is the non-dimensional duffing equation

$$\ddot{y} + 2\zeta\,\dot{y} + y + \gamma\,y^3 = F_0 \cos \omega t \tag{2.78}$$

where γ is the cubic stiffness parameter. The inclusion of the cubic stiffness, introduce some important changes compared to the linear systems described by eq. 2.75. First of all, the superposition principle is no longer applicable for establishing the response. Also, the steady state response now depends on the initial conditions, whereas the linear dynamic system is independent of the initial conditions.

Analogue to the procedure presented for the linear system in Section 2.5.1, the amplitude response is obtained by plotting the DLF against frequency ratio. Figure 2.14 shows the effect of the cubic stiffness parameter, compared to Figure 2.12 and the linear system. By investigating the duffing oscillator, it is seen that the maximum response does not occur exactly at the natural frequency, as it does in a linear system.

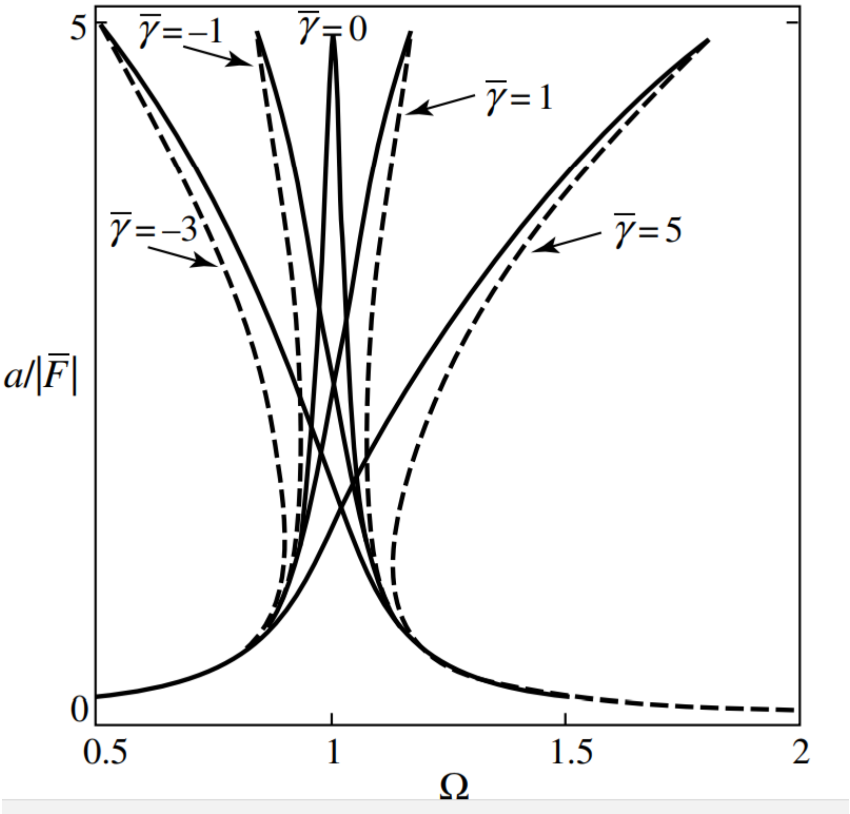

Figure 2.14: DLF for forced duffing oscillator plotted against frequency ratio Ω, with damping and different cubic resorting parameters γ. (Kovacic and Brennan, 2011)

2.5.3 Faraday waves

Another feature that could be interesting with regards to moonpool with a shallow water zone, is the so called Faraday effect. Faraday (1831) was the first to observe the effect, and the phenomena has been further investigated by many researchers. In linear theory, sloshing can not be excited in an enclosed tank linearly by vertical excitations. In reality, nonlinearities can cause dynamic instabilities that may result in large resonant sloshing behaviour (Faltinsen and Timokha, 2009). This serves as one of several plausible reasons for deviations between linear estimates and experiments. With regards to forcing period, the most dangerous instabilities for a planar tank occurs at T = $\frac{1}{2}T_m$, where T is forcing period and T_m is the natural period of the mth mode. These periods are referred to as parametric resonance, and is different to what is commonly called resonance in a mass-spring system, which is forcing period equal to the natural period. Bredmose et al. (2003) conducted vertical forcing experiments of a rectangular tank, at T = 0.4s. He excited the third natural mode, that is T = 0.4s ≈ $\frac{1}{2}T_3$. Figure 2.15 shows snapshots from his experiments

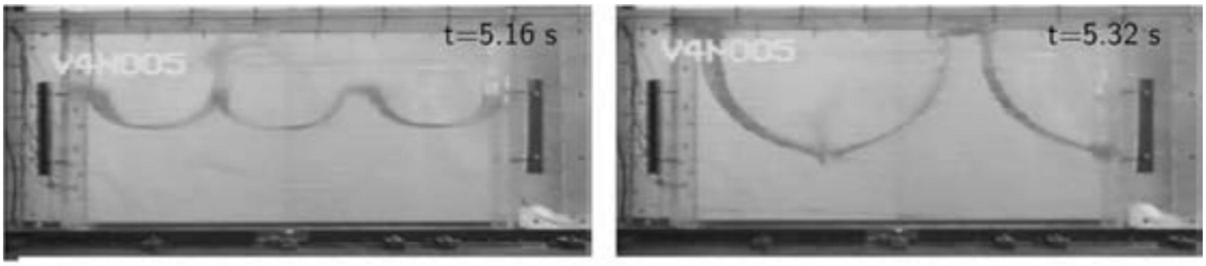

Figure 2.15: Faraday waves excited by vertical shaking of rectangular tank, with forcing period T = 0.4s $\approx \frac{1}{2}T_3$. Snapshots taken with sampling ratio 25 frames per second (Bredmose et al., 2003)

Chapter 3

Numerical Simulations

With the increase of available computational power, CFD has in recent years established itself as a strong tool in marine technology. Describing flow phenomena in marine applications can be done by partial differential equations such as Navier-Stokes equations. Solving these equations are not possible analytically, except in special cases under specific simplifications such as simple pipeline calculations. In CFD, the equations are solved numerically. This chapter will describe pitfalls and possibilities of CFD, and how the numerical method should be structured to obtain good approximate results. The theory in this chapter is mainly based on the theory presented by Faltinsen (1993) and Ferziger (2002). At the end of the chapter, an outline of the numerical grid generation process of the PVC3D simulations will be presented.

3.1 Sources of error between reality and numerical results

As mentioned, the numerical methods provide approximations of the reality. The deviations between computed results and reality arise from simplifications and approximations in the numerical method. Ferziger (2002) presents three bullet points to summarize these:

- Approximations or idealizations in the differential equations.
- Approximations in the discretization process.
- Iterative methods are used in solving the differential equations. Unless the iterations are run for a very long time, the exact solutions are not produced.

While the exact solution can be obtained in principle when the governing equations are exact, some physical phenomena requires some sort of modelling to express. An example of this is modelling of turbulent flow. This could be done by introducing a Raynolds-Averaged Navier-Stokes(RANS) model, where the mean and fluctuating part of the velocity and pressure are averaged. To solve for the turbulent flow, the Raynolds stress must be modeled as a function of the mean flow.

3.1.1 Validation and verification of numerical results

In the world of CFD validation and verification are terms that are frequently mentioned and emphasized. Roache (1997) defines the two terms in a neat way

- Verification - "solving the equations right"
- Validation - "solving the right equations"

Due to approximations and idealizations presented in Section 3.1, the importance of validation of the numerical results can not be emphasized enough Ferziger (2002). One important tool to investigate numerical solutions is visualization. In OpenFOAM, the main post-processing tool is the open source visualization application ParaView (OpenFOAM, 2018). ParaView enables the user to interpret large amount of data, through plots and videos of the flow. In the interface, the user can investigate various parameters, in order to analyze the results. However, one should not interpret the result as correct without thorough investigation. The visualization tool presents nice colorful plots and videos that might look correct at first sight, without critical examination.

3.2 Structure of a numerical method

In the following an outline of how a numerical solution method can be structured will be presented. The section is mainly based on the structure and theory presented by Ferziger (2002)

Mathematical model

The first step of a numerical solution method, is to choose an applicable set of governing partial differential equations and boundary conditions. Subject to the properties of the real flow, simplifications such as compressible, inviscid or two-dimensional flow, can be imposed to reduce the computational requirements. Each solution method is typically designed for certain equations. Hence, trying to make a general solution method for different sets of equations is often unrealistic.

Discretization model

When a mathematical model is selected, one has to decide upon a suitable method of discretization. That is, how to approximate the differential equations by algebraic equations, for variables at discrete locations in space and time. Several discretization methods exists, and the most important ones are finite difference, finite volume and finite element methods. When working in cases applicable for potential flow, boundary element methods are most commonly utilized.

Numerical grid

To make a discrete representation of the fluid domain, a numerical grid is developed. The numerical grid describes discrete locations where variables are calculated in the domain. To divide the domain into a finite number of subdomains, different grid options exists. Examples of these are structured grids, block-structured grids and unstructured grids. Examples of each type of grids are shown in Figure 3.1.

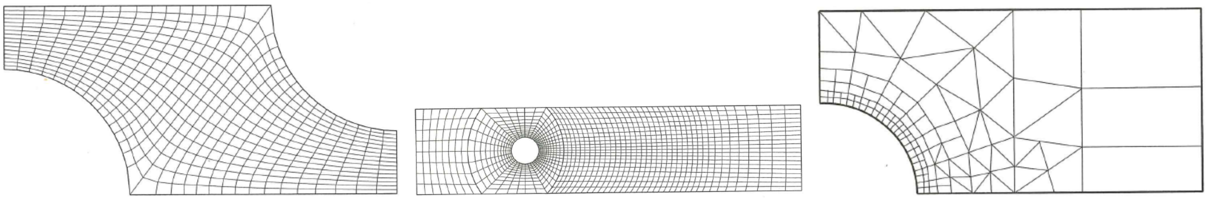

(a) Structured grid (b) Block-structured grid (c) Unstructured grid

Figure 3.1: Numerical grid types (Ferziger, 2002)

Finite approximations

When it comes to selecting appropriate approximations for the discretization, there exist several different approaches. These approximations are dependent on the chosen discretization method. In finite difference methods, one has to make approximations for the derivatives. In finite volume methods, approximations must be made regarding surface and volume integrals. Lastly, in finite element methods, choices must be made for shape and weighting functions. As stated, other methods also exists. Different methods have different requirements when is comes to coding, debugging and solving time. Large time requirements might come at the cost of refinement of grid. Thus, a compromise is needed in most cases.

Solutions method

Following the discretization process, one has a large system of non-linear equations to solve. In unsteady flow situations, solutions methods are based on those used in initial value problems. At each time step an elliptic problem has to be solved. Steady flow are solved by pseudo-time stepping or an equivalent iteration scheme. There are several options available when it comes to selecting a solution method, and the different methods depend on grid type and number of nodes.

Convergence criteria

As the solution methods in numerical methods use iterations, a convergence criteria must be set. The convergence criteria sets the limit for when to stop the inner and the outer iterations. The inner iterations consists of the linear equations, while the outer iterations deals with non-linearity. Both accuracy and efficiency are important when setting the convergence criteria.

3.3 Important properties of solution methods

In order to analyze the solution method, one typically analyses the different components of the solution. The different components are meant to have different properties. If a component does not posses the certain property, neither will the complete solution method. Some important properties of the solution method is presented in the following, based on Ferziger (2002)

Consistency

For a numerical solution method to be consistent, the discretization has to be exact when grid spacing goes towards zero. The truncation order error must approach zero, when the mesh spacing goes to zero. The truncation error is the difference between the discretized equation and the exact one. It is found by doing a Taylor expansion about a single point. The Taylor expansion produces the original equation, with the added truncation error.

Stability

If errors that occur during the solution process is not magnified, the numerical solution method is said to be stable. This implies that for an iterative process, the solution does not diverge. A common way to address the stability is through the Von Neumann's method. In some complicated cases, one often has to rely on experience and intuition.

Convergence

Convergence is said to be preserved if the exact solution is obtained as the grid spacing tends to zero. For linear problems, convergence is typically difficult to verify. In such cases convergence is addressed through repeated simulations with increasingly refined grids. At one point, the solution is found to converge and be independent of grid refinement. Convergence is dependent on consistency and stability.

Conservation

As the governing equations are conservation laws, the numerical scheme should also obey these laws. That is, the amount of quantity leaving a closed volume should equal the amount entering the volume. In the case when sources and sinks are present in the control volume, care should be taken such that conservation is obtained with the net flux through the boundaries. With an conservative solution, errors can only be distributed over the domain.

Non-conservative solutions can impose artificial sinks and sources both locally and globally. The error imposed by non-conservatism is dependent on the refinement of the grid, and the problem is largest for coarse grids. However, it is difficult to know what this refinement limit is, and conservatism is therefore preferred.

3.4 Numerical simulations in OpenFOAM with PVC3D

Numerical simulations of fluid flow inside the moonpool, when modeling both air and water by Volume of Fluid(VOF) methods or similar, are computational expensive. Thus, tools with less computational requirements are useful, especially for engineering purposes. The hybrid code PVC3D presented in Chapter 1, combines potential theory with Navier-Stokes. Since Kristiansen and Faltinsen (2011) presented the methodology, some slight modifications have been made. Because difficulties were encountered on the intersections between the potential and the viscous domains, the whole fluid domain is now governed by Navier-Stokes while the free surface still is captured by linear potential theory. As the simulations are run for single faced flow, probes are placed in similar locations as in experiments logging the dynamic pressure from the p_gh field.

3.4.1 Pre-processing of numerical simulations

In this section the process of generating an appropriate numerical mesh for carrying out PVC3D simulations in OpenFOAM will be presented.

In order to generate the mesh to run the CFD simulations, the documentation on the outline of the *snappyHexMesh* utility in OpenFOAM is used (OpenFOAM, 2018). With the *snappyHexMesh* utility, a 3D mesh is generated automatically of hexahedra and split-hexahedra. A hexahedra is any polyhedron with six faces, such as a cube. The hexahedra are generated from a surface geometry in STL-format. The STL file contains information about the solid geometry in ASCII format, by means of coordinates defining triangles across the geometry surface. The structure of the ASCII files are shown in Figure 3.2a and the model is visualized in Figure 3.2b where the triangles are visible.

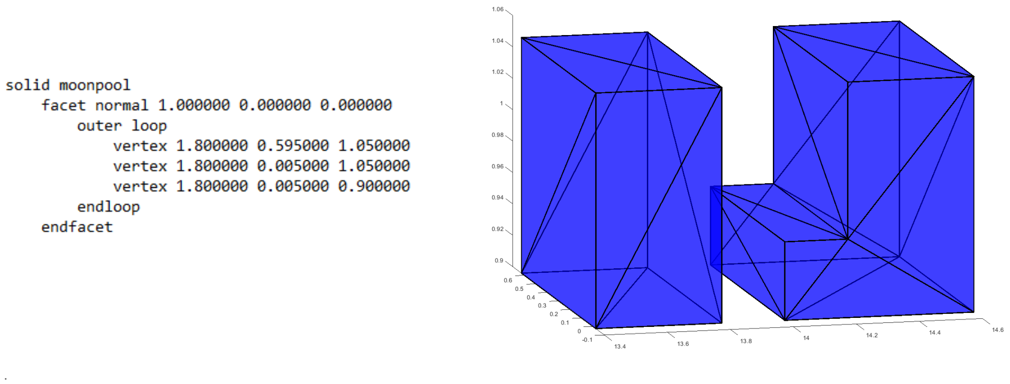

```
solid moonpool
    facet normal 1.000000 0.000000 0.000000
        outer loop
            vertex 1.800000 0.595000 1.050000
            vertex 1.800000 0.005000 1.050000
            vertex 1.800000 0.005000 0.900000
        endloop
    endfacet
```

(a) One triangle defined in ASCII format

(b) ASCII format visualized in Matlab

Figure 3.2: Geometry generated with STL file, in ASCII format

Prior to executing the *snappyHexMesh* utility, a background mesh has to be developed. This is done by use of the *blockMesh* utility, described in OpenFOAM (2018). The entire fluid domain is constructed by two boxes, each with length 14m, height 1m and width 0.6m, to in a best possible way model the model test facilities that will be described in Chapter 4. The boxes are placed side by side, to give a total domain length of 28m. Since no wave absorbers are modelled, the domain need to be long enough to avoid reflecting waves interfering with the model. The group velocity C_g is defined as

$$C_g = 0.5\,\frac{g}{\omega} \tag{3.1}$$

From previous simulations runtime of approximately 20 periods have proven necessary in order to obtain steady state at resonance. With an upper limit of forcing periods of 1s at the first sloshing mode resonance, the group velocity $C_g \approx 0.78\frac{m}{s}$. In order to extract oscillation amplitudes after steady state is obtained, the domain is chosen to be 28m long in total. For $C_g \approx 0.78\frac{m}{s}$, reflecting waves will interfere after approximately 35s.

For each box, the *simpleGrading* entry is utilized, to introduce a refinement from the end of each box towards the centre of the domain. The definition of the ratio is the length of the first cell to the length of the end cell, and the ratio is set to 0.2. The background mesh is shown in Figure 3.3

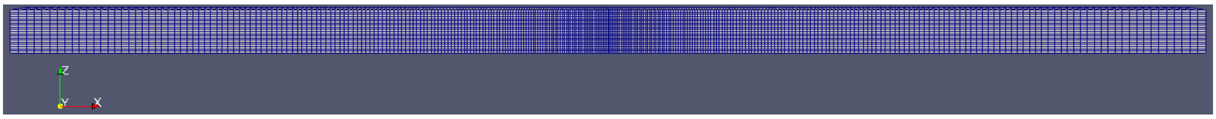

Figure 3.3: 28m long background mesh generated with the *blockMesh* utility. *simpleGrading* used to refine background mesh towards center of domain, with ratio between end cells and center cells 0.2

When the background mesh is generated, the *surfaceFeatureExtract* and *snappyHexMesh* utilities are utilized to generate a 3D mesh. In the *snappyHexMesh* dictionary, two specific entries are specified to generate the mesh. *castellatedMesh* does the refinement by splitting cells and *snap* adapts the castellated mesh to conform the geometry (OpenFOAM, 2018). This process is illustrated in Figure 3.4. On top of the background mesh, a refinement box around the model geometry is used. Each level of refinement splits each cell of the three-dimensional mesh in eight. In the present study refinement boxes of level three is used.

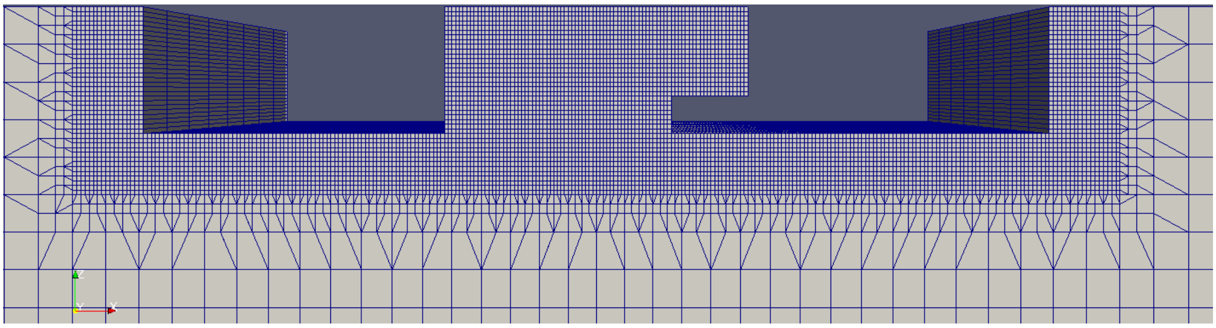

(a) *castellatedMesh* utility refining mesh by splitting cells

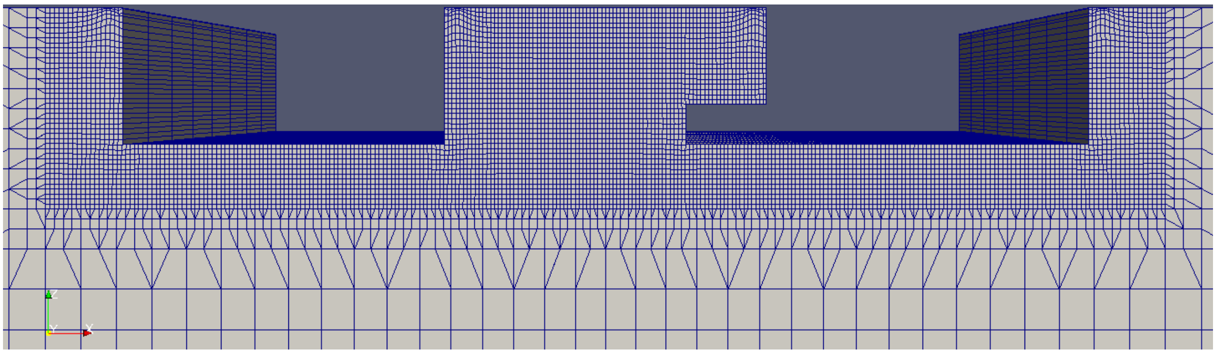

(b) *snap* utility comforming castellated mesh to geometry

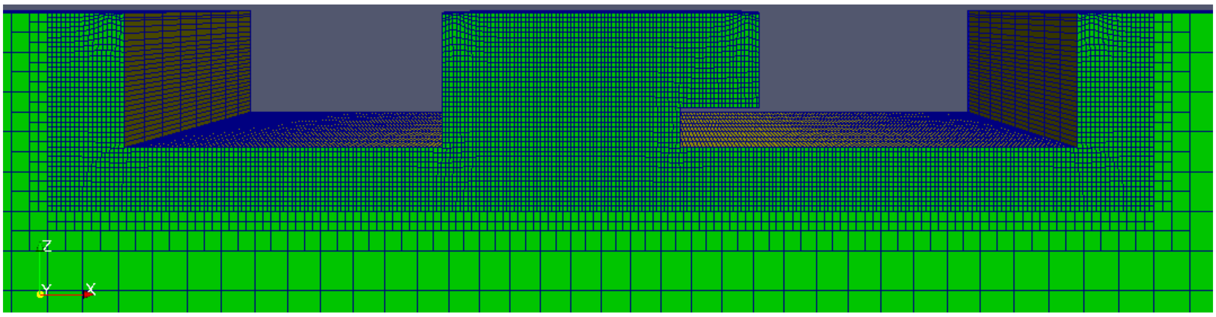

(c) Final 3D mesh

Figure 3.4: 3D mesh generated by utilizing the utility *snappyHexMesh*, with entries *castellatedMesh* and *snap*.

To generate a mesh that is two dimensional, *extrudeMesh* is utilized. This utility enables the user to select a patch, and extrude it in a given direction with a specified cell thickness. For the present simulations this thickness is set to 0.05m. This is shown in Figure 3.5, where it is visible that the cells in the y-direction generated by the refinement box around the model, is removed.

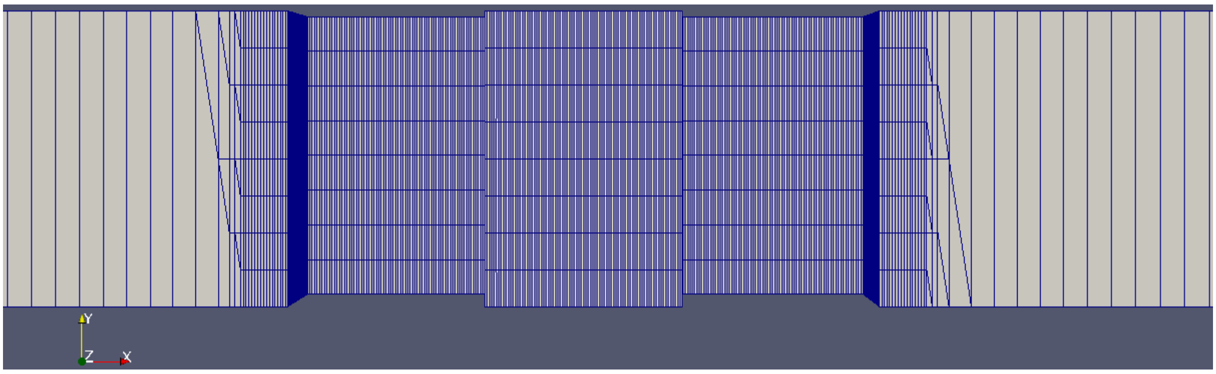

(a) Top view of mesh after using *snappyHexMesh* utility

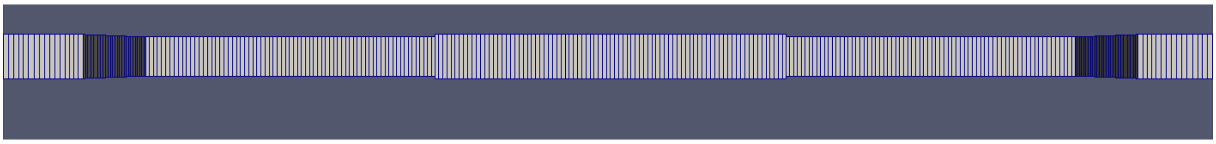

(b) Top view of mesh after using *extrudeMesh* utility

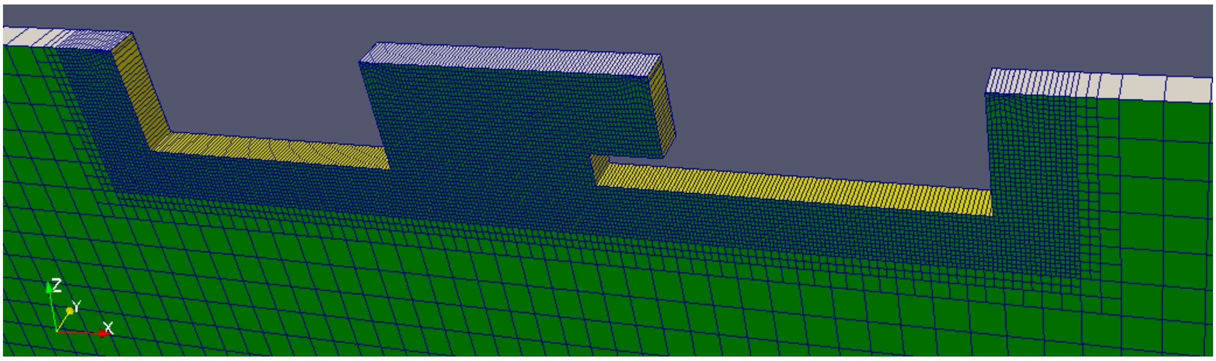

(c) Final 2D mesh

Figure 3.5: *extrudeMesh* utility is used to generate a 2D mesh from initial 3D mesh, by extruding the front patch a specified cell thickness 0.05m in the y-direction. a) shows how cell splitting generates cells in the y-direction, and b) shows how this is dealt with by *extrudeMesh*. c) shows the final 2D mesh

In Figure 3.6 the patches defining the boundaries are presented. The patches of the boundaries in the xz-plane of the fluid domain are accordingly denoted front and back. These boundaries are assigned with boundary conditions as presented in Table 3.1 , for both the mesh and the field files U, p_gh and p in the time folders.

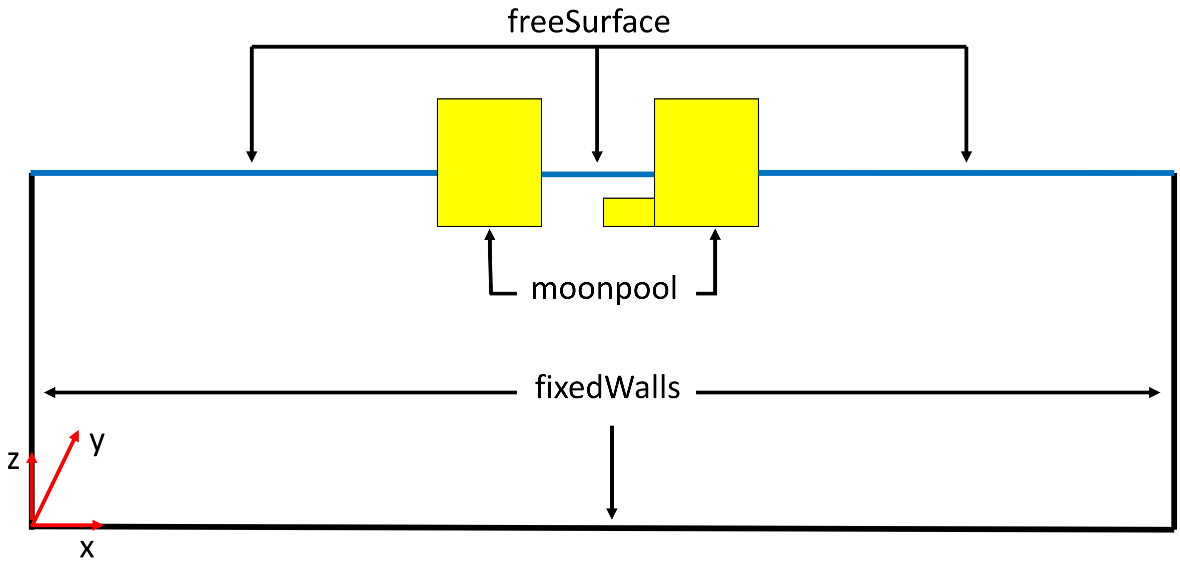

Figure 3.6: Patch names of numerical domain, for defining boundary conditions. The walls in the xz plane are named front and back.

	freeSurface	fixedWalls	moonpool	front	back
Mesh	patch	wall	movingWall	empty	empty
0/ U	pressureInletOutletParSlipVelocity	fixedValue	codedFixedValue	empty	empty
0/ p_gh	waveSurfacePressure	zeroGradient	zeroGradient	empty	empty
0/ p	calculated	calculated	calculated	empty	empty

Table 3.1: Boundary conditions of numerical simulations. Boundary conditions in Mesh is defined through the meshing procedure described above. In field files U, p_gh and p time directories defines the boundary conditions for how these parameters are solved.

Chapter 4

Experiments

This chapter will present the procedures in planning, executing and post-processing of two-dimensional forced heave model experiments. All model configurations were tested at drafts T of 0.1m, 0.11m, 0.12m, 0.14m and 0.17m with forcing amplitudes η_{osc} of 1mm, 2mm, 3mm, 4mm and 5mm. The experiments were carried out in the laboratory Ladertanken at NTNU. Ladertanken has a length L_T of 13m, width W_T of 0.6m and water depth h of 1m. Forced heave motion was applied by an oscillator rigged above the basin. The experiments presented were carried out over two lab periods, with piston mode experiments in March 2018 and sloshing experiments in April 2018. Thus, all setup procedures were carried out twice. An outline of how measurement systems were calibrated is given in Appendix D.

4.1 Model

Figure 4.1 illustrates the model that was used throughout all experiments. Recess lengths L_R of 0.2m, 0.15m and 0.1m were tested.

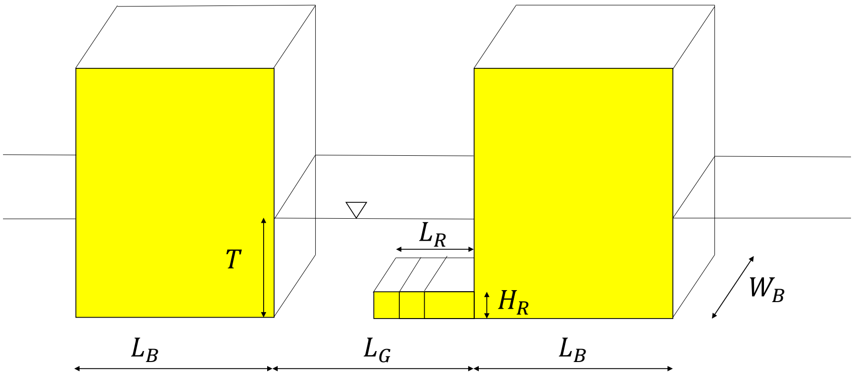

Figure 4.1: Model dimensions, with recess lengths L_R of 0.2m, 0.15m and 0.1m

All parameters in Table 4.1 were kept constant through all experiments

Constant	Value [m]
Box length, L_B	0.4
Gap length, L_G	0.4
Recess height, H_R	0.05
Box width, W_B	0.59

Table 4.1: Geometry parameters kept constant during all experiments

At different locations inside the moonpool wave probes were mounted in order to extract surface elevations. Two types of wave probes were used in the experiments. Above the moonpool, traditional wave probe rods were mounted to brackets that spanned across the moonpool. By this, measurements of surface elevations were done in the model fixed coordinate system. At the model walls, conductive aluminum tape were glued on, to measure the surface elevations against the walls. The principle of both are similar. Voltage is applied to the rod or tape, and resistance is a function of the submerged part of the probe. By measuring the current, the surface elevation is obtained. The two types of wave measurement systems are shown in Figure 4.2.

(a) Traditional wave probe (b) Tape probes

Figure 4.2: Two different types of wave measurement systems were used in the experiments.

Figure 4.3 and 4.4 shows the locations of the wave probes, both in top and side view respectively.

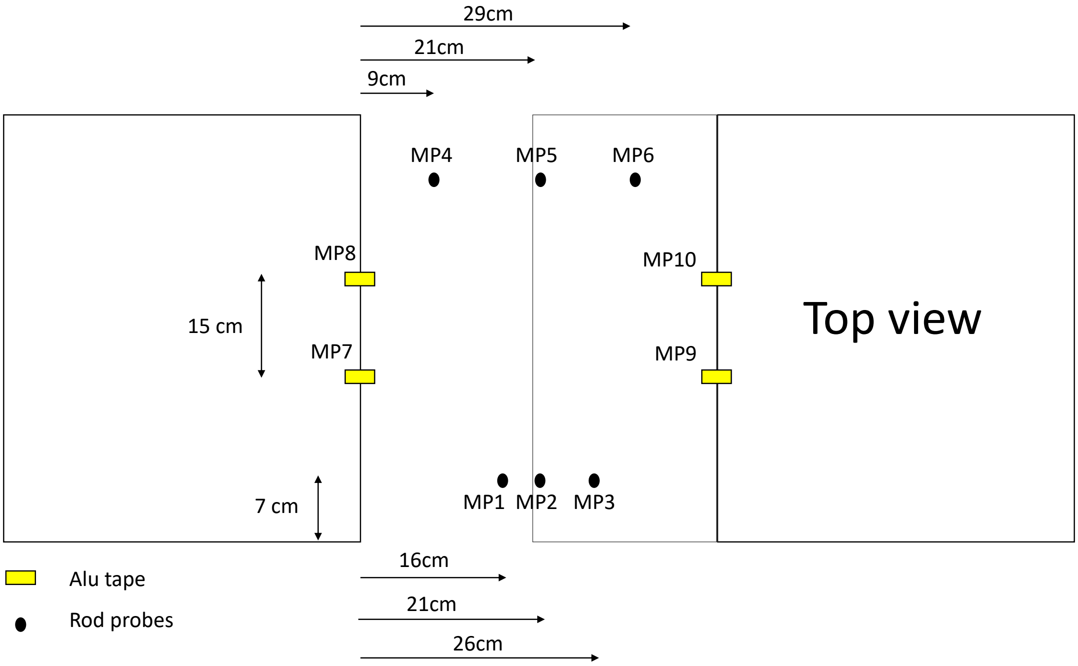

Figure 4.3: Top view of wave probe locations, showing the rod probes(MP1-MP6) as block dots and alu tape probes(MP7-MP10) in yellow

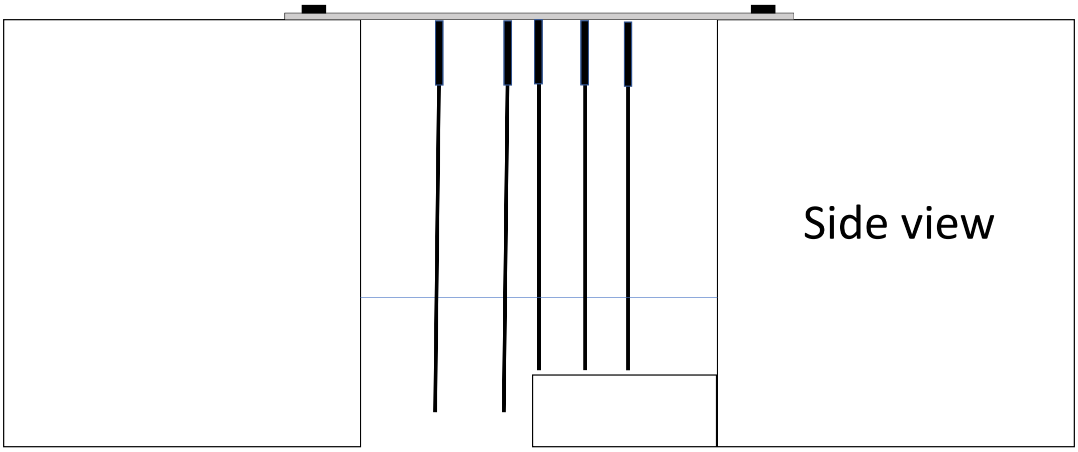

Figure 4.4: Side view of wave probe(rods) locations

4.2 Test matrix

Prior to doing laboratory experiments, detailed planning is necessary. This is to reduce the risk of mistakes, and to make sure one spend the available time as efficient as possible. An important aspect of experiment planning is to construct a compact and relevant test matrix. The researcher must ensure that the test matrix provides the desired results. The experiments presented in this thesis focuses on both piston mode and the first sloshing mode. Hence, the test matrices had to be concentrated around these resonant periods. To establish the test matrices, the theory presented in Section 2.2.1 was utilized. There were in total constructed six test matrices, one matrix for each recess length around the piston mode period, and one matrix for each recess length around the first sloshing mode period.

As an example, Table 4.2 shows the test matrix for recess length of 0.2m with draft of 0.1m, around the first sloshing mode natural period. All such tests were carried out for all forcing amplitudes.

Periods [s]								
0.6	0.65	0.7	0.7598	0.7798	0.7998	0.8198	0.8398	0.8598
0.8798	0.8998	0.9198	0.9398	0.9598	1	1.1	1.2	

Table 4.2: Example of test matrix, for sloshing experiments with L_R = 0.2m and T = 0.1m

Figure 4.5 show how one generated input time series look, accounting for the displacement effect cause by the model.

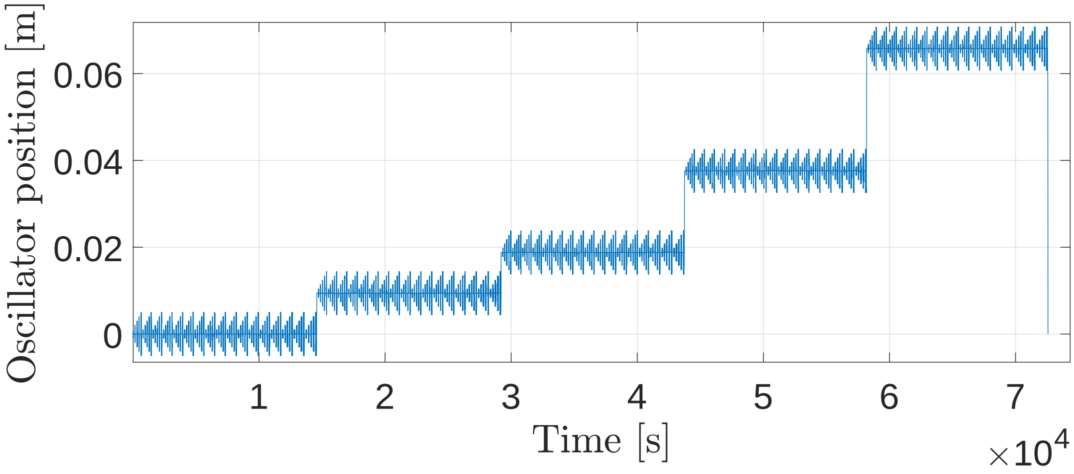

Figure 4.5: Example of input oscillator time series.

4.3 Post precessing

After the experiments were done, raw data time series were obtained for all measurement instruments that were mounted during setup. The post processing consists of extracting the harmonic signals from the time series, by filtering out frequencies outside some percentage of the excitation frequency using a band-pass filter. First the given oscillator frequencies were found, by analyzing the time series measurements of the oscillator rig. This was done by carrying out a Fast Fourier Transform(FFT) analysis for each run and input frequency. The procedure is shown in Figure 4.8.

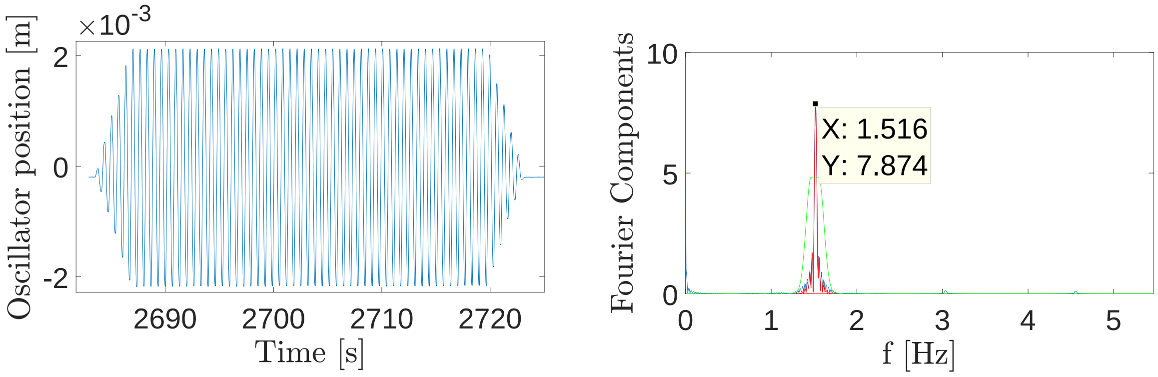

(a) Oscillator time series

(b) FFT of time series in a

Figure 4.6: Procedure for obtaining output oscillation periods for oscillator

A phenomena observed when processing the wave probe time series, are beats. These beats occur as the forcing frequency approach the natural frequency. The forcing frequency excites the natural frequency, and the result is visualized in Figure 4.7. The beating period is expressed as

$$T_{beat} = \frac{1}{|f - f_n|} \tag{4.1}$$

where f is the forcing frequency and f_n is the natural frequency. The beating phenomena is related to the viscous damping in the fluid. If there was no viscosity, the beating oscillations would not die out. However, as seen in Figure 4.7, the phenomena vanishes after some time.

As the forcing frequency approaches the natural frequency, one should include the excited resonance oscillations in the post-processing. To do so, the band-pass filtering range must be wide enough to capture both peaks highlighted in Figure 4.8a. The run analysed in Figure 4.8a is for a recess length of 0.1m, draft of 0.17m, forcing frequency of 1.352Hz and forcing amplitude of 0.003m. For this case, the beating period becomes large relative to the overall time-series, as seen from eq. 4.1. In the case analysed in Figure 4.8a the natural frequency f_n is 1.315Hz. This gives a beating period T_{beat} of 27s, as shown in Figure 4.8b. When extracting the average oscillation amplitudes of the probe signals, this should be done over a beating period if possible.

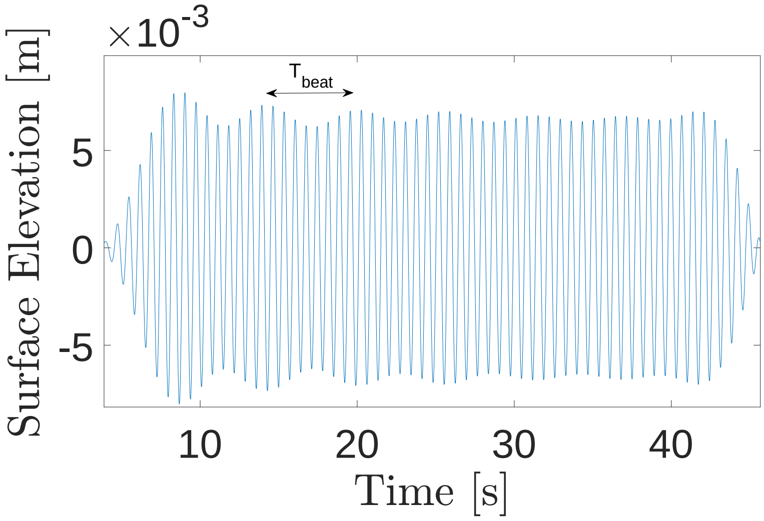

Figure 4.7: Beating signal and beating period. It is seen that the beating signals vanishes, due to viscous damping.

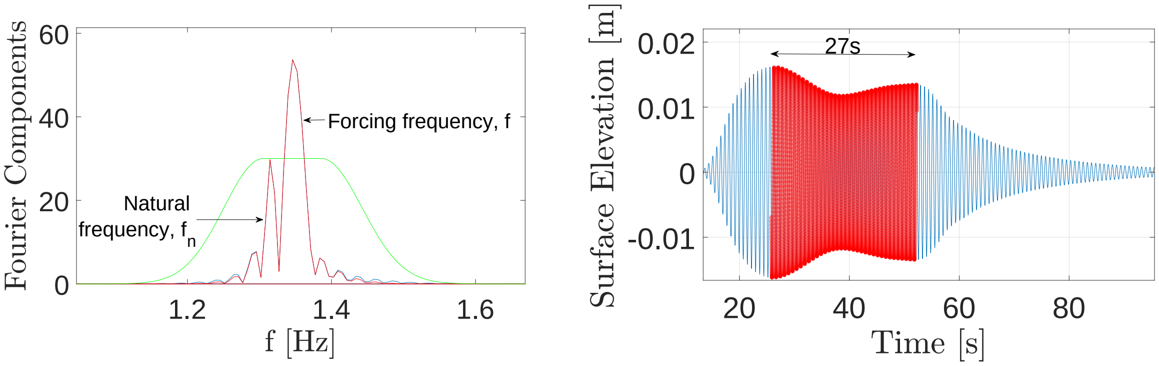

(a) FFT with standard deviation $\beta = 0.05$

(b) Time series with beating period equal to 27s, reaching over most of time series

Figure 4.8: Excitation frequency close the the natural frequency. Green line in(a) is the Gaussian curve defining the band-pass filtering range

Chapter 5

Results and Discussion

This chapter will present the main results found in this master's thesis project. Both experimental and numerical results will be presented and discussed upon. Results are presented in the earth fixed coordinate system.

5.1 Experimental results

In this section experimental results will be presented and discussed upon. As outlined in Section 4, experiments were conducted over two lab periods. As a consequence of that, the presented RAOs are merged to give a more compact picture of the results in terms of figures. To give the reader an overview of the results and the physical features investigated, some illustrative findings will be presented in the following. First, a case where linear features dominates will be presented in terms of RAOs, time series and FFTs. After this, cases showing strong non-linear behaviour because of shallow water effects will be presented. Findings and discussions will be further documented by snapshots from the experiments.

5.1.1 Large draft to recess length ratio

Figure 5.1 shows the RAO at MP1 for 0.1m recess with draft of 0.17m and a forcing amplitude of 0.003m. This is the shortest recess tested in the experiments, at the largest draft. The arrows points at the first sloshing mode and the piston mode resonance peaks, as well as the hump on the left side of sloshing resonance, denoted A. The dashed lines show the estimates of piston mode natural period denoted T_{piston} and the first sloshing mode natural period denoted $T_{sloshing}$, from the matched eigenfunction method in Section 2.2.1.

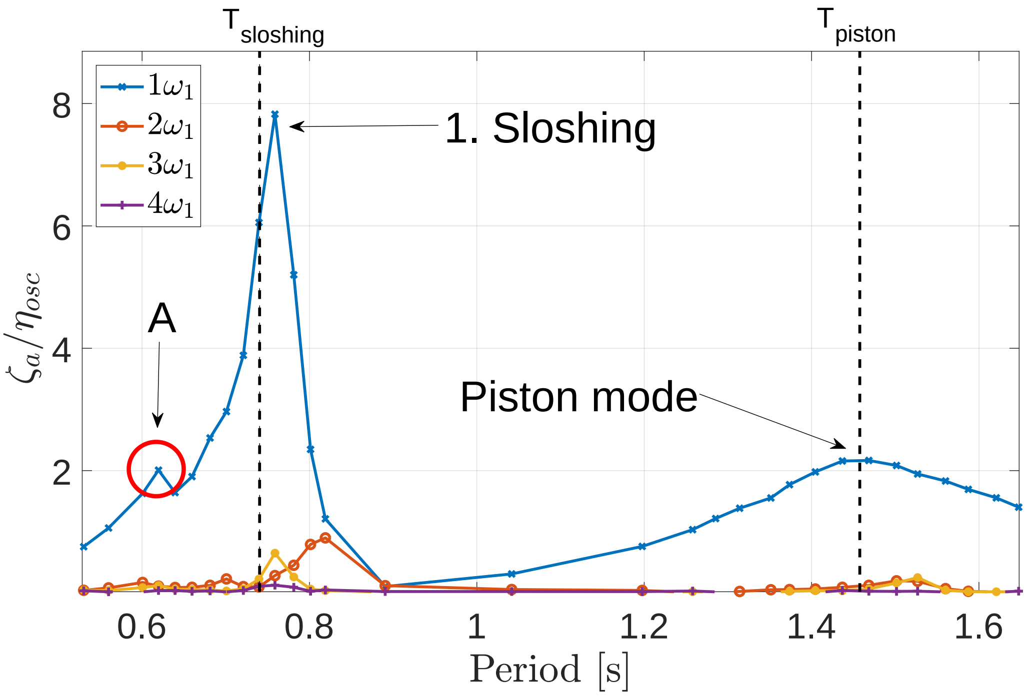

Figure 5.1: RAO at MP1 for L_R 0.1m, T = 0.17m and η_{osc} = 0.003m

In the following the cases pointed out in Figure 5.1 will be presented and described by means of time series and FFTs.

Piston mode

In Figure 5.2 the time series of the run at piston mode resonance is presented, showing contributions of the first three harmonics. Figure 5.2b show how the higher harmonic signals builds up after the first harmonic. The signals are strongly dominated by the first harmonic.

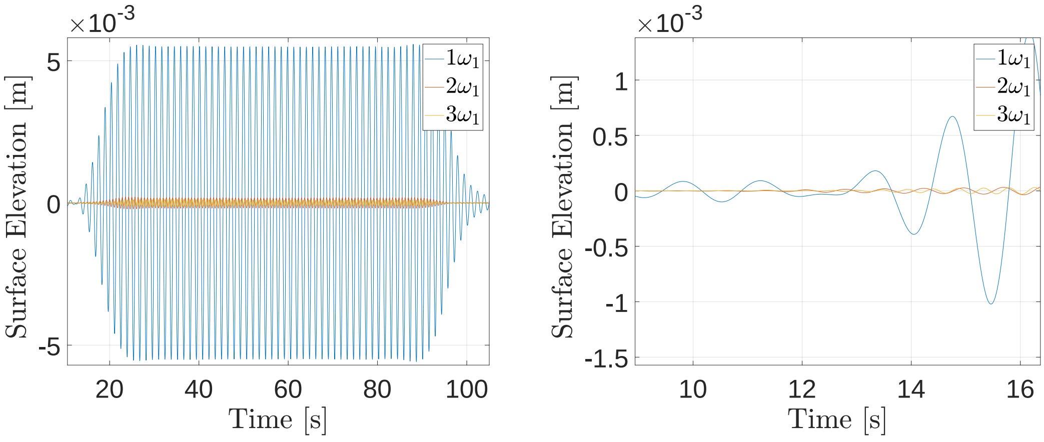

(a) Overview of harmonic oscillations

(b) Zoomed in on a)

Figure 5.2: Harmonic time series of MP1, L_R = 0.1m, T = 0.17m and η_{osc} = 0.003m

Figure 5.3 show the FFT of the time series at piston mode presented in Figure 5.2, with standard deviation $\beta = 0.05$ defining the bandpass Gaussian curve in green. The FFT verifies what is visible from the time series, that the free surface oscillations in this specific case is dominated by the first harmonic frequency.

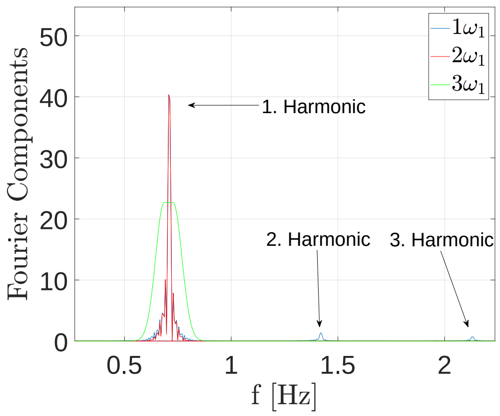

Figure 5.3: FFT of time series in Figure 5.2, with $\beta = 0.05$

1. Sloshing

In Figure 5.4 the time series of harmonic signals for the run at the first sloshing mode resonance period is shown. There is still clear that the first harmonic signals dominate. However, somewhat larger contributions are visible from both the second and the third harmonic signals.

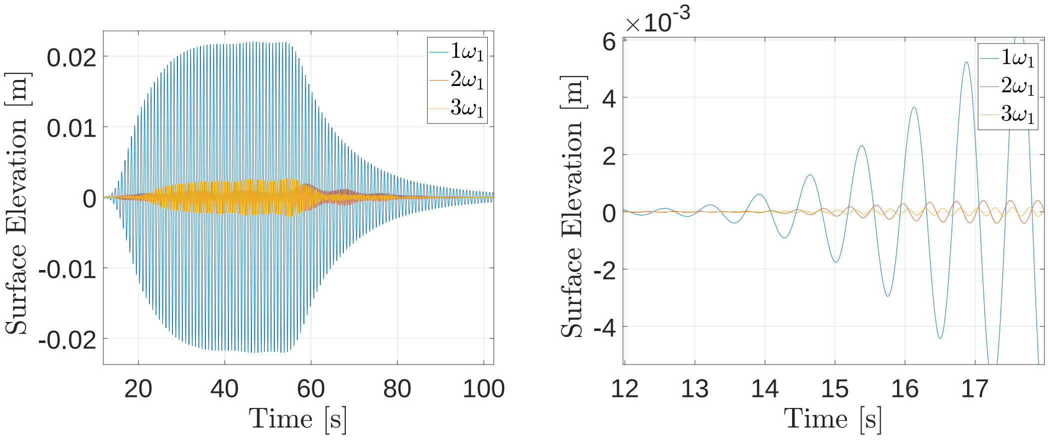

(a) Overview of harmonic oscillations

(b) Zoomed in on a)

Figure 5.4: Harmonic time series of MP1, L_R = 0.1m, T = 0.17m and η_{osc} = 0.003m

Figure 5.5 shows the FFT at the first sloshing mode frequency.

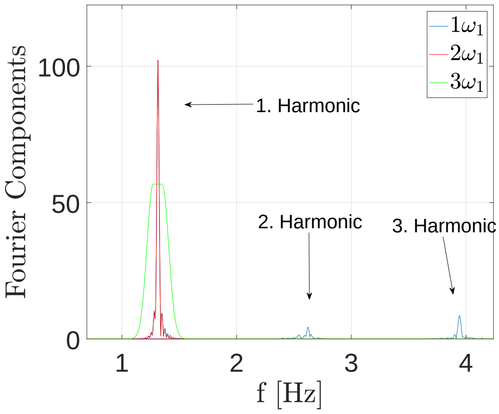

Figure 5.5: FFT of time series in Figure 5.4, with $\beta = 0.05$

Run denoted *A*

One interesting aspect of the RAO presented in Figure 5.1, is the hump pointed out by A. A plausible reason is that transverse sloshing has been excited. Taking the width of the tank as 0.6m and water depth 1m and inserting into eq. 2.70, shows that the natural period of the second transverse sloshing mode of the tank is 0.62s.

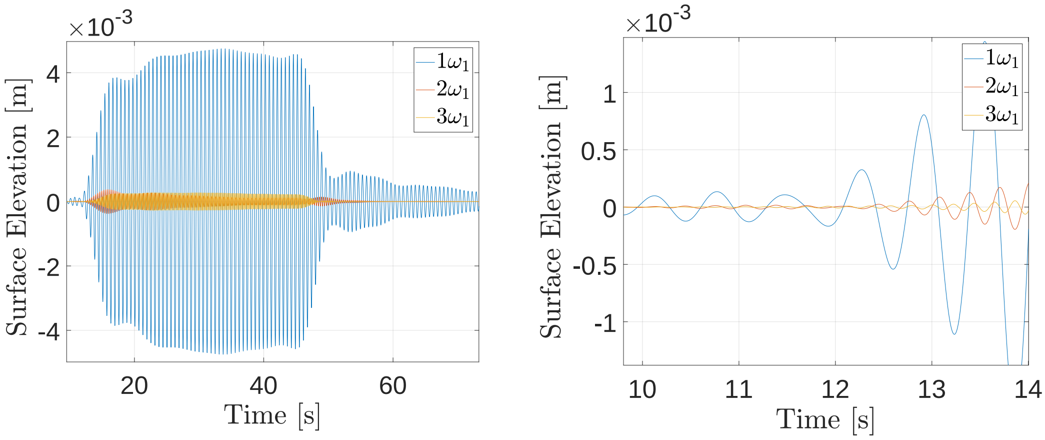

(a) Overview of harmonic oscillations

(b) Zoomed in on a)

Figure 5.6: Harmonic time series of MP1, $L_R = 0.1$m, T = 0.17m and $\eta_{osc} = 0.003$m

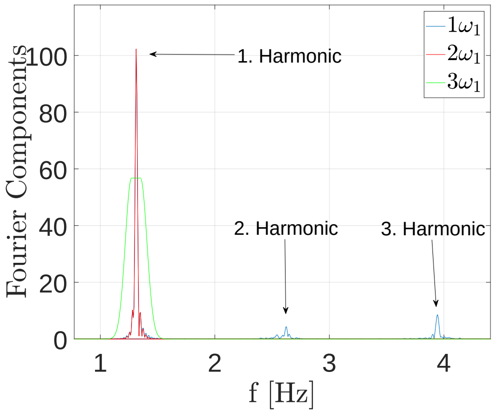

Figure 5.7: FFT of time series in Figure 5.6, with $\beta = 0.05$

5.1.2 Shallow water effects

In the following, results from MP3 with draft of 0.1m, recess length of 0.2m and forcing amplitude of 0.001m will be presented and discussed upon. Figure 5.8 shows the obtained RAO.

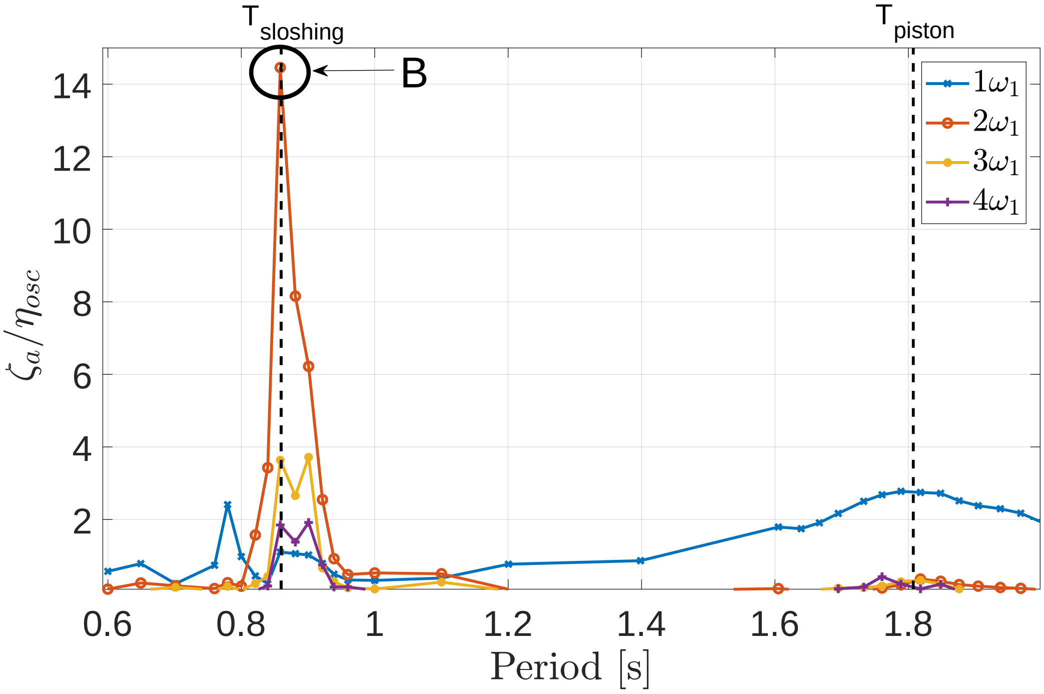

Figure 5.8: RAO at MP3 for L_R = 0.2m, T = 0.1m and η_{osc} = 0.001m

The peak denoted B highlights that resonance at the second harmonic is excited, pretty much exactly at the estimate of the first sloshing mode period. Judging from the results of the more linear case in Figure 5.1, there are some deviations between the estimate and the real natural periods. But the fact that the second sloshing mode is exited at the estimated first sloshing mode period, corresponds well with what was given in Section 2.4.1 by Faltinsen and Timokha (2009) on shallow and intermediate water sloshing in planar rectangular tanks. With the limits of h/l as defined in Table 2.2, the present case is in the intermediate water sloshing region and close to shallow water sloshing, dependent on how l is defined with depth above the recess being 0.05m. If l is taken as the length of the recess, h/l = 0.25. If l is taken as the length of the moonpool, h/l = 0.125. According to Faltinsen and Timokha (2009), eq. 2.70 is applicable for a few of the lowest natural modes, when in the intermediate region. Solving the equation for the first five natural modes, give results presented in Table 5.1.

Mode, i	1	2	3	4	5
l = 0.2m	0.6250s	0.3737s	0.2949s	0.2536s	0.2264s
l = 0.4m	1.1710s	0.6250s	0.4545s	0.3737s	0.3265s

Table 5.1: Estimates of natural period of the first five modes, using eq. 2.70

Neither by taking l equal 0.2m or 0.4m seems to match very well with experiments or the estimates. Actually, the estimates from Section 2.2.1 falls in between the estimates in Table 5.1. In Table 5.1 for both values of h/l, the ratio between the first two sloshing modes are 1.6725 and 1.8736 respectively. That is, the ratio is not 2 as in Figure 5.8. It is unclear for the author whether it is some deviation of the estimates to the real natural period, or that the recess case obviously differs from a tank case, that makes the second sloshing mode period exactly twice the estimated in the experiments.

Since barely no first harmonic signals are observed in Figure 5.8, other wave probes should be checked in order to discuss the harmonic signals. From Figure 5.9 the RAO of MP1 is presented, showing more first harmonic signals than at MP3. This points towards that MP3 is close to a node of the first sloshing mode.

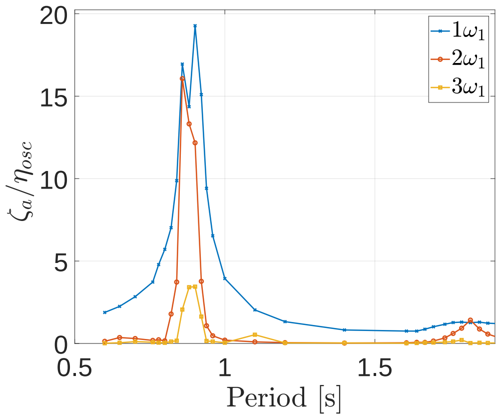

Figure 5.9: RAO at MP1 for L_R = 0.2m, T = 0.1m and η_{osc} = 0.001m

Figure 5.10 presents the time series from the run highlighted by B. It is clear that the second harmonic signals are dominating. However, one could also see from Figure 5.10b that the higher harmonics are excited after the first harmonic as expected.

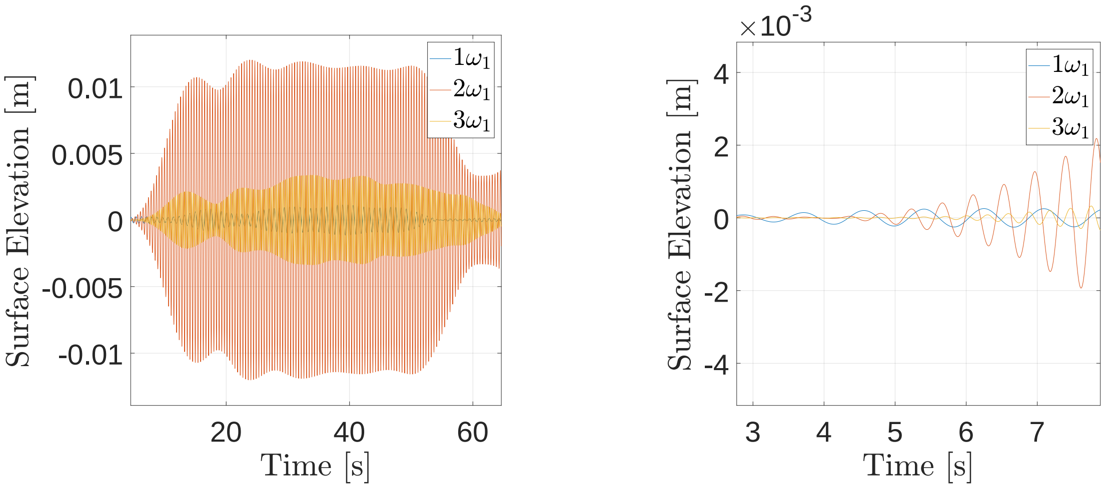

(a) Overview of harmonic oscillations

(b) Zoomed in on a)

Figure 5.10: Harmonic time series of MP3, L_R = 0.2m, T = 0.1m and η_{osc} = 0.001m

Figure 5.11 shows the FFT of the case in B. This verifies what is seen by the time series in Figure 5.10. It also indicates that the third harmonic also is excited with more energy than the first. Since in this case we have the longest recess and smallest draft, the shallow water sloshing theory presented by Faltinsen and Timokha (2009), should be closer to being applicable. If it is recalled that when h/l approach zero, the harmonics become multiples of the lowest natural frequency, the findings from Figure 5.11 makes sense.

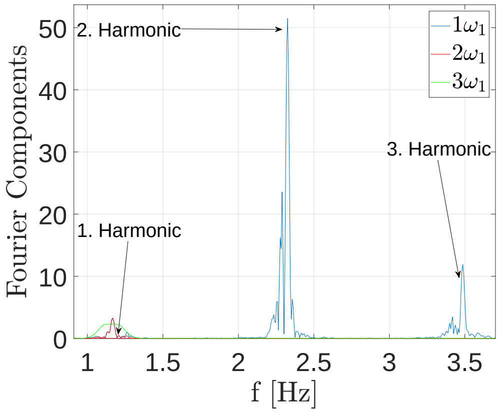

Figure 5.11: FFT of time series in Figure 5.10, with β = 0.05

In Figure 5.12a a snapshot from the resonance peak highlighted by B in Figure 5.8 is shown. One sees clearly from the snapshot that the surface profile oscillates close to the second sloshing mode, which is what Figure 5.8 tells. Figure 5.12b shows a snapshot from a run at piston mode resonance. Clearly, there is not much amplification. The consistency with the findings by Faltinsen et al. (2007) for clean moonpools is good, and will be discussed in more detail later.

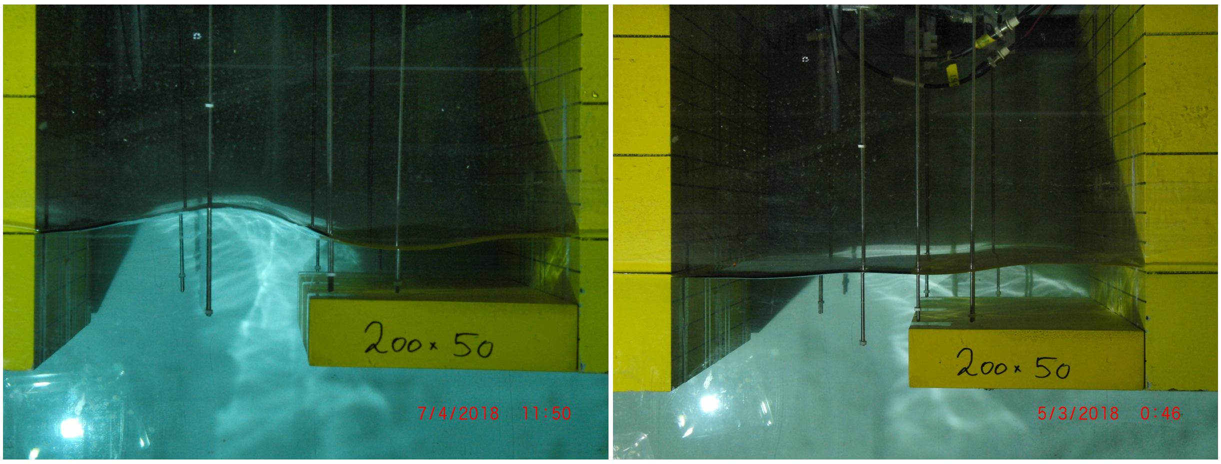

(a) Snapshot from run with L_R = 0.2m, T = 0.1m, Period = 0.8584s and η_{osc} = 0.001m

(b) Snapshot from run with L_R = 0.2m, T = 0.1m, Period = 1.8074s and η_{osc} = 0.003m

Figure 5.12: Snapshots from experiments with with T = 0.1m and L_R = 0.2m

As it is difficult to observe the first harmonic piston mode oscillations by looking at Figure 5.12b, Figure 5.13 shows the mode shape of the oscillations by plotting the first harmonic RAO for wave probes across the moonpool length. The finding is consistent with Molin (2017), and shows that the piston mode amplification is largest against the wall above the recess. Figure 5.14 shows the mode shape of of the run in snapshot Figure 5.12a, indicating a node at the position of MP3.

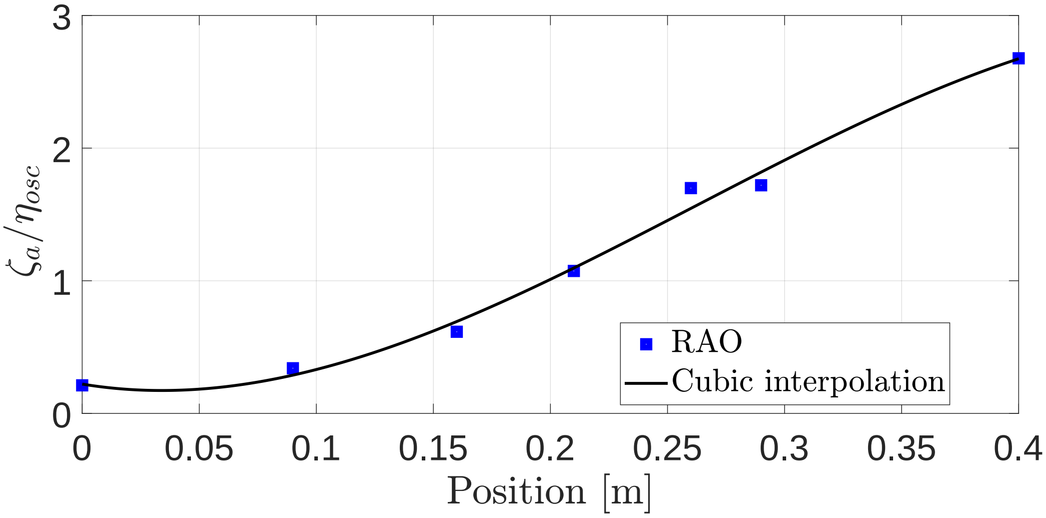

Figure 5.13: Mode shape at piston mode resonance as shown by snapshot in Figure 5.12b, obtained by a cubic regression of the RAO of MP1, MP2, MP3, MP4, MP6, MP7 and MP9 at their respective locations

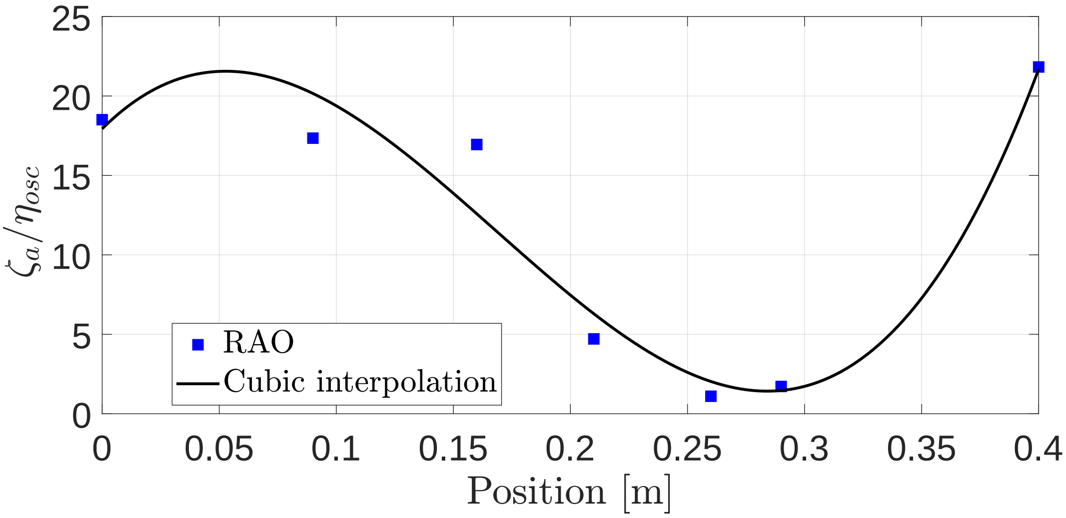

Figure 5.14: Mode shape at sloshing mode resonance as shown by snapshot in Figure 5.12a, obtained by a cubic regression of the RAO of MP1, MP2, MP3, MP4, MP6, MP7 and MP9 at their respective locations

In Figure 5.15 RAOs for all runs are presented, for MP3. These plots lays the foundations for a discussion on the main findings from experiments in Section 5.1.3. For closer detailed investigation of the RAOs, reference is made to Appendix E.

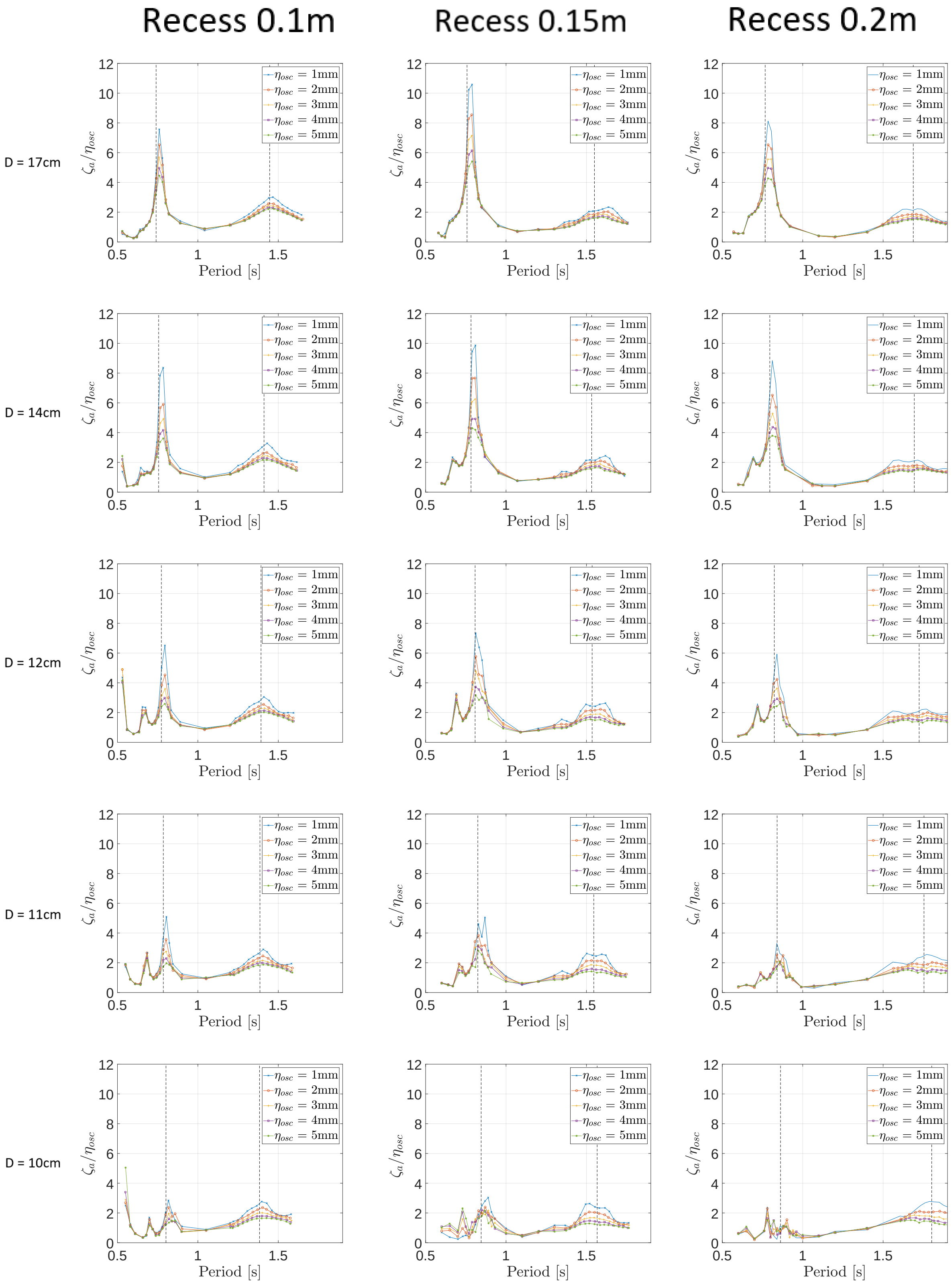

Figure 5.15: RAO at MP3 for all three recess lengths, also showing dependency of draft and amplitude. Dashed lines indicate the estimates for 1. sloshing mode(left) and piston mode(right) natural periods

5.1.3 Discussion on main findings on effect of draft, recess length and forcing amplitude

After presenting the comparisons of the RAOs at MP3 for all recess lengths, drafts and amplitudes in Figure 5.15, a discussion will follow to point out the main findings in relation to the effect of recess length, draft and forcing amplitude. Reference is also made to Appendix E where the RAOs for MP1, MP2, MP4, MP6, MP7 and MP9 are also presented in larger size, to show results at all positions in the longitudinal direction of the moonpool.

The dependency of draft is that the RAOs of the first sloshing mode are generally decreasing for decreasing draft. However, at MP3 for recess length 0.2m and 0.1m, the RAO is slightly larger at 0.14m draft, than 0.17m. For drafts below 0.14m, all RAOs are gradually decreasing. While above the recess at MP3 the largest amplification is obtained for recess length of 0.15m, the largest amplification above the opening at MP1 occurs for recess length of 0.2m. It is also seen that the effect of draft is most pronounced above the recess at MP3. The first sloshing mode resonance peak above the opening at MP1, is not equally decreasing for decreasing draft. As highlighted, it should be noted that MP3 is close to a node of the first sloshing mode.

The resonance periods are decreasing for increasing draft, which is consistent with the estimates from Section 2.2.1. There does seem that the estimates from theory are slightly smaller than reality, especially for the first sloshing mode. Since the piston mode hump is relatively wide, it is difficult to by certain means say if the estimates are exact or not for all cases. For larger drafts where the piston mode hump is more peaked, the estimated natural periods are also lower than in the experiment.

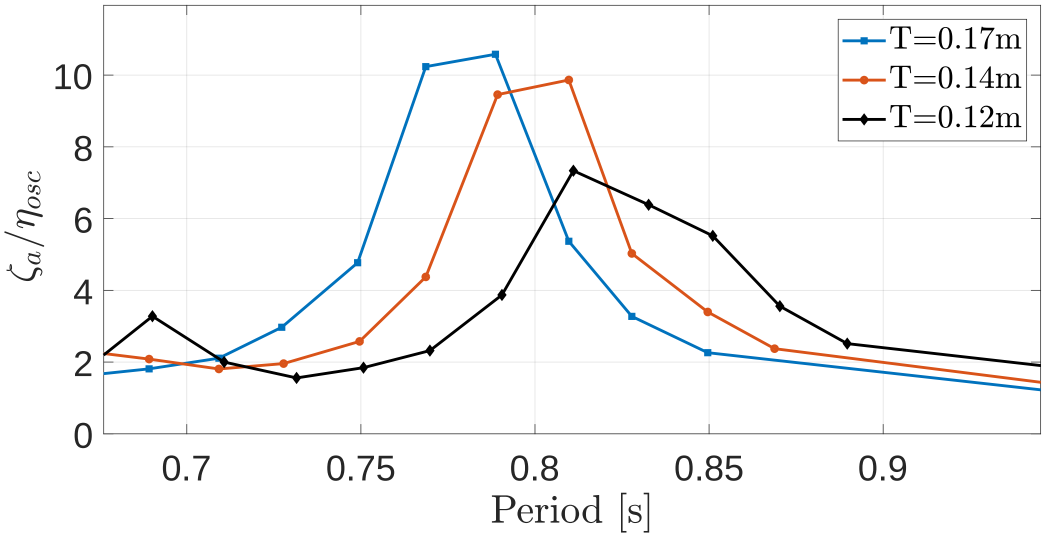

Figure 5.16: Depenency of draft on resonance period of first sloshing mode for recess 0.15m

Recess length affect the flow inside the moonpool. An interesting observation is that the largest amplification at MP3 is obtained for recess length 0.15m. The reason for this is unclear. The sloshing motions are excited by the presence of the recess, which could point towards largest amplification at the largest recess. However, it is seen that with the largest recess more higher harmonic modes are excited due to shallow water effects, as seen in Figure 5.17. Also the fact that the recess has a blockage effect that increase with length, will obviously effect the amplification at resonance. The combinations of these effects could possibly describe why the medium sized recess produces the largest amplification.

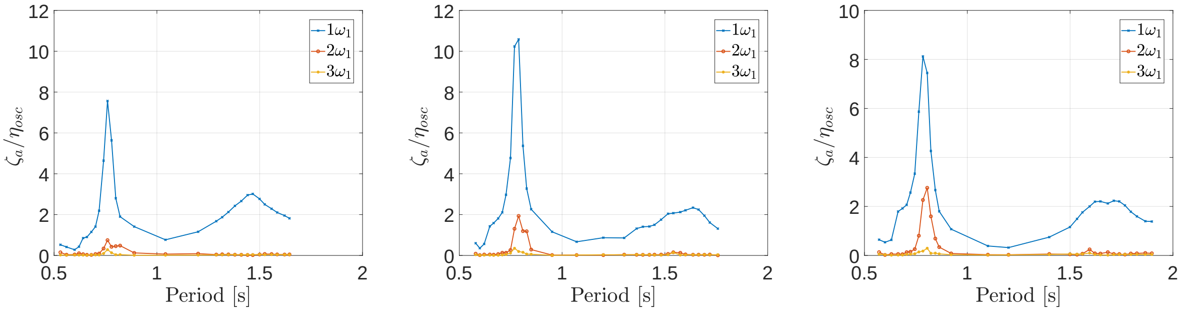

(a) $L_R = 0.1$m (b) $L_R = 0.15$m (c) $L_R = 0.2$m

Figure 5.17: RAO for all recess lengths, showing the difference in harmonic oscillations at MP3 with T=0.17m and $\eta_{osc} = 0.001$m

The effect of the forcing amplitude on excitation of higher harmonics compared to the first harmonic, does not seem to be very pronounced by investigating Figure 5.18. The effect of viscous damping on the RAOs is however clear. The viscous damping is proportional to velocity, hence one should expect RAOs to be higher at the smallest forcing amplitudes.

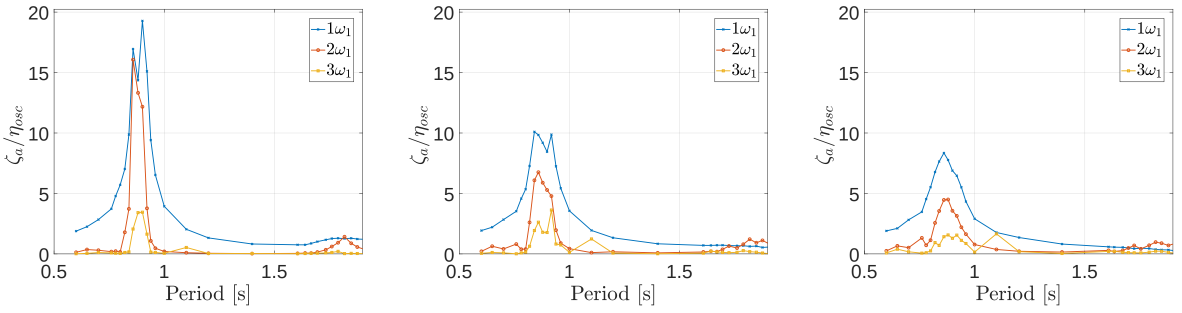

(a) $\eta_{osc} = 0.001$m (b) $\eta_{osc} = 0.003$m (c) $\eta_{osc} = 0.005$m

Figure 5.18: Harmonics at MP1 with recess length of 0.2 and draft of 0.1m, showing effect of forcing amplitude

In addition to the findings related to the mentioned parameters, it is obvious that not much amplification is present at piston mode resonance. This is consistent with what Faltinsen et al. (2007) found for a clean moonpool with ratio between hull box length L_B and moonpool gap length L_G equal to 1.

From private conversation with Ravinthrakumar(2018), it is known that duffing oscillations has been observed in similar experiments as those conducted in this thesis. Figure 5.19 shows examples of duffing oscillation in the present experiment compared with results obtained by Ravinthrakumar(2018). Results from the present experiments shows the same sudden drop after the resonance peak. From comparing with the results in Fig 5.19b, it is clear that finer period steps should be used in order to obtain more details. It should be noted that the results in Figure 5.19b is for a moonpool gap of 0.2m and only presented to highlight the need for finer period steps.

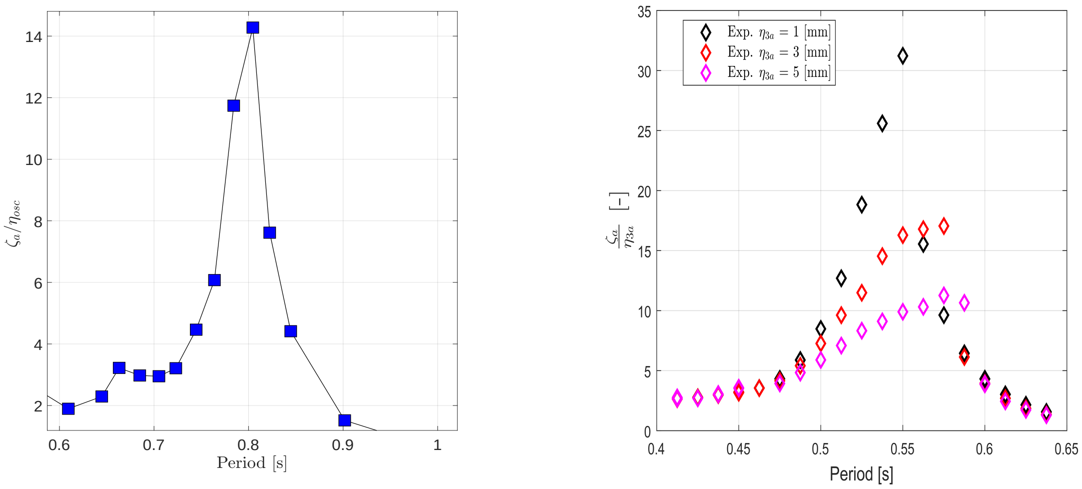

(a) Duffing in present experiments with coarse period steps , with recess length of 0.1m and draft of 0.11m

(b) Duffing for moonpool gap of 0.2m, recess length of 0.1m and draft of 0.11m, provided by Ravinthrakumar(2018)

Figure 5.19: Comparison between duffing oscillations observed in present experiments(a), compared with results obtained with finer period steps by Ravinthrakumar(2018) with different model configuration(b)

5.1.4 Discussion on the applicability of shallow water theory in shallow water zone above recess

A similar approach as taken with the h/l ratio from Faltinsen and Timokha (2009), will be investigated by means of the Ursell-parameter in relation to the shallow water zone above the recess. Some striking differences must be remembered when it comes to the applicability of the parameter in the scope of this thesis. The expression for the Ursell parameter was given in eq. 2.73, and some assumptions must be taken to find values for the parameters L, H and h. If h is taken as the different water depths of the shallow water zone above the recess tested in the experiments, and forcing periods 0.6s and at the first sloshing mode period as examples. Then, we find the wave numbers k from each case with corresponding wave lengths L as

$$\frac{\omega^2}{g} = k \tanh kh \tag{5.1}$$

$$L = \frac{2\pi}{k} \tag{5.2}$$

This is obviously dubious as eq. 5.1 and 5.2 stems from theory of propagating waves, while the waves inside the moonpool are standing. By this, plots of the two cases are presented in Figure 5.20

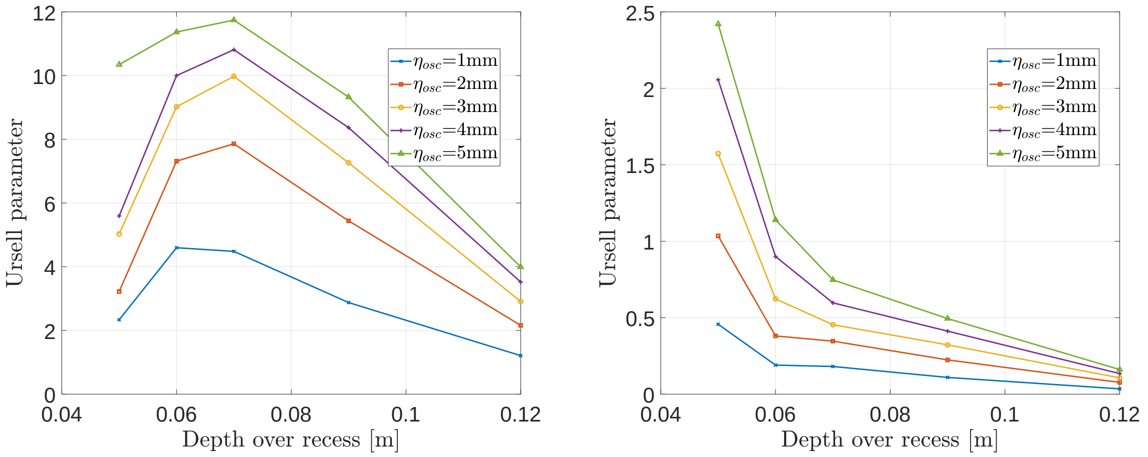

(a) Ursell parameter for forcing period equal the first sloshing mode period

(b) Ursell parameter with forcing period equal 0.6s

Figure 5.20: Ursell parameter for $L_R = 0.2$m, calculated by wave amplitudes from MP3

By comparing with the presented RAOs, the results in Figure 5.20a matches fairly well with what is seen from the investigation of harmonics at sloshing resonance and visually from experiments. The Ursell paramater is well above 1, the free surface is non-linear, and not described by linear theory. For the lower periods Figure 5.20b indicates that a transition could exist for the lower amplitudes at larger drafts, which is also consistent with theory. As the limit presented in Section 2.4.2 is $U \ll \mathcal{O}(1)$, it is not perfectly clear where this transition could exist.

5.1.5 Discussion on error sources in experiments

To carry out a proper analysis of the error in the experiments, one usually distinguish between two sorts of error. The first of them is called bias error, which includes systematic errors. That is, errors that will not change or disappear by doing repeated testing. The second source of error is called scatter or precision error. This is random error, which is the reason why one never should expect the exact same results from repeated tests. To determine the precision error, repeated test must be executed. When a sufficient number of tests are repeated, the standard deviation of the results are found by assuming that measurement values follow a Gaussian distribution. The procedure is thoroughly described in Steen (2014). After doing a finite number of test, the mean is estimated as the average of the measurements. Then one finds an expression for the standard deviation of measurement values.

While executing the experiments presented in this thesis, no repeated runs were executed. However, repeated tests were carried out by Ravinthrakumar et al. (2018) for a similar experimental setup. Forced heave experiments with 0.2m moonpool gap and recesses of

0.05m and 0.10m were repeated eight times. Results in terms of RAOs proved to match well between repeated runs, and a maximum difference of 2% was found. The experiments were executed in the same laboratory as the present experiments, using the same measurement systems.

Transverse sloshing and other 3D effects

As the model used in the experiments had a width of 0.59m, a gap was left between the model and the basin walls of 5mm at each side. This enabled water to flow in between the model and the basin walls, which introduces some 3D effects. Also, as discussed transverse sloshing in the tank was possibly excited. It was pointed out by A in Figure 5.1 that the the second sloshing mode of the tank was 0.62s. The first transverse sloshing mode is approximately 0.88s, which is close to the first sloshing mode natural period of the moonpool. The longitudinal sloshing modes of the tank is well outside the ranges experiments were conducted for, and not a relevant source of error.

Parabolic beaches

In each end of the basin parabolic beaches were mounted to damp out and avoid reflecting waves interfering with the model. From private conversations with Professor Trygve Kristiansen(2018), it was known from best practice that a submergence of around 2mm was ideal for the beaches. With the automated experiments being conducted for five different drafts, a compromise was made with regards to beach submergence. However, this is not expected or seen as a large source of error.

Wave probes and measurement systems

Wave probes used in the experiments have from experience proved to be prone to changes in the temperature. Experiments were conducted over two test periods, with piston mode experiments conducted in the beginning of March 2018 and sloshing experiments in the beginning of April 2018. The temperature was fairly constant during each period, and also no large changes between the lab periods either. Some drift were experienced for some of the wave probes, and this was adjusted for in the post-processing.

Model stiffness and vibrations

The oscillator and model were connected through an arm, reaching from the oscillator to the rig fastened to the model. The size and length of the model meant that the moment arm was large. For all runs at the smallest drafts, there were no vibrations visible by analyzing the accelerometer data. One thing that did seem to cause vibrations in the model, was when sloshing resonance was excited especially at the two largest drafts.

5.2 Numerical results

In this section numerical results will be presented in terms of PVC3D simulations, as described in Chapter 3. The results are presented along with comparisons with experimental results, to examine the applicability of PVC3D given the linear free surface conditions in the code. In the preceding, attention is paid to how well PVC3D reproduce the response around the first sloshing mode natural period, with recess length of 0.2m at the position of MP3 in Figure 4.3. This recess length is chosen as it proved to introduce the strongest non-linear moonpool flows in Section 5.1. Some different refinements is investigated, starting with an initial mesh. All refinements use a level three refinement box around the model, as described in Chapter 3. The cases investigated are presented in Table 5.2. The initial mesh denoted case 1 in Table 5.2, has N_{X0} = 300 cells in the x-direction and N_{Y0} = 20 cells in the y-direction of the background mesh generated by *blockMesh* in Section 3.4.

Case	Refinements	Draft 0.12m	Draft 0.17m
1	$1 \cdot N_{X0}, 1 \cdot N_{Y0}$	15 134 cells	16 068 cells
2	$1.5 \cdot N_{X0}, 1.5 \cdot N_{Y0}$	32 368 cells	34 018 cells
3	$2 \cdot N_{X0}, 2 \cdot N_{Y0}$	57 684 cells	61 360 cells
4	$3 \cdot N_{X0}, 3 \cdot N_{Y0}$	129 578 cells	

Table 5.2: Mesh refinements investigated, showing number of cells for each 2D case with recess length 0.2m. N_{X0} = 300 and N_{Y0} = 20

From Figure 5.21 it is seen that the dependency of mesh is clear. For case 3 mesh in Figure 5.21c the PVC3D produce a resonant peak that is 2.18% higher than the experiments. This is a level of deviation one usually should expect from similar comparisons between PVC3D and experiments, which from private communication with Professor Trygve Kristiansen is said to be around 2 %. PVC3D is also precise when is comes to the natural period, with only a slight phase shift between the experimental results and PVC3D. This is not seen to be dependent on the refinement cases investigated.

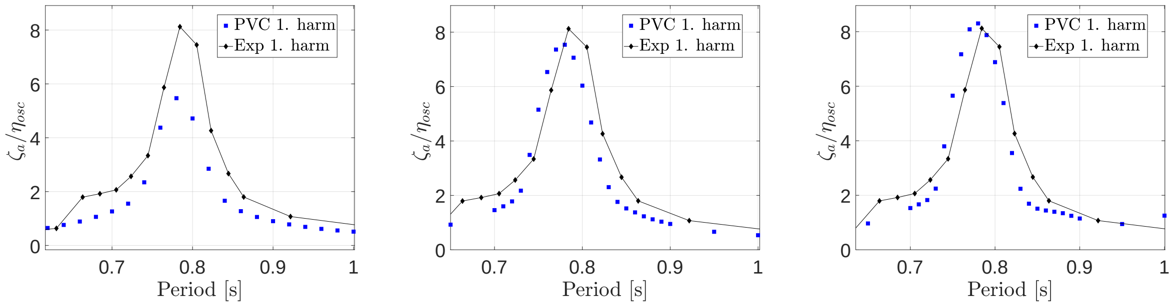

(a) Case 1 with T = 0.17m (b) Case 2 with T = 0.17m (c) Case 3 with T = 0.17m

Figure 5.21: Effect of refinement for T = 0.17m and L_R = 0.2m, at MP3. RAOs show response with forcing amplitude η_{osc} = 0.001m

Figure 5.22 shows how the RAO from PVC3D compare with experiment for draft of 0.12m, with refinement cases as presented in Table 5.2. Clearly the same refinement levels does not produce equally satisfactory results, when the draft is decreased.

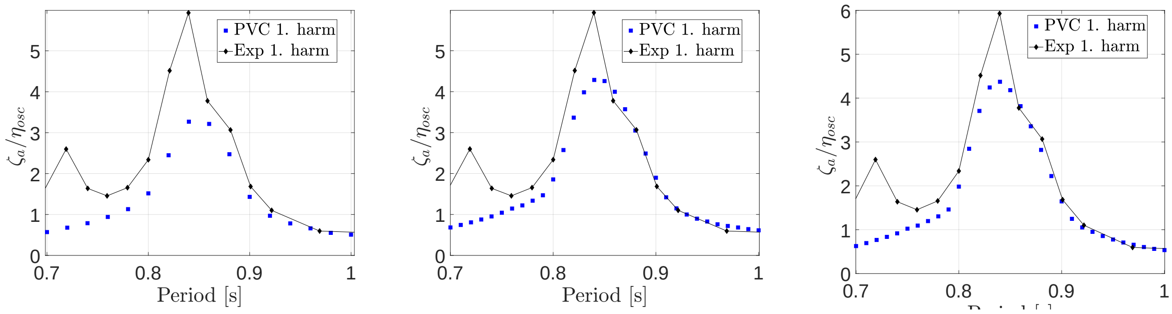

(a) Case 1 with T = 0.12m

(b) Case 2 with T = 0.12m

(c) Case 3 with T = 0.12m

Figure 5.22: Effect of refinement for T = 0.12m and L_R = 0.2m, at MP3. RAOs show response with η_{osc} = 0.001m

In order to complement the findings for draft of 0.12m in Figure 5.22 in the preceding discussions on the validity of the PVC3D in the shallow water zone, one final mesh was tested for a few of the periods around first sloshing mode period. Figure 5.23 shows how the numerical results improve with finer mesh. The comparison is made between experiments, case 3, and case 4 refinements, for draft of 0.12m and recess length of 0.2m. Figure 5.23 indicates that with the present base mesh, the experimental results will not be reached with a reasonable refinement. This can probably be due to the strong viscous features exhibited in the shallow water zone.

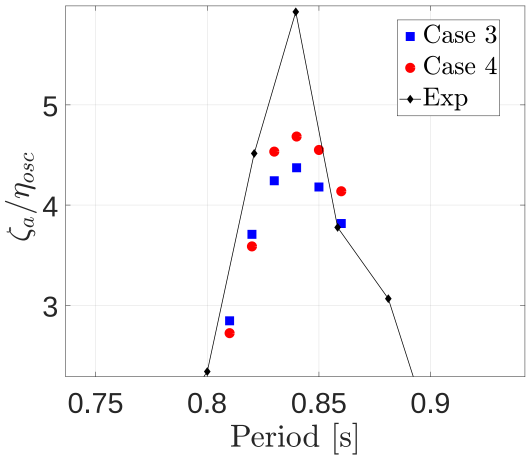

Figure 5.23: Comparison between experiment, case 3 and case 4 refinements, L_R = 0.2m and T = 0.12m at MP3

As seen from experimental findings presented in Section 5.1, the free surface exhibit stronger non-linear behaviour for decreasing drafts. In order to examine the applicability of PVC3D in the shallow water zone above the recess, comparisons should be made on the higher harmonic results. From visualizing the time series from PVC3D simulations, it is seen that the free surface is not perfectly linear. Figure 5.24 shows the time series for a period where higher sloshing modes are strongly excited in experiments.

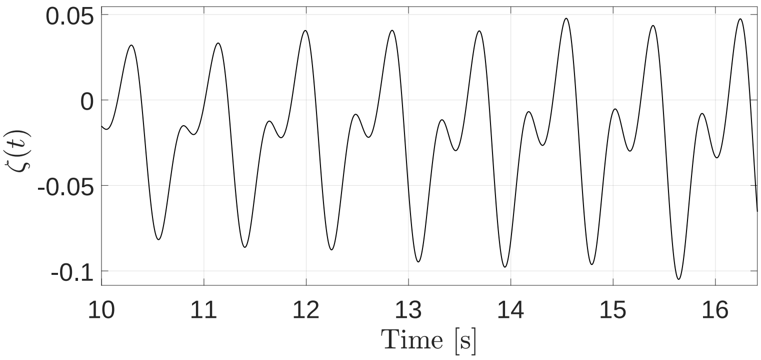

Figure 5.24: Time series from PVC3D with case 3 refinement with forcing period 0.85s where strong second harmonic oscillations are excited in experiments.. L_R = 0.2 and T = 0.12m at MP3

Figure 5.25 shows that PVC3D is not able to capture the second harmonic excited in the shallow water zone in a satisfactory manner. The second harmonic response is shown for both case 3 and case 4 refinements, and no significant improvement is obtained compared to the experimental results.

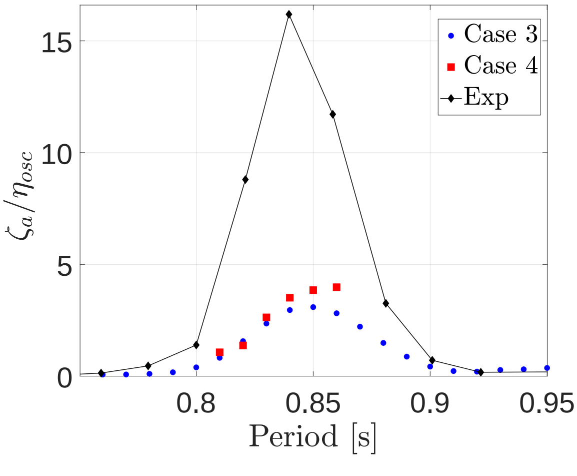

Figure 5.25: Comparison of second harmonic signals from PVC3D with case 3 and case 4 refinement and experiment, with L_R = 0.2m and T= 0.12m at MP3

5.2.1 Discussion on main findings from numerical simulations

This section will discuss the main findings from doing numerical simulations with PVC3D, for moonpool with recess cases. In order to validate the numerical results, experimental findings are used as comparison. The four refinement cases investigated showed that there is a dependency of refinement on the accuracy of the numerical results. Previous simulations on clean moonpools by Professor Trygve Kristiansen have shown that good level of accuracy is obtained for the piston mode resonance, with only 10-15 cells across the moonpool. It makes sense that a larger number of cells are required to describe the sloshing resonance accurately, as the present results show.

Given the violent flow experienced in the experiments for decreasing draft, investigating the effect of draft in PVC3D is important. It is seen from Figure 5.22 that the same refinement that produce good correlation for the largest draft in Figure 5.21, is not sufficient for a draft of 0.12m. For case 3 refinement, the deviation between resonance peak from experiments and PVC3D for the first harmonic is 26.3% for draft of 0.12m. Doing the same simulation with case 4 refinement improve the deviation to 21 %. This improvement has a cost of increased simulation time by a factor of 2.25, which indicates that refinement of the background mesh is not sufficient in order to obtain experimental results. A plausible reason for the large deviations is that PVC3D is not able to handle the viscous effects of decreasing draft.

It is seen from Figure 5.25 that the second harmonic oscillations observed in the experiments are not well captured in PVC3D. Comparisons are made for case 3 and case 4 refinements, and no significant improvement is obtained.

When comparing experimental and numerical results it is important to bear in mind that uncertainties from both parts must be accounted for. There might be numerical wave dispersion errors for some scenarios. Also, uncertainties with regards to experimental setups like draft and measurement systems are plausible reasons for deviations. As no proper convergence study is carried out for these simulations, there could possibly prove to be a need for better refinements for some cases.

The hump observed for periods below the first sloshing mode was discussed in 5.1.3. This hump is again observed for the experiments in Figure 5.22. It is seen that PVC3D does not produce this hump, something that also indicates that this hump is caused by excitation of the second transverse sloshing mode of the tank experiments are conducted in.

Chapter 6

Concluding Remarks and Further Work

The challenges faced in the industry with operational time limited due to resonant motions inside the moonpool, led the foundations for this master's thesis work. This thesis investigates fluid motions inside a moonpool equipped with a recess. The main issues the thesis address is the effect of recess length, draft and forcing amplitude, on the linearity of the free surface and amplification at resonance. Comparisons are made with estimates by utilizing linear potential theory, with special attention paid to matched eigenfunction expansions. The method is applied to both three and six subdomains. Experiments are carried out over two lab periods, for piston mode and sloshing experiments respectively. Results are presented by merging the findings, in terms of RAOs. Numerical results are presented by applying the hybrid code PVC3D, to investigate its applicability. In the following, conclusive remarks are presented, followed by suggestions of further work in Section 6.1.

In Chapter 2 relevant theory is presented. Special attention is paid to potential theory, and it is shown how matched eigenfunction expansions can be utilized. The theory is applied for three subdomains, from which estimates of the natural periods of piston mode and sloshing modes are obtained. An outline of how the theory is applied for six subdomains is also presented, with following preliminary results in terms of RAO. The latter method proved to be very sensitive to bugs, and plots of matched potentials and derivatives in Appendix B indicate some bugs still exists.

From experimental results presented in Section 5.1, it is seen that the water depth above the recess strongly affect the linearity of the free surface. Results are presented in which it is seen that second harmonic oscillations i equally strong as the first harmonic for the lowest drafts, and also higher modes are excited. This is because to the shallow water zone above the recess, and a discussion is made with regards to the theory presented by Faltinsen and Timokha (2009) on shallow and intermediate water sloshing in planar rectangular tanks. The consistency is clear in that higher harmonics are excited when the water depth in the shallow water zone is decreased. The non-linear effects increase with increased recess length.

It is seen that the largest amplifications of the free surface are obtained by the moonpool walls when the first sloshing mode is excited. The largest amplifications are observed for drafts of 0.14m with the longest tested recess length of 0.2m, and RAOs are gradually decreasing with decreasing draft. The largest tested draft of 0.17m, shows slightly smaller amplifications than drafts of 0.14m.

The natural period of the first sloshing mode is found to decrease for increasing drafts. This is consistent with the estimates obtained by implementing the theory of Molin (2017) in Chapter 2, with matched eigenfunction expansions in three subdomains. Results showed that the estimates were somewhat lower than the natural periods observed in the experiments. The RAO obtained by implementing the six domain approach of matched eigenfunction expansions presented in Section 2.2.2, predicted the resonant peaks more precisely. The reason for this is probably that the latter accounts for the outer free surface.

At piston mode, not much amplification was observed. This is consistent with what Faltinsen et al. (2007) found for clean moonpools. It was shown by a mode shape plot that the piston mode amplitudes were largest against the wall above the recess, as pointed out by Molin (2017).

Results from numerical simulations were presented in Section 5.2. PVC3D was implemented for moonpool with recess cases, to investigate the applicability of the code given the strong non-linear features illustrated in the experimental results. Simulations were done for recess length of 0.2m, and for drafts of 0.17m and 0.12m. Four different refinement cases were tested, and results were compared with experimental results. For 0.17m draft satisfactory results are obtained, with 2.18% deviation between experimental and PVC3D results. From previous comparisons between experiments and PVC3D, such level deviations is common given uncertainties in experimental procedures and possible numerical wave dispersion errors. For draft of 0.12m the same refinement cases that produced satisfactory results for draft of 0.17m, is seen to not be able the capture the resonance peak obtained from experiments. Only a small improvement is obtained between the two finest refinements, for more than twice the computational time. A plot of the time series from PVC3D show that the code is able to produce some non-linear free surface oscillations, for the cases where these features were strong in experiments. However, it is far from sufficient in order to capture the second harmonic oscillation observed in experiments. The improvement of refinements tested during these non-linear simulations are shown to be minimal.

6.1 Further work

This section will suggest possible further work on the topics of moonpool with recess. It will be discussed how the work presented in this thesis can be taken further, and also other topics that might be interesting to investigate.

As presented in Chapter 2, due to restricted time the matched eigenfunction expansion method in six subdomains were not fully debugged. Some bugs were present by deadline of this thesis, and results were presented as preliminary. Upcoming master graduates should attempt to implement the theory with inspiration from this thesis.

Experiments presented in this thesis are done through forced heave oscillations. Following the work in this thesis, freely floating experiments may be investigated. A natural starting point would be two-dimensional experiments, but also three-dimensional freely floating experiments would be interesting.

While this thesis has investigated the effect of geometrical parameters as recess length and model draft, other geometrical configurations could be investigated. In order to investigate the possibility of damping the resonant motions in moonpools with recess, curved inlets or bilge keels at the moonpool inlet might be tested. Some sort of feasibility considerations will be necessary with regards to sharp bilge keels at the inlet, as objects in the moonpool should stay clear of the bilge keel. An engineering approach could be considered, and some sort of protection netting could be considered.

In order to further investigate the applicability of PVC3D in the shallow water zone above a recess, a thorough refinement study should be carried out. This would be necessary to fully understand the applicability in the shallow water zone.

References

Aalbers, A. (1984). The water motions in a moonpool. *Ocean engineering*, 11(6):557–579.

Bredmose, H., Brocchini, M., Peregrine, D., and Thais, L. (2003). Experimental investigation and numerical modelling of steep forced water waves. *Journal of Fluid Mechanics*, 490:217–249.

Cointe, R. and Geyer, P. (1991). Nonlinear and linear motions of a rectangular barge in a perfect fluid.

Çengel, Y. A. (2010). *Fluid mechanics fundamentals and applications*. McGraw-Hill.

Faltinsen, O. (1993). *Sea loads on ships and offshore structures*, volume 1. Cambridge university press.

Faltinsen, O. M., Rognebakke, O. F., and Timokha, A. N. (2007). Two-dimensional resonant piston-like sloshing in a moonpool. *Journal of Fluid Mechanics*, 575:359–397.

Faltinsen, O. M. and Timokha, A. N. (2009). Sloshing.

Faraday, M. (1831). Xvii. on a peculiar class of acoustical figures; and on certain forms assumed by groups of particles upon vibrating elastic surfaces. *Philosophical transactions of the Royal Society of London*, 121:299–340.

Ferziger, J. H. (2002). Computational methods for fluid dynamics.

Fredriksen, A. G., Kristiansen, T. F., and Faltinsen, O. M. (2012). Investigation of gap resonance in moonpools at forward speed using a nonlinear domain-decomposition method. *iwwwfb27*.

Guo, X., Lu, H., Yang, J., Peng, T., et al. (2016). Study on hydrodynamic performances of a deep-water drillship and water motions inside its rectangular moonpool. In *The 26th International Ocean and Polar Engineering Conference*. International Society of Offshore and Polar Engineers.

Haiyang Huang, X. Z. (2018). On natural modes in two-dimensional asymmetric and symmetric moonpools in finite water depth.

Kovacic, I. and Brennan, M. J. (2011). *The Duffing equation: nonlinear oscillators and their behaviour*. John Wiley & Sons.

Kristiansen, T. and Faltinsen, O. M. (2011). Gap resonance analyzed by a new domain-decomposition method combining potential and viscous flow. *Applied Ocean Research*, 34:198–208.

Kristiansen, T., Ommani, B., Berget, K., and Baarholm, R. (2015). An experimental and numerical investigation of a box-shaped object in moonpool; a three-dimensional study. *OMAE 2015*.

Kristiansen, T., Sauder, T., and Firoozkoohi, R. (2013). Validation of a hybrid code combining potential and viscous flow with application to 3d moonpool. In *Proceedings of the ASME 2013 32nd International Conference on Ocean, Offshore and Arctic Engineering (OMAE2013)*.

Larsen, C. (2012). Marin dynamikk: kompendium for bruk i faget tmr 4182 marin dynamikk ved institutt for marin teknikk, fakultet for ingeniørvitenskap og teknologi, ntnu. Technical report, volume UK-2012-09 of TMR4182 Marin dynamikk. Marinteknisk senter, Institutt for marin teknikk, NTNU, Trondheim.

Lin, L., Liang, C., Bin, T., et al. (2010). Comparison of potential flow and viscous fluid models in gap resonance. In *25th Int Workshop on Water Waves and Floating Bodies. Harbin*, pages 1–4.

Linton, C. M. and McIver, P. (2001). *Handbook of mathematical techniques for wave/structure interactions*. CRC Press.

Molin, B. (2001). On the piston and sloshing modes in moonpools. *Journal of Fluid Mechanics*, 430:27–50.

Molin, B. (2017). On natural modes in moonpools with recesses. *Applied Ocean Research*, 67:1–8.

OpenFOAM (2018). OpenFOAM User Guide. `https://cfd.direct/openfoam/user-guide/`.

Ravinthrakumar, S., Kristiansen, T. F., and Ommani, B. (2018). A 2d experimental and numerical study of moonpools with recess. *OMAE2018*.

Reiersen, L. M. U. (2016). Investigation of moonpool resonance as vessel damping device. Master's thesis, NTNU.

Roache, P. J. (1997). Quantification of uncertainty in computational fluid dynamics. *Annual review of fluid Mechanics*, 29(1):123–160.

Sauder, T., Kristiansen, T., Ostman, A., et al. (2010). Validation of a numerical method for the study of piston-like oscillations between a ship and a terminal. In *The Twentieth International Offshore and Polar Engineering Conference*. International Society of Offshore and Polar Engineers.

Steen, S. (2014). Experimental methods in marine hydrodynamics : compendium.

Svendsen, I. A. (2006). Introduction to nearshore hydrodynamics.

Törnblom, J. and Hammargren, E. (2012). Effect of the moonpool on the total resistance of a drillship.

Torres, F. G., Cueva, M., Malta, E. B., Nishimoto, K., and Ferreira, M. D. (2004). Study of numerical modeling of moonpool as minimization device of monocolumn hull. In *ASME 2004 23rd International Conference on Offshore Mechanics and Arctic Engineering*, pages 971–977. American Society of Mechanical Engineers.

Zhu, H., Ding, M., and Li, Y. (2011). Gibbs phenomenon for fractional fourier series. *IET signal processing*, 5(8):728–738.

Appendix A

Matched Eigenfunction Expansions in Three Subdomains

Matching in z = d

Potentials

$$\phi_1 \;=\; \phi_2 \quad \text{on z = d} \tag{A.1}$$

That is

$$A_0 + B_0 + \sum_{n=1}^{N_1} (A_n \cosh\, k_n d + B_n \sinh\, k_n d) \cos k_n x \;=\; C_0 + \sum_{n=1}^{N_1} C_n\, cos\lambda_n x \tag{A.2}$$

To establish expressions for A_0 and A_m.

- Integrate each side from 0 to a in x

$$A_0 a + B_0 a = C_0 a + \sum_{n=1}^{N_2} C_n \frac{\sin \lambda_n a}{\lambda_n} \tag{A.3}$$

Now the properties of orthogonal functions are utilized

$$\int_0^a \cos\, k_m x \cos\, k_n x\, dx = 0 \quad \text{if m} \neq \text{n} \tag{A.4}$$

- Multiply with cos $k_m x$ and integrate each side from 0 to a in x

$$(A_m \cosh\, k_m d + B_m \sinh\, k_m d) \int_0^a \cos^2(k_m x) dx = \sum_{n=1}^{N_2} C_n \int_0^a \cos\, \lambda_n x \cos\, k_m x\, dx \tag{A.5}$$

Eq. A.3 and A.5 can be combined as

$$\overrightarrow{A} + D_B \overrightarrow{B} = M_{AC} \overrightarrow{C} \tag{A.6}$$

where $\overrightarrow{A} = [A_0, A_1, ..., A_{N_1}]'$, $\overrightarrow{B} = [B_0, B_1, ..., B_{N_1}]'$, $\overrightarrow{C} = [C_0, C_1, ..., C_{N_2}]'$, D_B is a (N_1+1) x (N_1+1) diagonal matrix and M_{AC} is a full $(1+N_1)$ x $(1+N_2)$ matrix

Derivatives

$$\begin{aligned} \phi_{2z} &= \phi_{1z} \quad \text{for } 0 \leq \text{x} \leq \text{a} \\ \phi_{2z} &= \ 0 \quad \text{for a} \leq \text{x} \leq \text{a+b} \end{aligned} \tag{A.7}$$

That is

$$\begin{aligned} \frac{D_0}{h} + \sum_{n=1}^{N_2} D_n \lambda_n \cos\lambda_n x \ &= \ \frac{B_0}{d} + \sum_{n=1}^{N_1} k_n (A_n \sinh k_n d + B_n \cosh k_n d) \cos k_n x \quad \text{for } 0 \leq \text{x} \leq \text{a} \\ \frac{D_0}{h} + \sum_{n=1}^{N_2} D_n \lambda_n \cos\lambda_n x \ &= \ 0 \quad \text{for a} \leq \text{x} \leq \text{a+b} \end{aligned} \tag{A.8}$$

- Integrate both sides over their domain of validity as

$$\int_0^{a+b} \phi_{2z} dx = \int_0^a \phi_{1z} dx \tag{A.9}$$

To obtain

$$\frac{D_0}{h}(a+b) = \frac{B_0 \ a}{d} \tag{A.10}$$

The following orthogonal property is utilized

$$\int_0^a \cos\lambda_m x \cos\lambda_n x \ dx = 0 \quad \text{if m} \neq \text{n} \tag{A.11}$$

- Multiply with $\cos\lambda_m x$ and Integrate over domains of validity as

$$\int_0^{a+b} \phi_{2z} \ cos\lambda_m x dx = \int_0^a \phi_{1z} \ cos\lambda_m x dx \tag{A.12}$$

To obtain

$$\begin{aligned} D_m \lambda_m \int_0^{a+b} \cos^2 \lambda_m x dx = \\ \frac{B_0}{d} \frac{\sin\lambda_m a}{\lambda_m} \ + \ \sum_{n=1}^{N_1} k_n (A_n \sinh k_n d \ + \ B_n \ + \ \cosh k_n d) \int_0^a \cos k_n x \cos\lambda_m x \ dx \end{aligned} \tag{A.13}$$

Eq. A.10 and A.13 can be combined as

$$\overrightarrow{D} = M_{DA} \ \overrightarrow{A} + M_{DB} \overrightarrow{B} \tag{A.14}$$

where $\overrightarrow{D} = [D_0, D_1, ..., D_{N_2}]'$, $\overrightarrow{A} = [A_0, A_1, ..., A_{N_1}]'$, $\overrightarrow{B} = [B_0, B_1, ..., B_{N_1}]'$, M_{DA} and M_{DB} are full $(1+N_2)x(1+N_1)$ matrices.

Matching in z = 0

Potentials

$$\phi_1 \;=\; \phi_3 \quad \text{on z} = 0 \tag{A.15}$$

That is

$$A_0 + \sum_{n=1}^{N_1} A_n \cos k_n x = \sum_{n=1}^{N_3} E_n \sin \mu_n (x + b_1) \tag{A.16}$$

- Integrate each side from 0 to a in x

$$A_0 \; a = \sum_{n=1}^{N_3} E_n \int_0^a \sin \mu_n (x + b_1) dz \tag{A.17}$$

The following orthogonal property is utilized

$$\int_0^a \cos k_m x \; \cos k_n x \; dx = 0 \quad \text{if m} \neq \text{n} \tag{A.18}$$

- Multiply by $\cos k_m x$ and integrate each side from 0 to a in x

$$A_m \int_0^a \cos^2 k_m x \; dx = \sum_{n=1}^{N_3} E_n \int_0^a \sin \mu_n (x + b_1) \; \cos k_m x \; dx \tag{A.19}$$

Eq. A.17 and A.19 can be combined as

$$\overrightarrow{A} = M_{EA} \, \overrightarrow{E} \tag{A.20}$$

Derivatives

$$\begin{gathered} \phi_{3z} = \phi_{1z} \quad \text{for } 0 \leq \text{x} \leq \text{a} \\ \phi_{3z} = \; 0 \quad \text{for } -b_1 \leq x \leq 0 \;\&\; a \leq x \leq a + c + b_2 \end{gathered} \tag{A.21}$$

That is

$$\begin{gathered} \frac{B_0}{d} + \sum_{n=1}^{N_1} B_n k_n \cos k_n x = \sum_{n=1}^{N_1} E_n \mu_n \tanh \mu_n (H - T) \sin \mu_n (x + b_1) \quad \text{for } 0 \leq \text{x} \leq \text{a} \\ \frac{B_0}{d} + \sum_{n=1}^{N_1} B_n k_n \cos k_n x = 0 \quad \text{for } -b_1 \leq x \leq 0 \;\&\; a \leq x \leq a + c + b_1 \end{gathered} \tag{A.22}$$

The following orthogonal property is utilized

$$\int_0^a \sin\mu_m(x+b_1)\ \sin\mu_n(x+b_1)\ dx = 0 \quad \text{if m} \neq \text{n} \tag{A.23}$$

- Multiply by sin $\mu_m(x+b_1)$ and integrate over domains of validity

$$\frac{B_0}{d}\int_0^a sin\mu_m(x+b_1)\ dx + \sum_{n=1}^{N_1} B_n\ k_n \int_0^a \cos k_n x \sin\mu_m(x+b_1)\ dx = \sum_{n=1}^{N_1} E_m\mu_m \tanh\mu_m(H-T)\frac{a+b+b_1+b_2}{2} \tag{A.24}$$

$$\overrightarrow{E} = M_{BE}\ \overrightarrow{B} \tag{A.25}$$

Free surface condition in z = h+d

The free surface is governed by the combined free surface condition

$$g\phi_{2z} - \omega^2\phi_2 = 0 \tag{A.26}$$

That is

$$\begin{gathered} \frac{D_0}{h}g + \sum_{n=1}^{N_1}\left[C_n\lambda_n \sinh\lambda_n h + D_n\lambda_n \cosh\lambda_n h\right]\ g\ \cos\lambda_n x = \\ \omega^2[C_0 + D_0 + \sum_{n=1}^{N_1}\left[C_n \cosh\lambda_n h + D_n \sinh\lambda_n h\right]\cos\lambda_n x] \end{gathered} \tag{A.27}$$

- Integrate from 0 to a+c in x

$$\frac{D_0}{h}g = \omega^2[C_0 + D_0] \tag{A.28}$$

- Multiply by $\cos\lambda_m x$ and integrate from 0 to a+c in x

$$\begin{gathered} \left[C_m\lambda_m \sinh\lambda_m h + D_m\lambda_m \cosh\lambda_m h\right]\ g\ \int_0^{a+c} cos^2\lambda_m x\ dx = \\ \omega^2\ \left[C_m \cosh\lambda_m h + D_m \sinh\lambda_m h\right]\ \int_0^{a+c} \cos^2\lambda_m x\ dx \end{gathered} \tag{A.29}$$

Eq. A.29 can be written as

$$C_m \tanh\lambda_m h\ \lambda_m\ g + D_m\lambda_m\ g\ = \omega^2\ \left[C_m + D_m\ \tanh\lambda_m h\right] \tag{A.30}$$

Eq. A.28 and A.30 can be combined as

$$D_1\ \overrightarrow{C} + D_2\overrightarrow{D} = \omega^2(\overrightarrow{C} + D_4\overrightarrow{C}) \tag{A.31}$$

where $\overrightarrow{C} = [C_0, C_1, ..., C_{N_2}]'$, $\overrightarrow{D} = [D_0, D_1, ..., D_{N_2}]'$, D_1, D_2 and D_4 are diagonal matrices.

Appendix B

Matched Eigenfunction Expansions In Six Subdomains

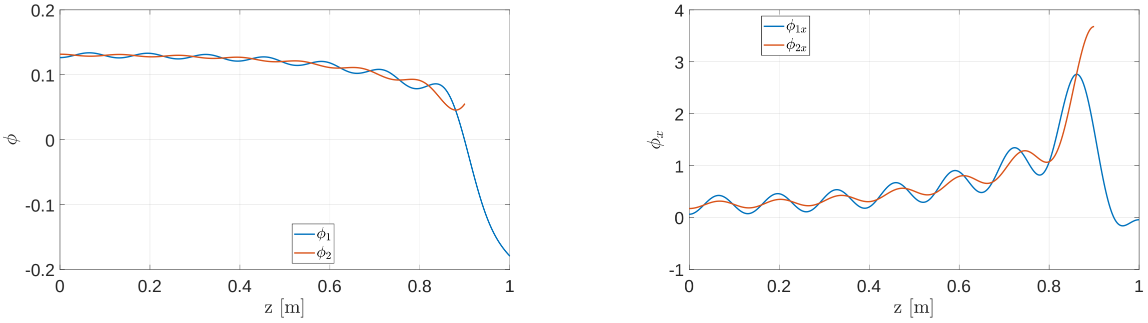

(a) Matching of potentials in x = 0

(b) Matching of derivatives in x = 0

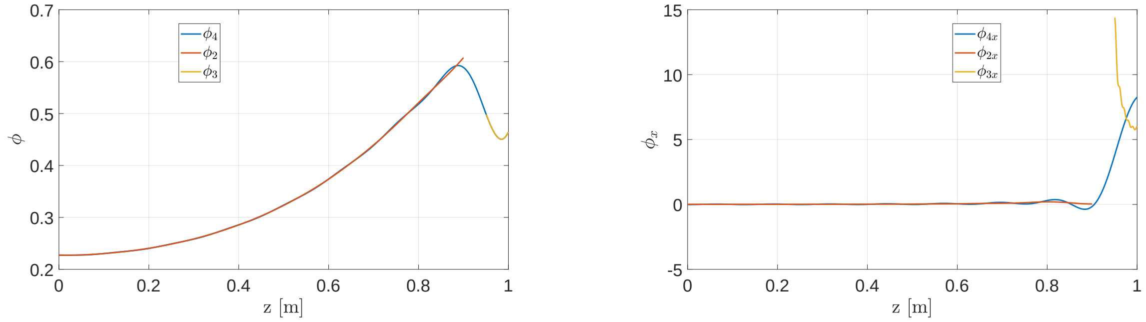

(c) Matching of potentials in x = x_2

(d) Matching of derivatives in x = x_2

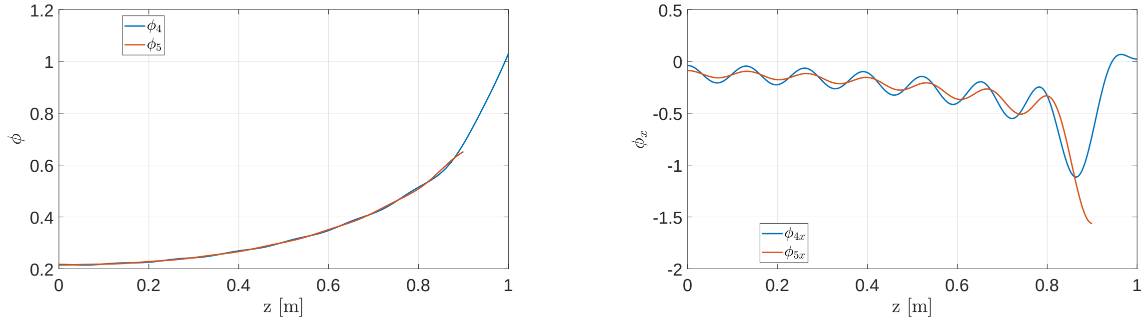

(e) Matching of potentials in x = x_3

(f) Matching of derivatives in x = x_3

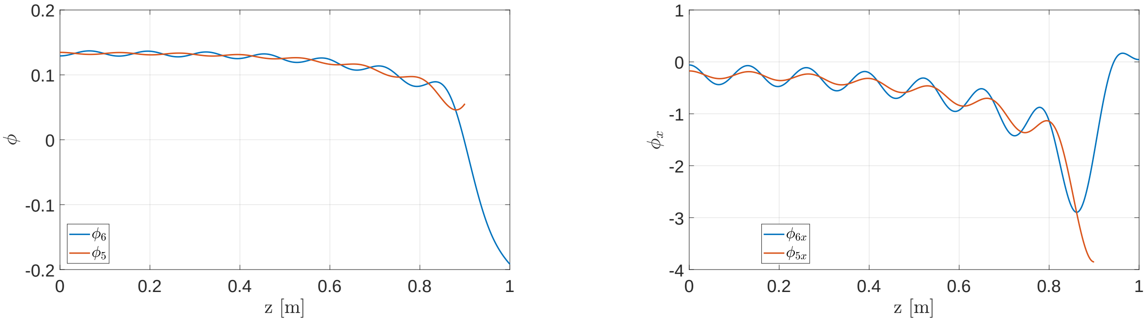

(g) Matching of potentials in x = x_4

(h) Matching of derivatives in x =x_4

Figure B.1: Matching procedures must be validated by checking that the velocity potentials and their derivatives in fact match at all intersections. Some deviations are still visible

Appendix C

Linear Dynamic System

With constant coefficients m, c and k, the general one DOF linear equation of motion for a damped system becomes

$$m\ddot{x} + c\dot{x} + kx = F_0 \cos \omega t \tag{C.1}$$

where m is mass, c is damping, k is stiffness and F_0 is the excitation amplitude. $\ddot{x}, \dot{x}$ and x is acceleration, velocity and displacements respectively.

To solve the differential equation in eq. C.1, Larsen (2012) gives a thorough outline of the procedure. The solution is found as the sum of a particular part and a homogeneous part. The homogeneous solution is established by the damped natural frequency, ω_d. This damped natural frequency is defined as

$$\omega_d = \omega_0 \sqrt{1 - \xi^2} \tag{C.2}$$

where ω_0 is the natural frequency and ξ is the damping ratio defined as

$$\xi = \frac{c}{c_{cr}} = \frac{c}{2\sqrt{mk}} \tag{C.3}$$

where c_{cr} is critical damping.

Because of the form of eq. C.1, it is natural to assume the particular solution to be made of harmonic functions, with frequency equal to the excitation frequency. That is, the particular solution u_t becomes

$$u_p = C_1 \sin \omega t + C_2 \cos \omega t \tag{C.4}$$

The particular solution is then fed into eq. C.1. By differentiating the terms in eq. C.4 to the correct order, one finds the following expression

$$-m\omega^2 C_1 - c\omega C_2 + kC_1 = P_0 - m\omega^2 C_2 - c\omega C_1 + kC_2 = 0 \tag{C.5}$$

By solving the integration constant, solutions for C_1 and C_2 is found as

$$C_1 = \frac{P_0}{k}\frac{1-\beta^2}{(1-\beta^2)+(2\xi\beta)^2} \tag{C.6}$$

$$C_2 = \frac{P_0}{k}\frac{2\zeta\beta}{(1-\beta^2)+(2\xi\beta)^2} \tag{C.7}$$

with β being the frequency ratio, that is the ratio between the excitations frequency ω and the natural frequency ω_0

$$\beta = \frac{\omega}{\omega_0} \tag{C.8}$$

With the constants C_1 and C_2 obtained, the particular solution can be found as

$$u_p = \frac{P_0}{k}\frac{1}{(1-\beta^2)+(2\xi\beta)^2}\left[\left(1-\beta^2\right)\sin\,\omega t - 2\xi\beta\cos\,\omega t\right] \tag{C.9}$$

As t → 0, the homogeneous part will die out, and the response R will be described by the particular solution as

$$R = \sqrt{C_1^2\,+\,C_2^2} = \frac{P_0}{k}\frac{1}{\left[\left(1-\beta^2\right)\left(2\xi\beta\right)^2\right]^{\frac{1}{2}}} \tag{C.10}$$

The dynamic load factor(DLF) is found as

$$DLF = \left|\frac{u_{max}}{u_{st}}\right| = \frac{1}{\left[\left(1-\beta^2\right)\left(2\xi\beta\right)^2\right]^{\frac{1}{2}}} \tag{C.11}$$

Appendix D

Calibration

This section will present the calibration procedures carried out prior to executing the experiments. The main idea is that there exists a linear relation m between measured unit x , and the certain physical output y.

$$y = mx + b \tag{D.1}$$

To obtain the calibration slope for the wave probe rods, voltage is measured at four known depths using a calibration rig fabricated by the lab personnel. The points were then plotted, and a linear regression line constructed. To calibrate the conductive tape that was glued onto the model, the oscillator was used. Hence, a compensation for the displacement effect δ_T cause by the model was needed, as T = T_0 + δ_T where T is the total draft and T_0 is the applied deplacement by the oscillator, and

$$\delta_T = \frac{T_0 \, A_M}{A_T - A_M} \tag{D.2}$$

where A_M is the water line area of the model and A_T is the tank water line area. Figure D.1 shows how this is done for one of the wave probes. In this case the calibration factor is 0.0322, as seen in the calibration curve.

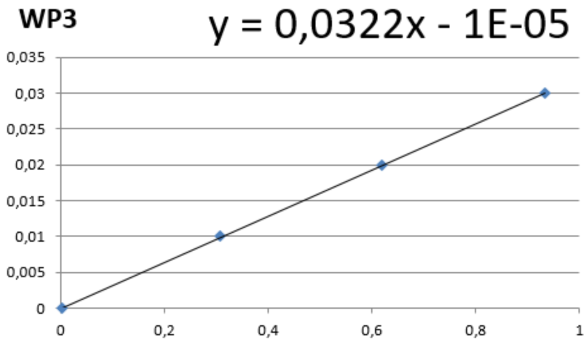

Figure D.1: Construction of calibration curve

Similar calibration procedures were carried out for the accelerometers. Three points were obtained by placing the accelerometer on a piece of cubic wood, and measuring 0G, 1G and 2G at 0, 90° and 180° respectively. The force transducer was calibrated by the lab personnel beforehand, and validated by placing known weights on it. The deplacement measurement system was also validated in advance, by measurement of known lengths. All calibration points were measured for 10-15s, before a mean level was found and plotted.

Appendix E

RAO

RAOs at all longitudinal positions of the moonpool is given in the following. Effect of forcing amplitude are presented, along with the harmonics with forcing amplitude of 0.001m.

RAOs for MP1

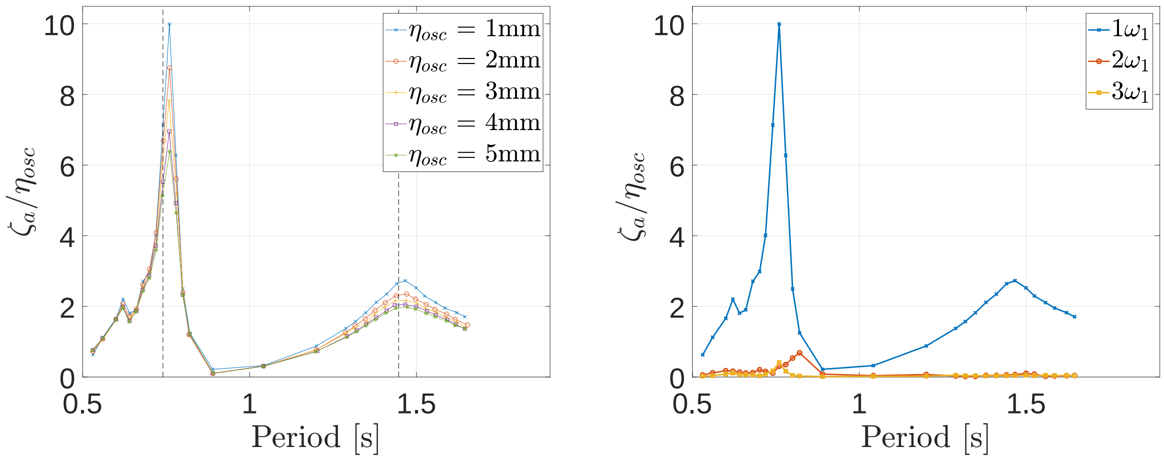

(a) RAO for all forcing amplitudes.

(b) Three first harmonics, with $\eta_{osc} = 0.001$m.

Figure E.1: RAOs at MP1 for $L_R = 0.1$m and draft 0.17m. Dashed lines in (a) show how estimates of natural periods of 1st sloshing mode(left) and piston mode(right) compare

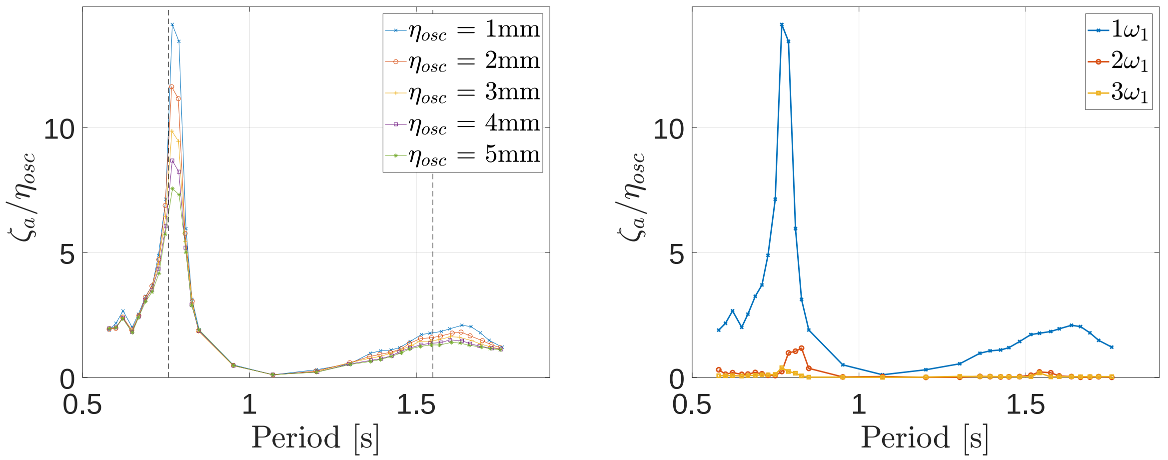

(a) RAO for all forcing amplitudes. (b) Three first harmonics, with η_{osc} = 0.001m.

Figure E.2: RAOs at MP1 for L_R = 0.15m and draft 0.17m. Dashed lines in (a) show how estimates of natural periods of 1st sloshing mode(left) and piston mode(right) compare

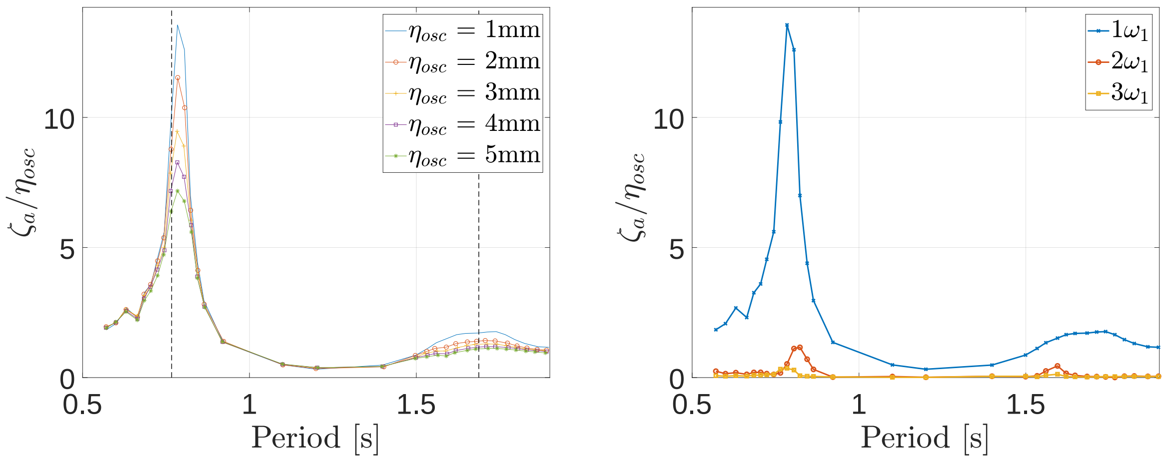

(a) RAO for all forcing amplitudes. (b) Three first harmonics, with η_{osc} = 0.001m.

Figure E.3: RAOs at MP1 for L_R = 0.2m and draft 0.17m. Dashed lines in (a) show how estimates of natural periods of 1st sloshing mode(left) and piston mode(right) compare

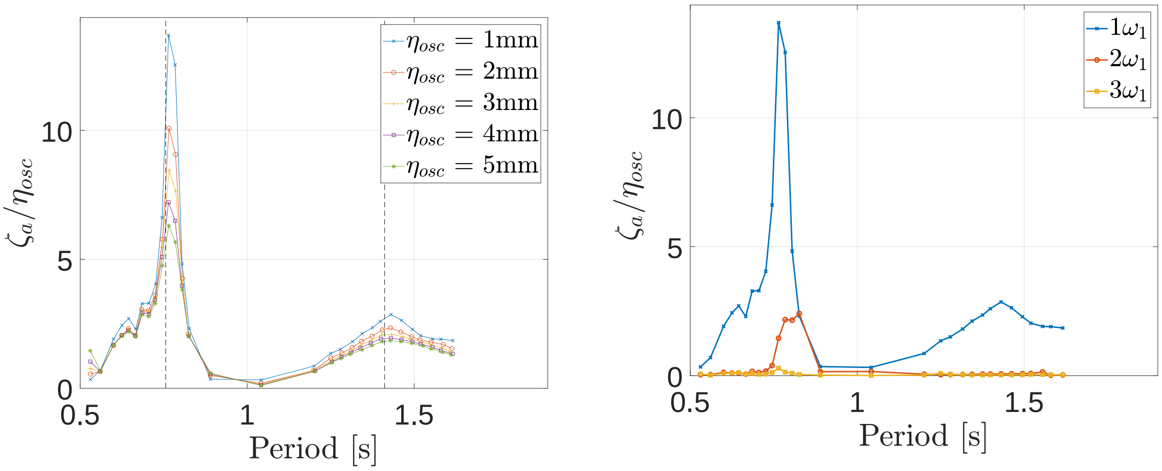

(a) RAO for all forcing amplitudes.

captionThree first harmonics, with η_{osc} = 0.001m.

Figure E.4: RAOs at MP1 for L_R = 0.1m and draft 0.14m. Dashed lines in (a) show how estimates of natural periods of 1st sloshing mode(left) and piston mode(right) compare

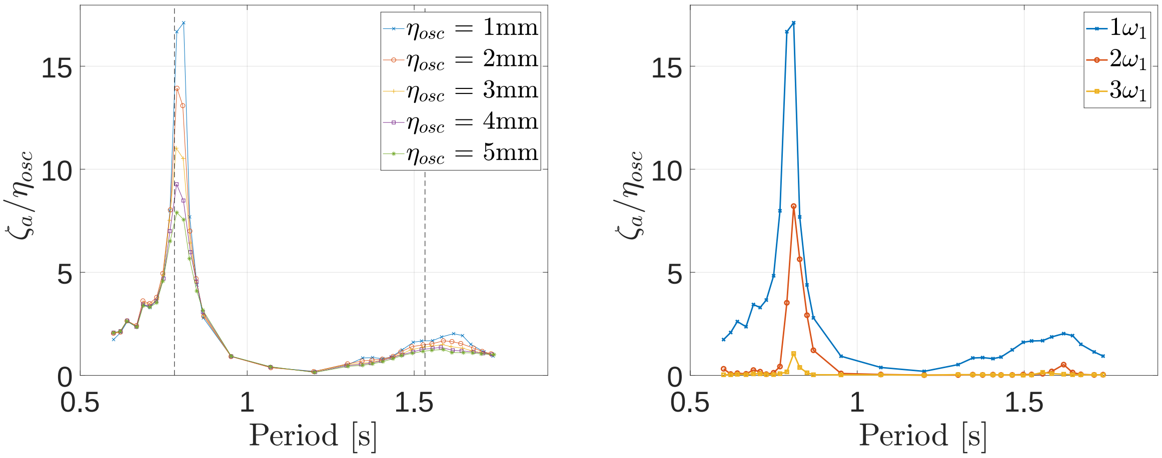

(a) RAO for all forcing amplitudes.

(b) Three first harmonics, with η_{osc} = 0.001m.

Figure E.5: RAOs at MP1 for L_R = 0.15m and draft 0.14m. Dashed lines in (a) show how estimates of natural periods of 1st sloshing mode(left) and piston mode(right) compare

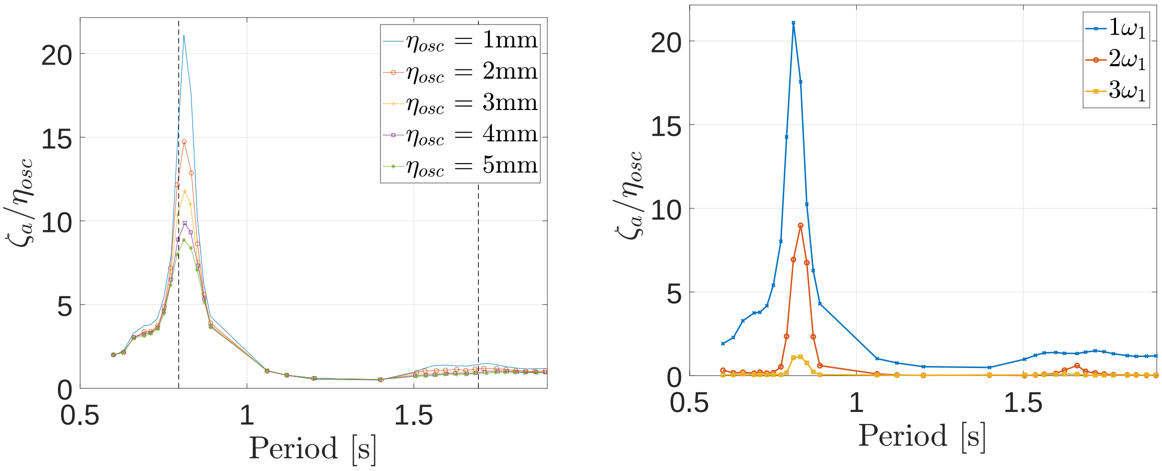

(a) RAO for all forcing amplitudes.

captionThree first harmonics, with η_{osc} = 0.001m.

Figure E.6: RAOs at MP1 for L_R = 0.2m and draft 0.14m. Dashed lines in (a) show how estimates of natural periods of 1st sloshing mode(left) and piston mode(right) compare

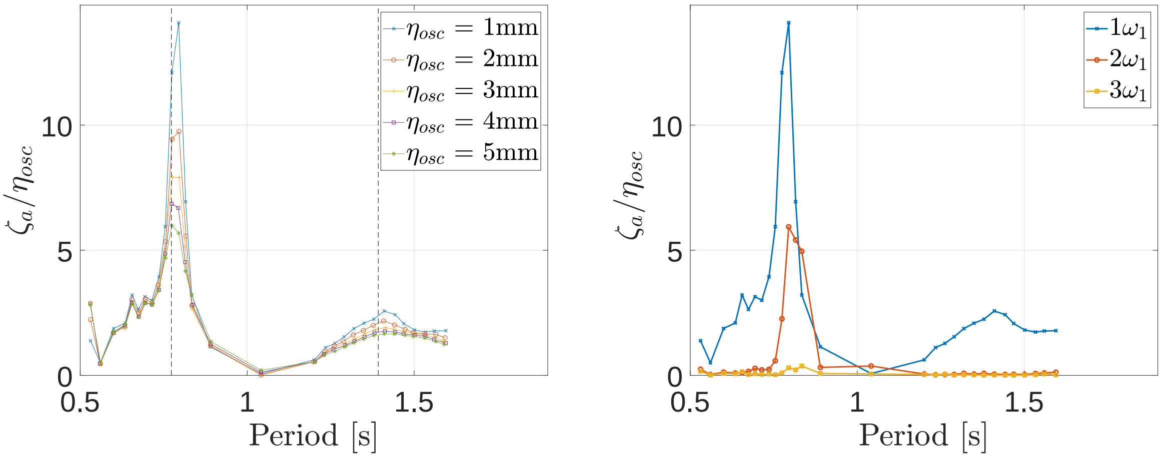

(a) RAO for all forcing amplitudes.

(b) Three first harmonics, with η_{osc} = 0.001m.

Figure E.7: RAOs at MP1 for L_R = 0.1m and draft 0.12m. Dashed lines in (a) show how estimates of natural periods of 1st sloshing mode(left) and piston mode(right) compare

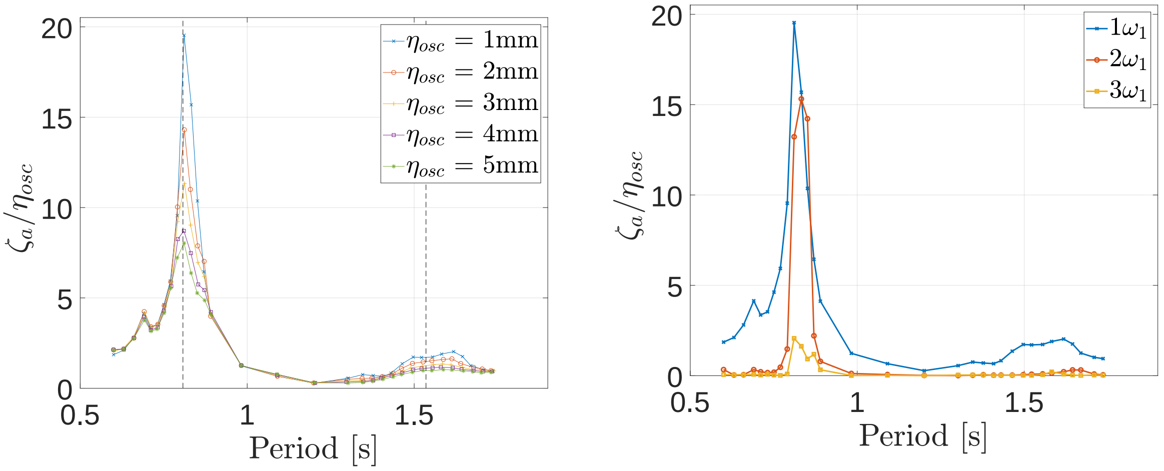

(a) RAO for all forcing amplitudes.

captionThree first harmonics, with η_{osc} = 0.001m.

Figure E.8: RAOs at MP1 for L_R = 0.15m and draft 0.12m. Dashed lines in (a) show how estimates of natural periods of 1st sloshing mode(left) and piston mode(right) compare

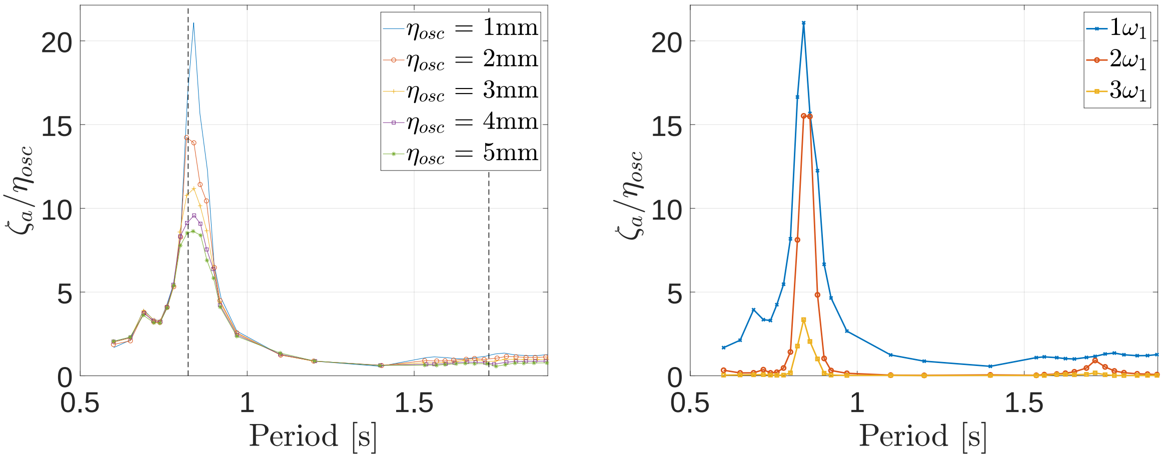

(a) RAO for all forcing amplitudes.

(b) Three first harmonics, with η_{osc} = 0.001m.

Figure E.9: RAOs at MP1 for L_R = 0.2m and draft 0.12m. Dashed lines in (a) show how estimates of natural periods of 1st sloshing mode(left) and piston mode(right) compare

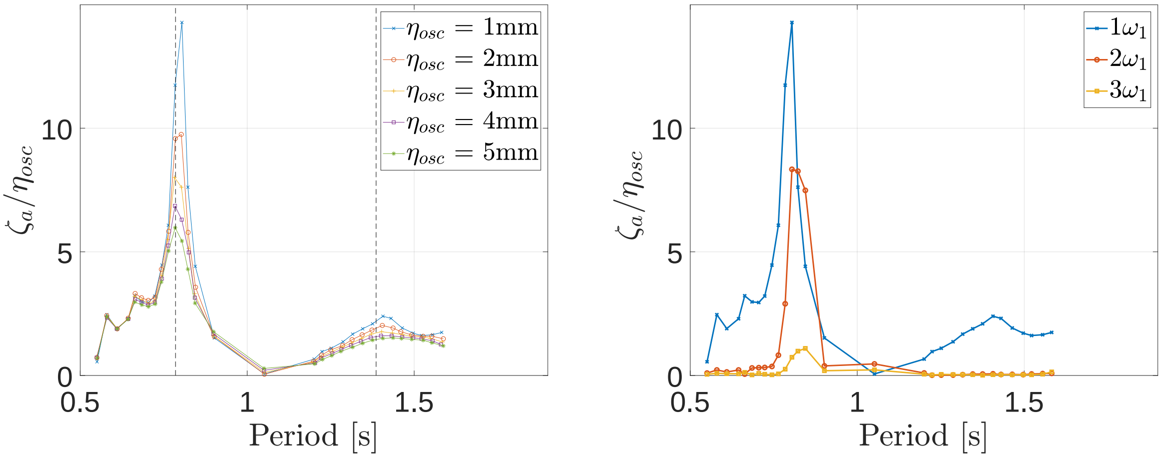

(a) RAO for all forcing amplitudes.

(b) Three first harmonics, with $\eta_{osc} = 0.001$m.

Figure E.10: RAOs at MP1 for $L_R = 0.1$m and draft 0.11m. Dashed lines in (a) show how estimates of natural periods of 1st sloshing mode(left) and piston mode(right) compare

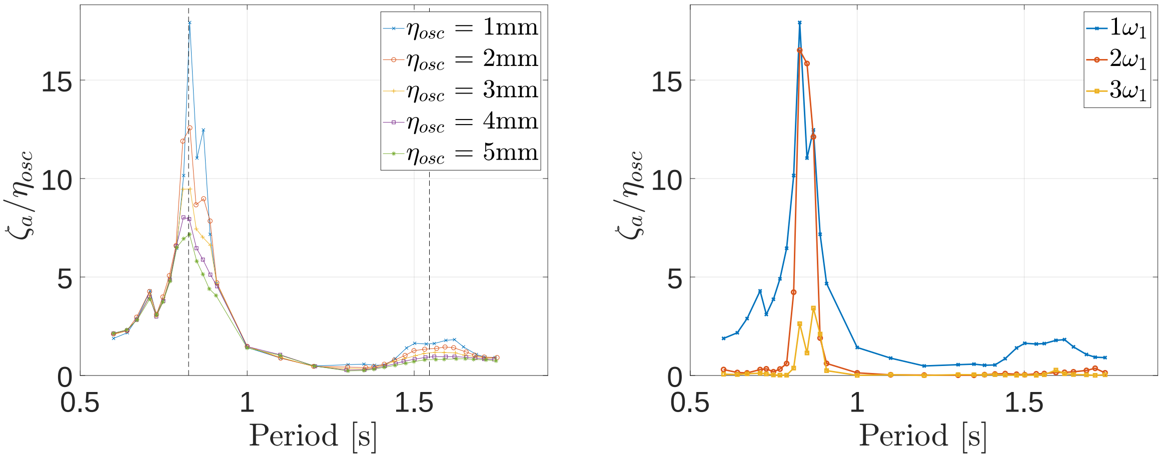

(a) RAO for all forcing amplitudes.

(b) Three first harmonics, with $\eta_{osc} = 0.001$m.

Figure E.11: RAOs at MP1 for $L_R = 0.15$m and draft 0.11m. Dashed lines in (a) show how estimates of natural periods of 1st sloshing mode(left) and piston mode(right) compare

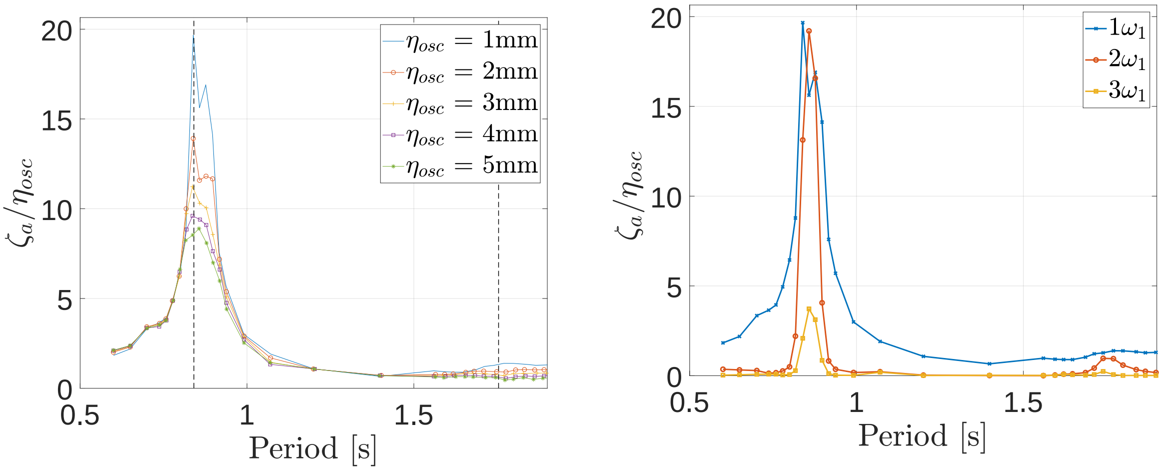

(a) RAO for all forcing amplitudes.

captionThree first harmonics, with η_{osc} = 0.001m.

Figure E.12: RAOs at MP1 for L_R = 0.2m and draft 0.11m. Dashed lines in (a) show how estimates of natural periods of 1st sloshing mode(left) and piston mode(right) compare

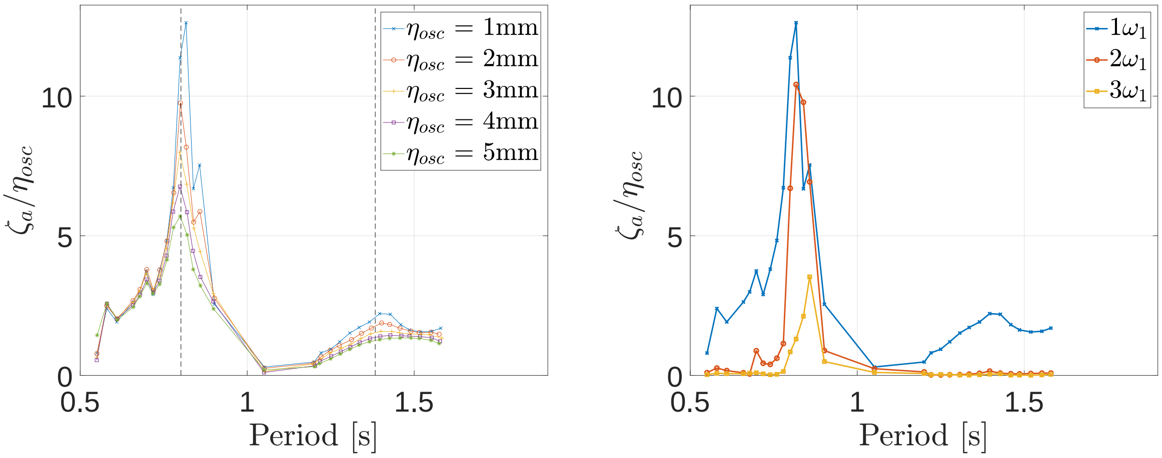

(a) RAO for all forcing amplitudes.

(b) Three first harmonics, with η_{osc} = 0.001m.

Figure E.13: RAOs at MP1 for L_R = 0.1m and draft 0.10m. Dashed lines in (a) show how estimates of natural periods of 1st sloshing mode(left) and piston mode(right) compare

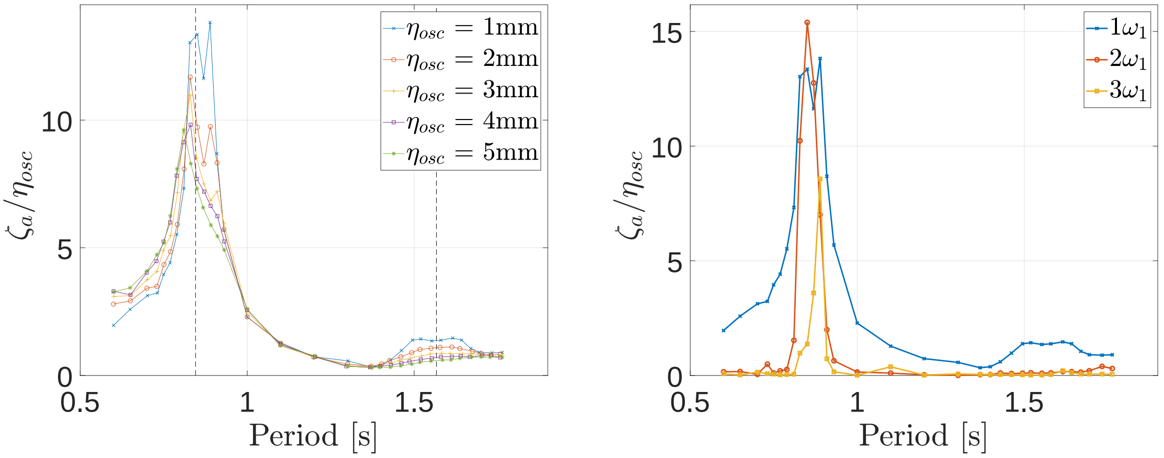

(a) RAO for all forcing amplitudes.

(b) Three first harmonics, with $\eta_{osc} = 0.001$m.

Figure E.14: RAOs at MP1 for $L_R = 0.15$m and draft 0.10m. Dashed lines in (a) show how estimates of natural periods of 1st sloshing mode(left) and piston mode(right) compare

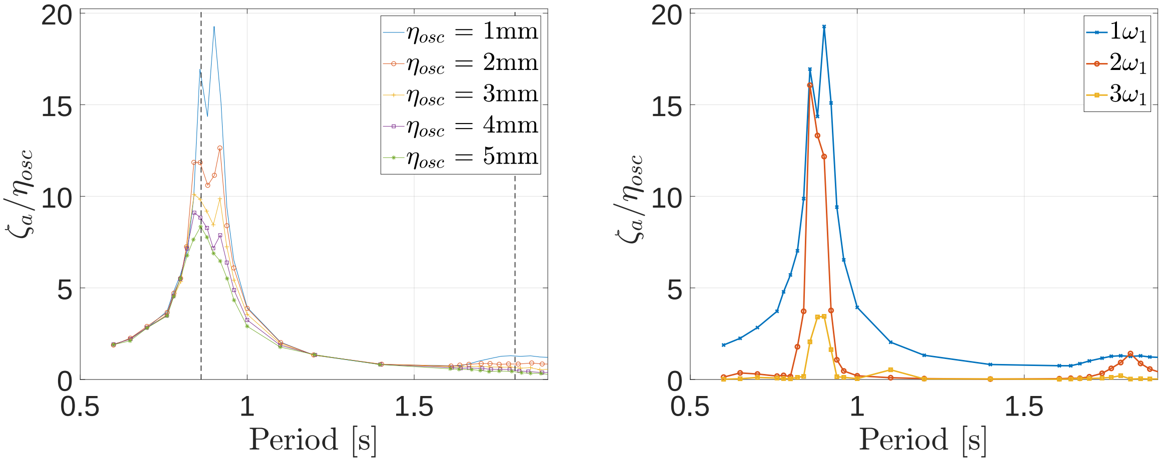

(a) RAO for all forcing amplitudes.

(b) Three first harmonics, with $\eta_{osc} = 0.001$m.

Figure E.15: RAOs at MP1 for $L_R = 0.2$m and draft 0.10m. Dashed lines in (a) show how estimates of natural periods of 1st sloshing mode(left) and piston mode(right) compare

RAOs for MP2

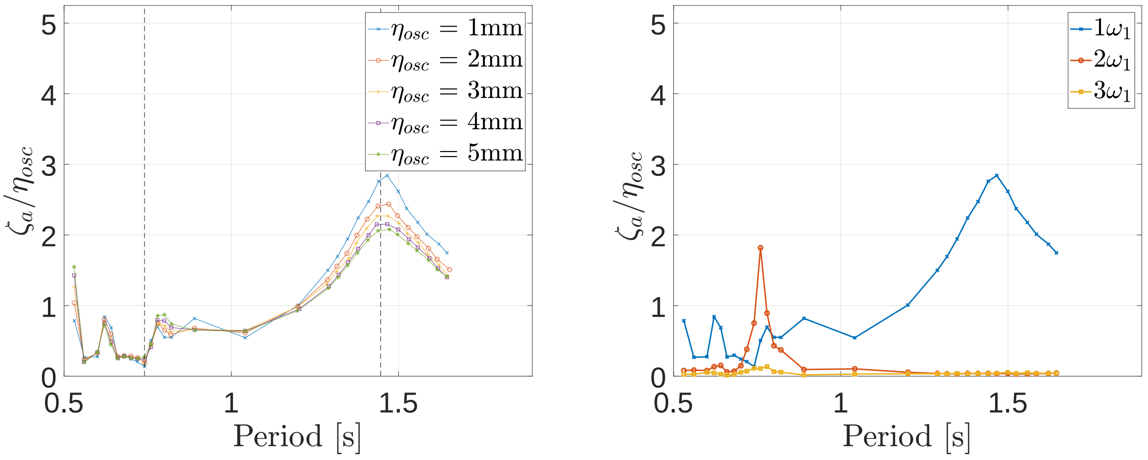

(a) RAO for all forcing amplitudes. (b) Three first harmonics, with $\eta_{osc} = 0.001$m.

Figure E.16: RAOs at MP2 for $L_R = 0.1$m and draft 0.17m. Dashed lines in (a) show how estimates of natural periods of 1st sloshing mode(left) and piston mode(right) compare

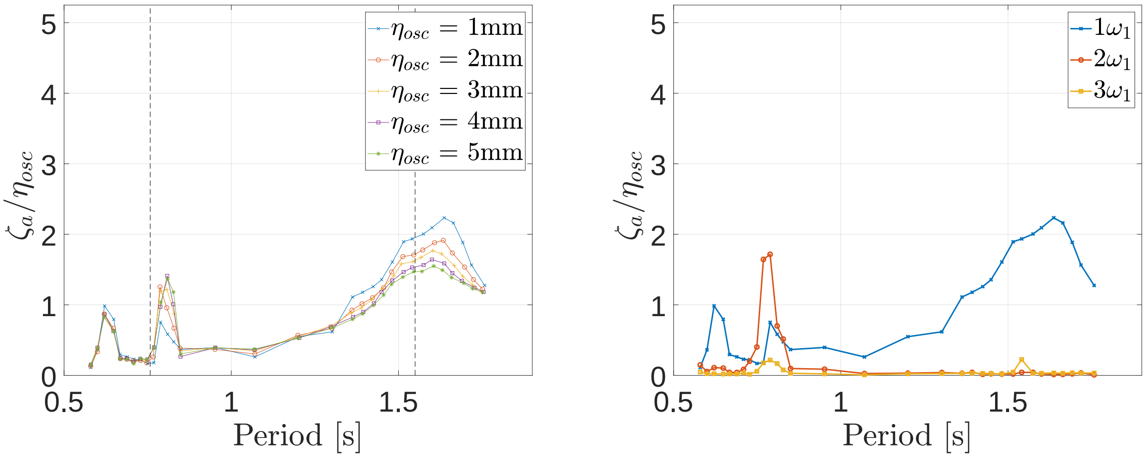

(a) RAO for all forcing amplitudes. (b) Three first harmonics, with $\eta_{osc} = 0.001$m.

Figure E.17: RAOs at MP2 for $L_R = 0.15$m and draft 0.17m. Dashed lines in (a) show how estimates of natural periods of 1st sloshing mode(left) and piston mode(right) compare

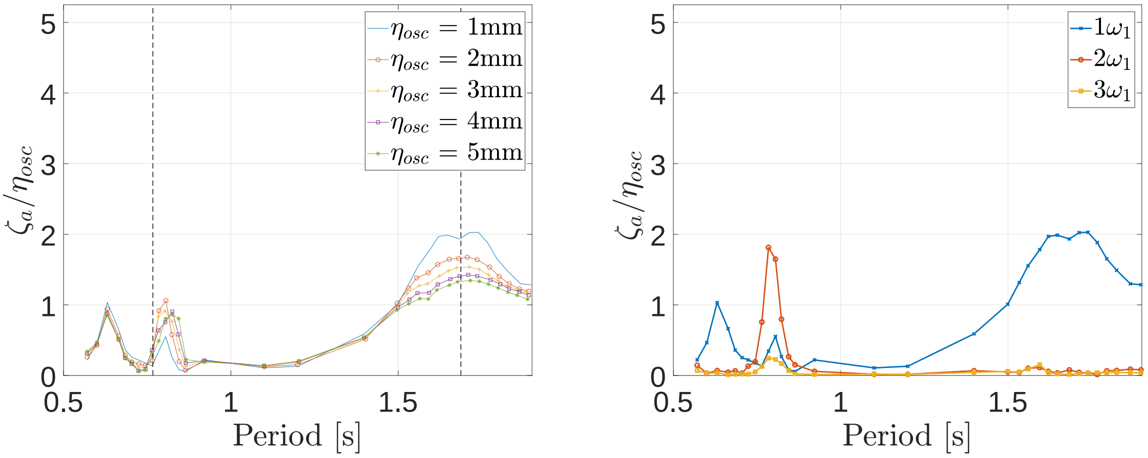

(a) RAO for all forcing amplitudes.

(b) Three first harmonics, with η_{osc} = 0.001m.

Figure E.18: RAOs at MP2 for L_R = 0.2m and draft 0.17m. Dashed lines in (a) show how estimates of natural periods of 1st sloshing mode(left) and piston mode(right) compare

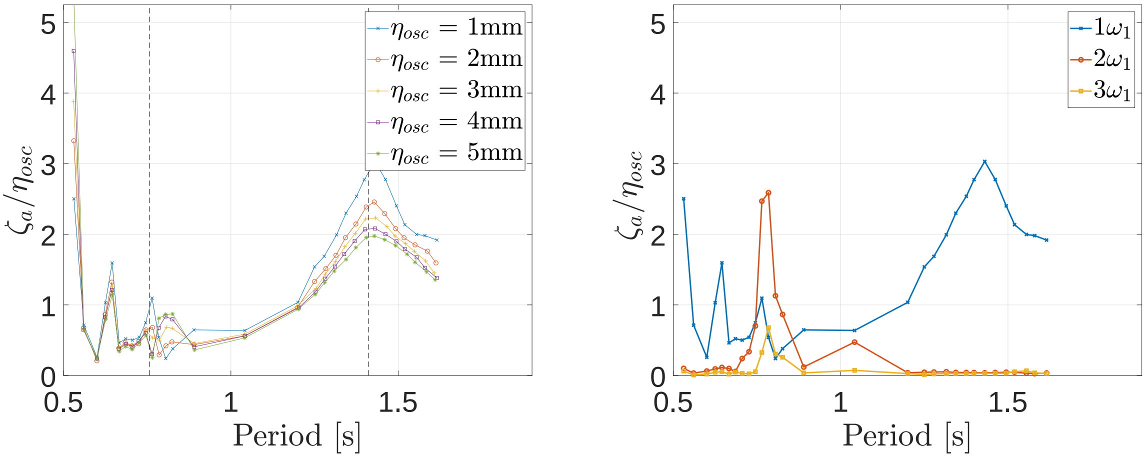

(a) RAO for all forcing amplitudes.

(b) Three first harmonics, with η_{osc} = 0.001m.

Figure E.19: RAOs at MP2 for L_R = 0.1m and draft 0.14m. Dashed lines in (a) show how estimates of natural periods of 1st sloshing mode(left) and piston mode(right) compare

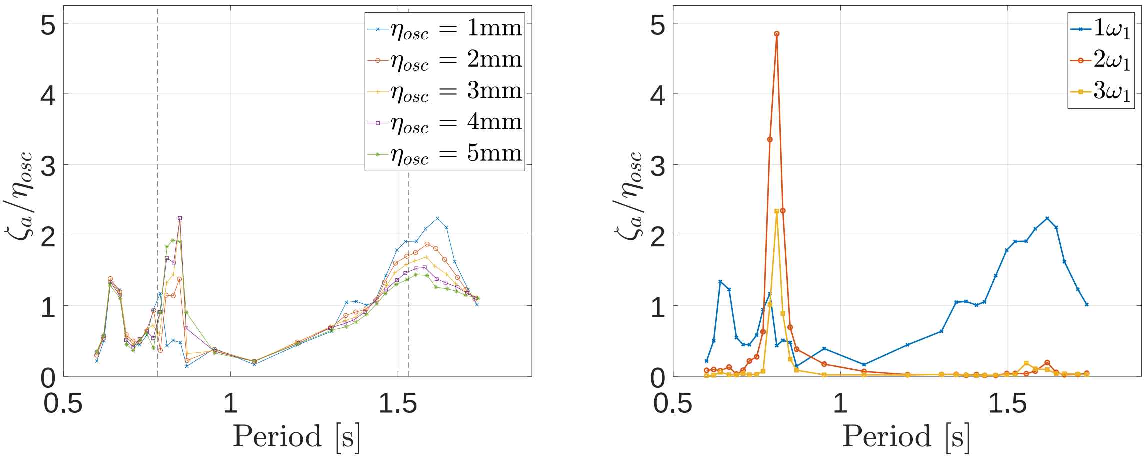

(a) RAO for all forcing amplitudes.

(b) Three first harmonics, with $\eta_{osc} = 0.001$m.

Figure E.20: RAOs at MP2 for $L_R = 0.15$m and draft 0.14m. Dashed lines in (a) show how estimates of natural periods of 1st sloshing mode(left) and piston mode(right) compare

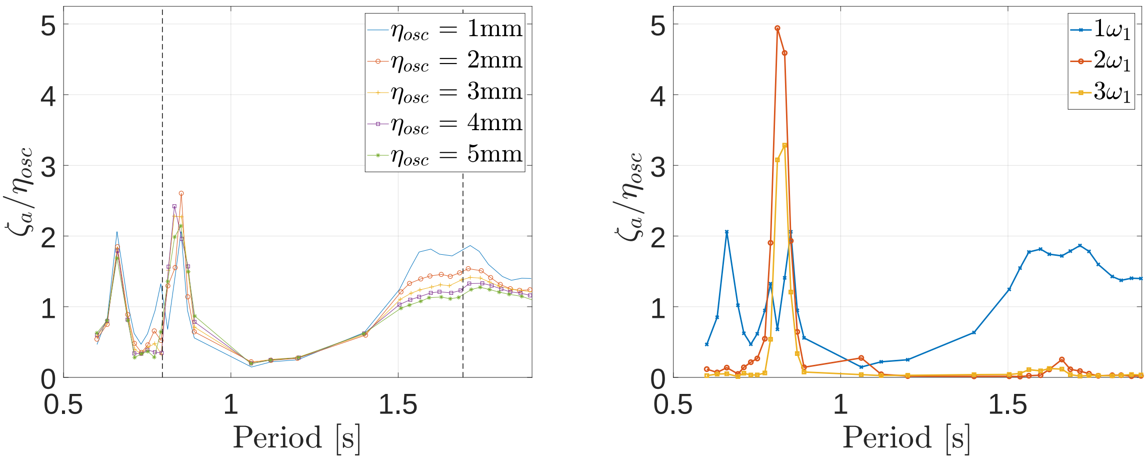

(a) RAO for all forcing amplitudes.

(b) Three first harmonics, with $\eta_{osc} = 0.001$m.

Figure E.21: RAOs at MP2 for $L_R = 0.2$m and draft 0.14m. Dashed lines in (a) show how estimates of natural periods of 1st sloshing mode(left) and piston mode(right) compare

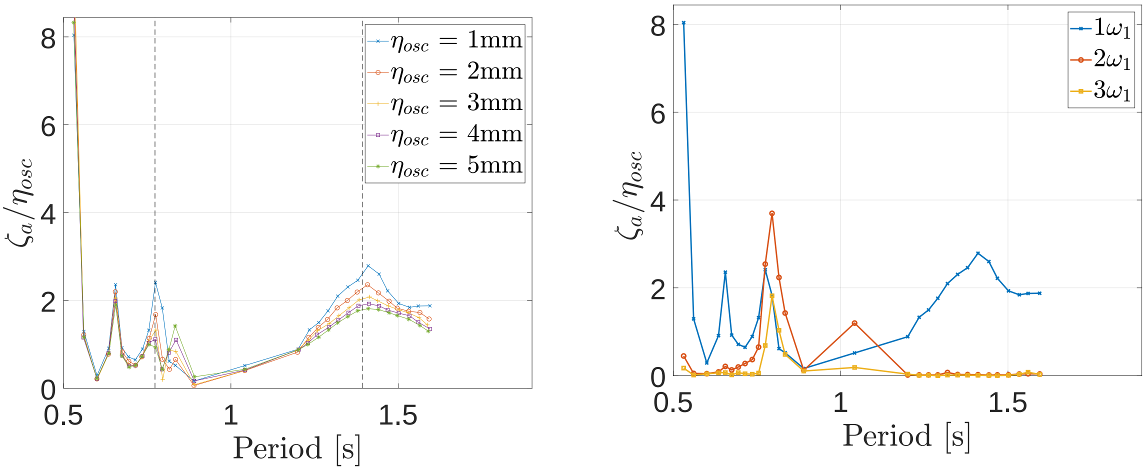

(a) RAO for all forcing amplitudes.

captionThree first harmonics, with η_{osc} = 0.001m.

Figure E.22: RAOs at MP2 for L_R = 0.1m and draft 0.12m. Dashed lines in (a) show how estimates of natural periods of 1st sloshing mode(left) and piston mode(right) compare

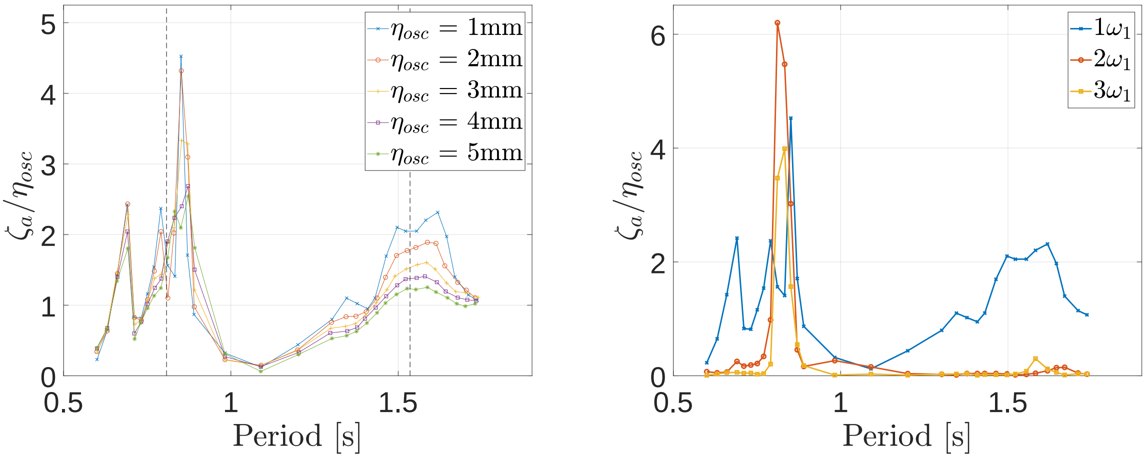

(a) RAO for all forcing amplitudes.

(b) Three first harmonics, with η_{osc} = 0.001m.

Figure E.23: RAOs at MP2 for L_R = 0.15m and draft 0.12m. Dashed lines in (a) show how estimates of natural periods of 1st sloshing mode(left) and piston mode(right) compare

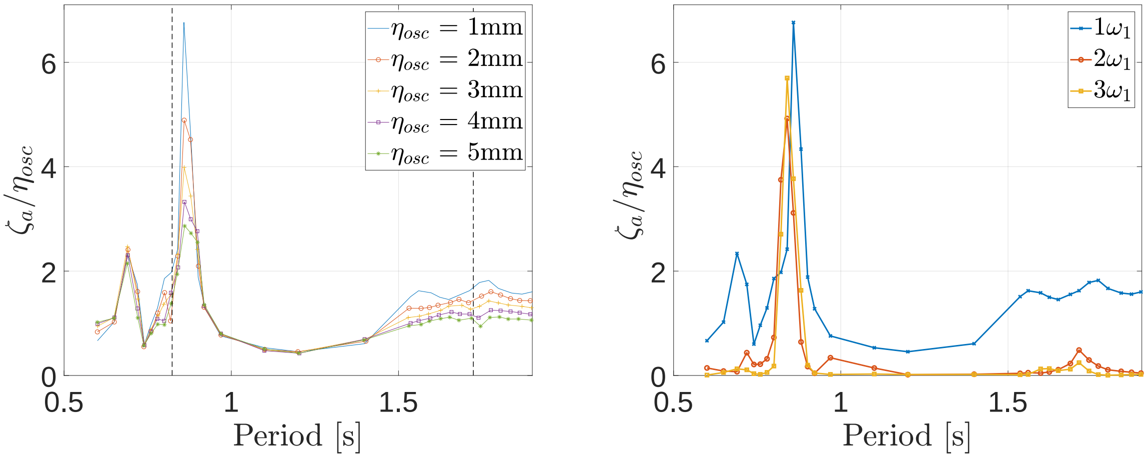

(a) RAO for all forcing amplitudes.

(b) Three first harmonics, with $\eta_{osc} = 0.001$m.

Figure E.24: RAOs at MP2 for $L_R = 0.2$m and draft 0.12m. Dashed lines in (a) show how estimates of natural periods of 1st sloshing mode(left) and piston mode(right) compare

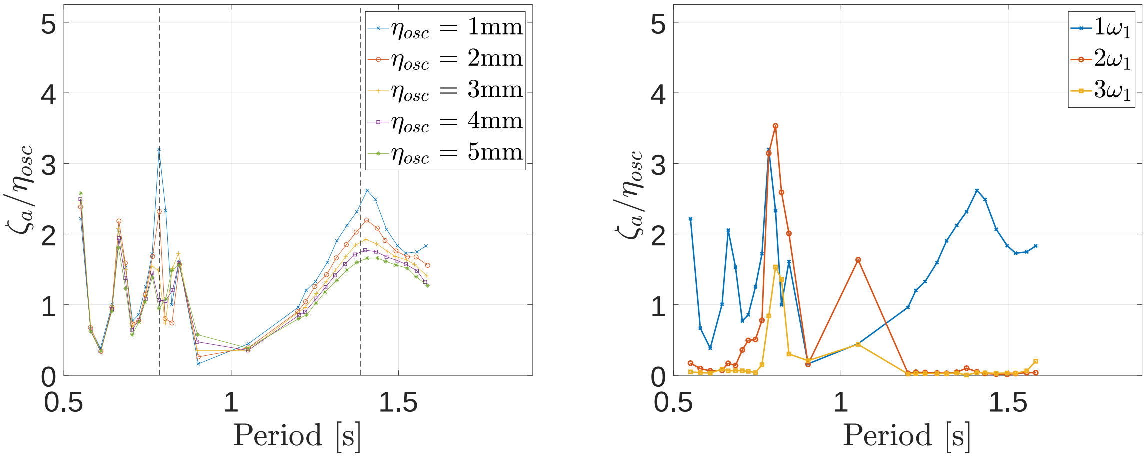

(a) RAO for all forcing amplitudes.

(b) Three first harmonics, with $\eta_{osc} = 0.001$m.

Figure E.25: RAOs at MP2 for $L_R = 0.1$m and draft 0.11m. Dashed lines in (a) show how estimates of natural periods of 1st sloshing mode(left) and piston mode(right) compare

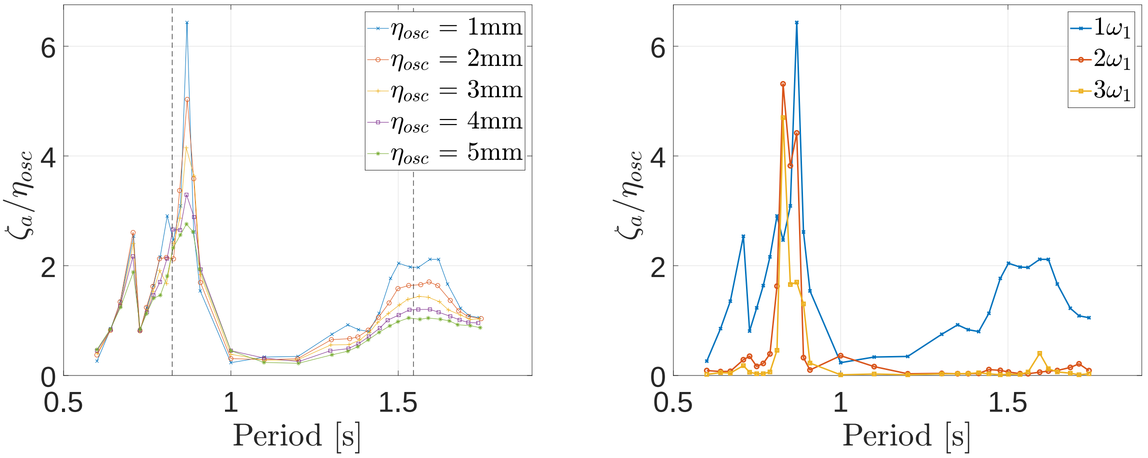

(a) RAO for all forcing amplitudes.

(b) Three first harmonics, with $\eta_{osc} = 0.001$m.

Figure E.26: RAOs at MP2 for L_R = 0.15m and draft 0.11m. Dashed lines in (a) show how estimates of natural periods of 1st sloshing mode(left) and piston mode(right) compare

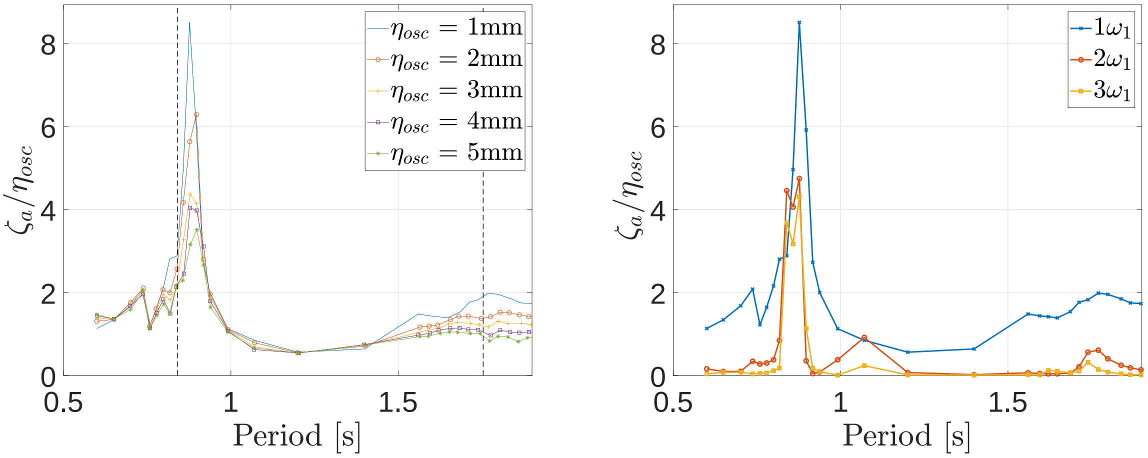

(a) RAO for all forcing amplitudes.

(b) Three first harmonics, with $\eta_{osc} = 0.001$m.

Figure E.27: RAOs at MP2 for L_R = 0.2m and draft 0.11m. Dashed lines in (a) show how estimates of natural periods of 1st sloshing mode(left) and piston mode(right) compare

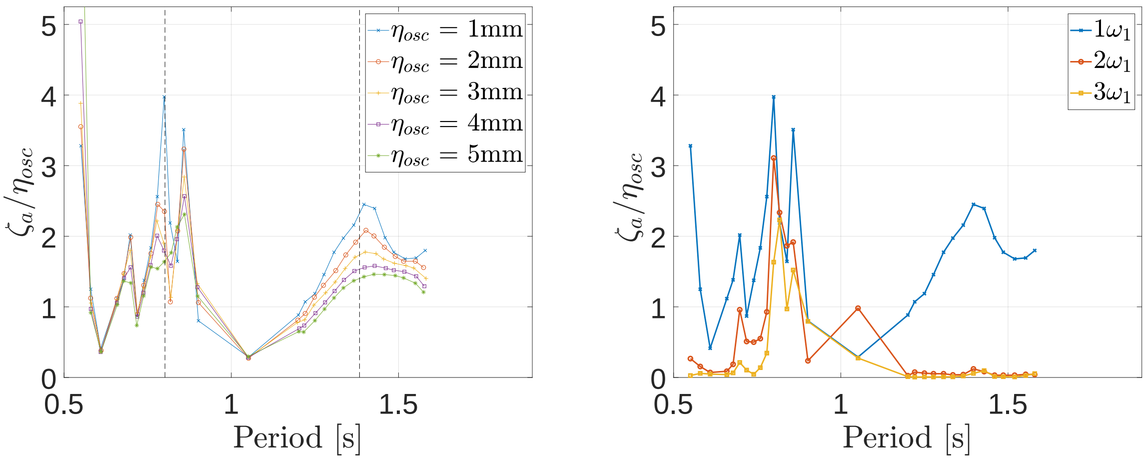

(a) RAO for all forcing amplitudes.

(b) Three first harmonics, with $\eta_{osc} = 0.001$m.

Figure E.28: RAOs at MP2 for $L_R = 0.1$m and draft 0.10m. Dashed lines in (a) show how estimates of natural periods of 1st sloshing mode(left) and piston mode(right) compare

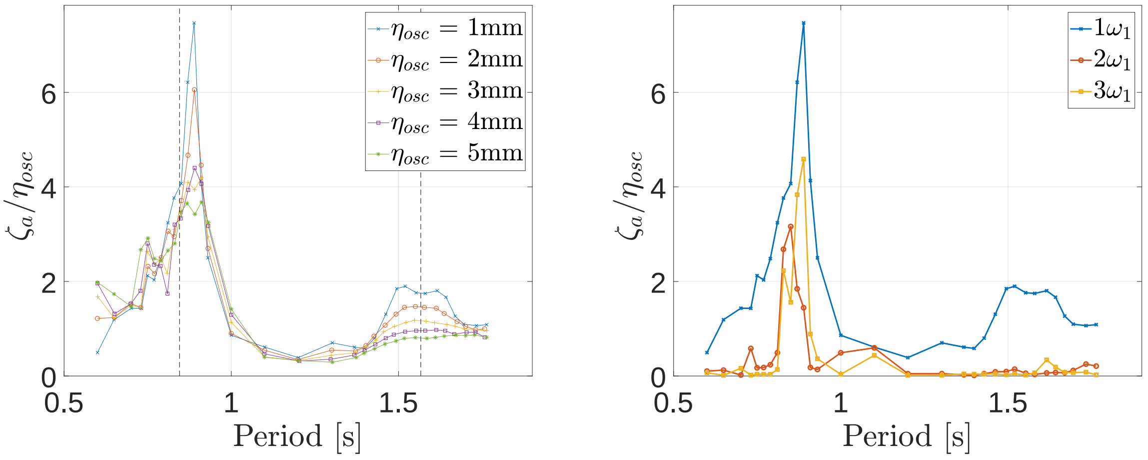

(a) RAO for all forcing amplitudes.

(b) Three first harmonics, with $\eta_{osc} = 0.001$m.

Figure E.29: RAOs at MP2 for $L_R = 0.15$m and draft 0.10m. Dashed lines in (a) show how estimates of natural periods of 1st sloshing mode(left) and piston mode(right) compare

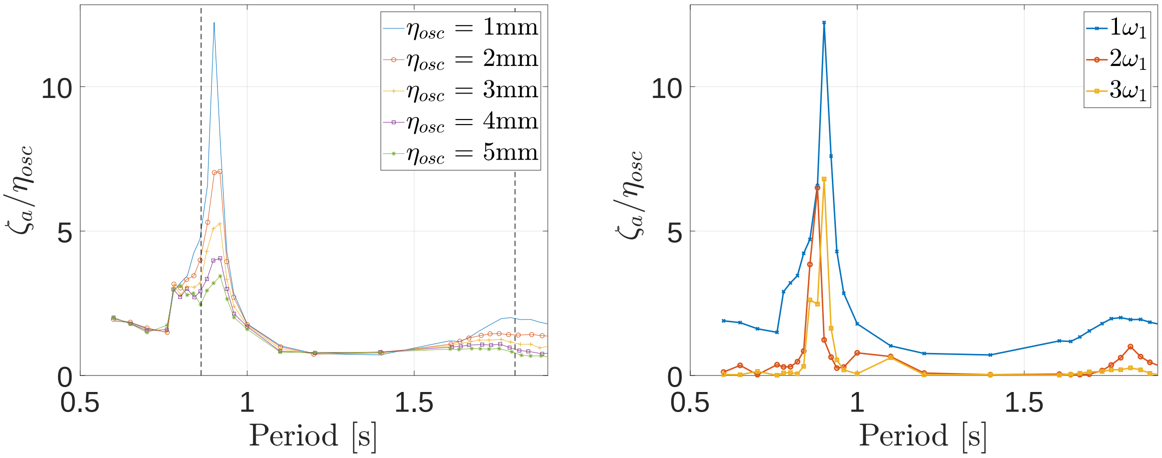

(a) RAO for all forcing amplitudes.

(b) Three first harmonics, with $\eta_{osc} = 0.001$m.

Figure E.30: RAOs at MP2 for $L_R = 0.2$m and draft 0.10m. Dashed lines in (a) show how estimates of natural periods of 1st sloshing mode(left) and piston mode(right) compare

RAOs for MP3

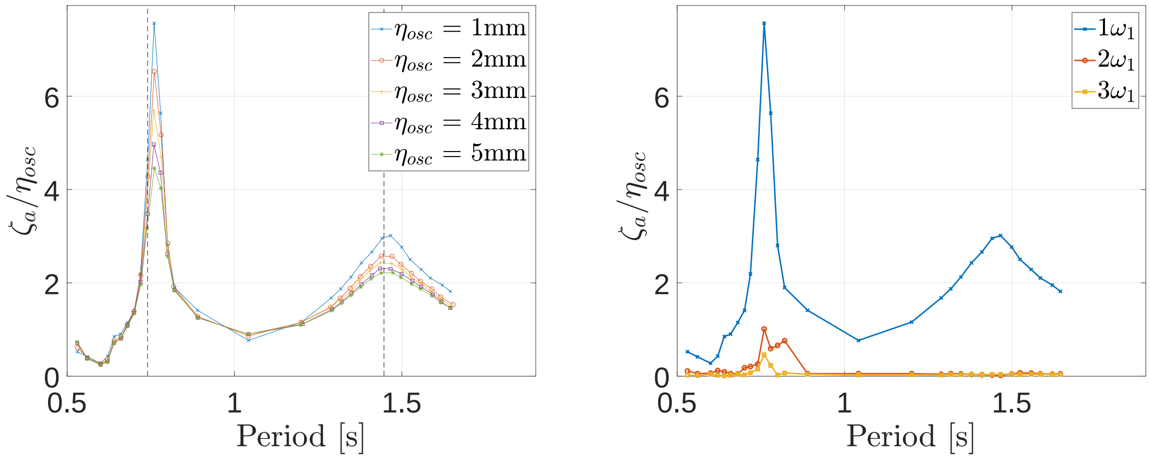

(a) RAO for all forcing amplitudes.

(b) Three first harmonics, with $\eta_{osc} = 0.001$m.

Figure E.31: RAOs at MP3 for $L_R = 0.1$m and draft 0.17m. Dashed lines in (a) show how estimates of natural periods of 1st sloshing mode(left) and piston mode(right) compare

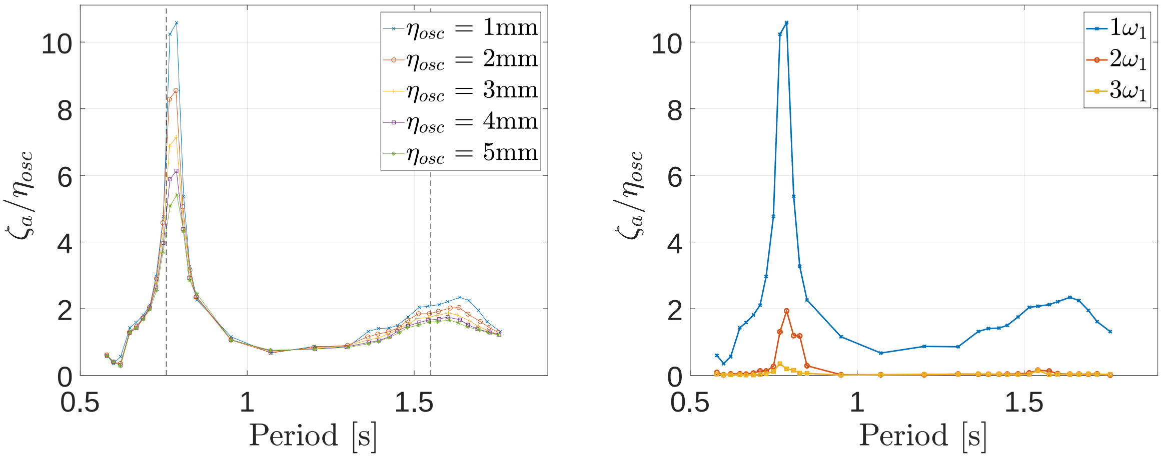

(a) RAO for all forcing amplitudes.

(b) Three first harmonics, with $\eta_{osc} = 0.001$m.

Figure E.32: RAOs at MP3 for $L_R = 0.15$m and draft 0.17m. Dashed lines in (a) show how estimates of natural periods of 1st sloshing mode(left) and piston mode(right) compare

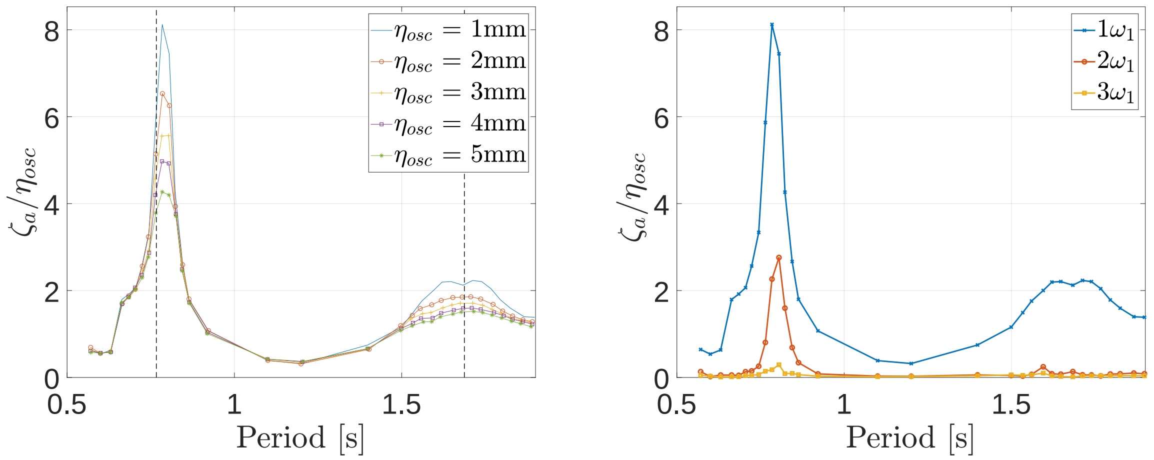

(a) RAO for all forcing amplitudes. (b) Three first harmonics, with η_{osc} = 0.001m.

Figure E.33: RAOs at MP3 for L_R = 0.2m and draft 0.17m. Dashed lines in (a) show how estimates of natural periods of 1st sloshing mode(left) and piston mode(right) compare

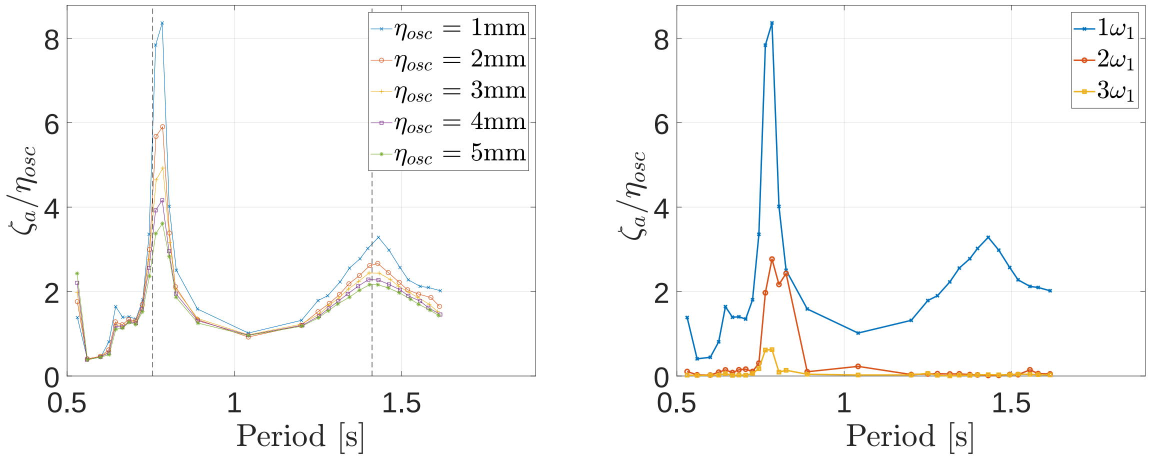

(a) RAO for all forcing amplitudes. (b) Three first harmonics, with η_{osc} = 0.001m.

Figure E.34: RAOs at MP3 for L_R = 0.1m and draft 0.14m. Dashed lines in (a) show how estimates of natural periods of 1st sloshing mode(left) and piston mode(right) compare

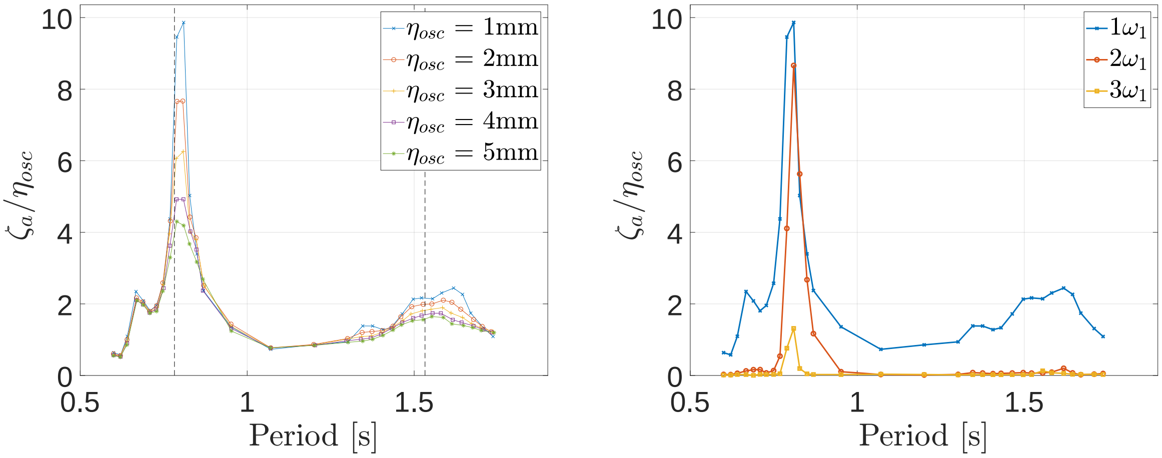

(a) RAO for all forcing amplitudes.

(b) Three first harmonics, with η_{osc} = 0.001m.

Figure E.35: RAOs at MP3 for L_R = 0.15m and draft 0.14m. Dashed lines in (a) show how estimates of natural periods of 1st sloshing mode(left) and piston mode(right) compare

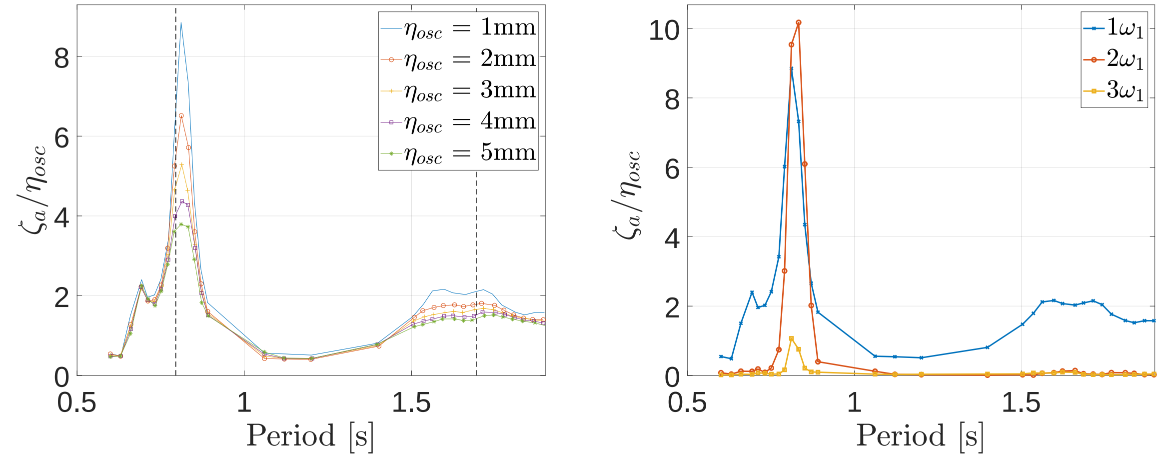

(a) RAO for all forcing amplitudes.

(b) Three first harmonics, with η_{osc} = 0.001m.

Figure E.36: RAOs at MP3 for L_R = 0.2m and draft 0.14m. Dashed lines in (a) show how estimates of natural periods of 1st sloshing mode(left) and piston mode(right) compare

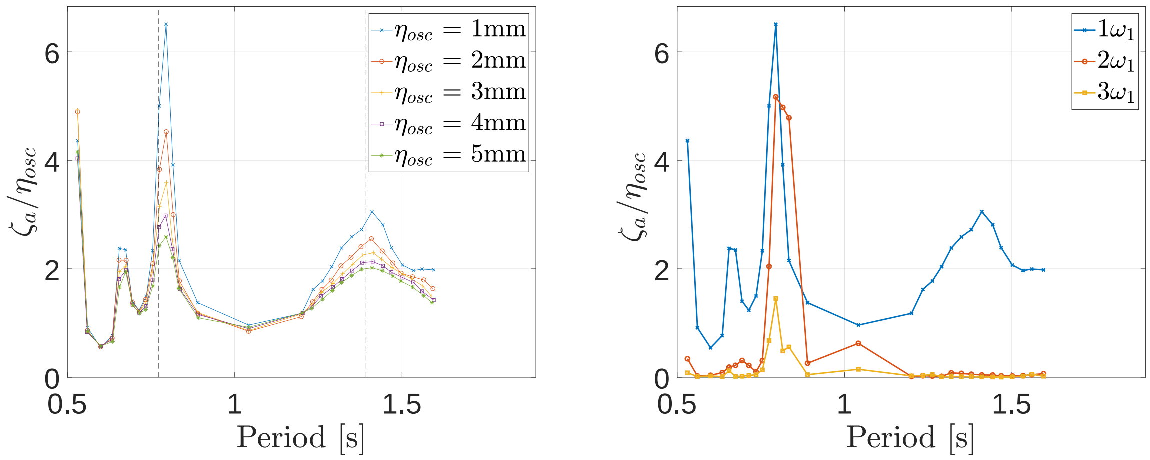

(a) RAO for all forcing amplitudes.

(b) Three first harmonics, with η_{osc} = 0.001m.

Figure E.37: RAOs at MP3 for L_R = 0.1m and draft 0.12m. Dashed lines in (a) show how estimates of natural periods of 1st sloshing mode(left) and piston mode(right) compare

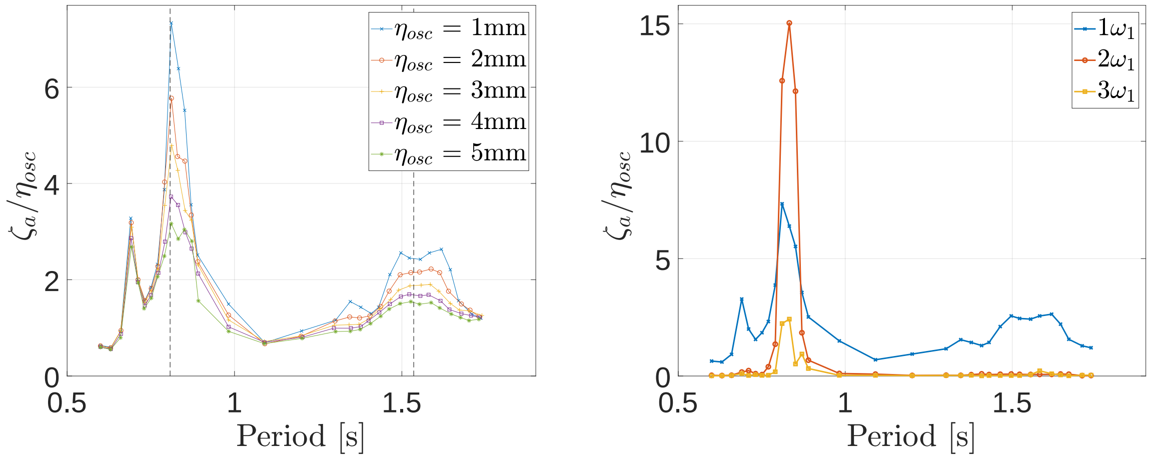

(a) RAO for all forcing amplitudes.

(b) Three first harmonics, with η_{osc} = 0.001m.

Figure E.38: RAOs at MP3 for L_R = 0.15m and draft 0.12m. Dashed lines in (a) show how estimates of natural periods of 1st sloshing mode(left) and piston mode(right) compare

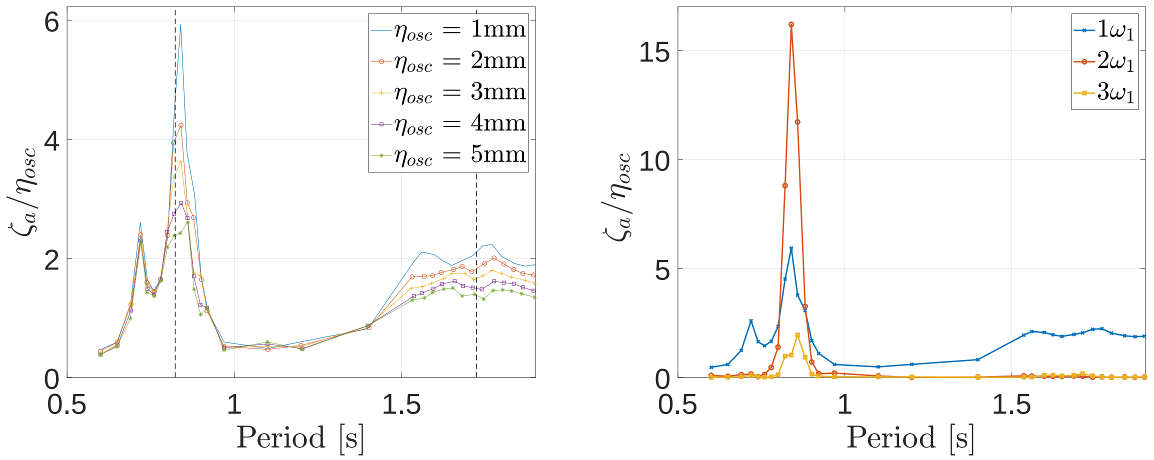

(a) RAO for all forcing amplitudes.

(b) Three first harmonics, with $\eta_{osc} = 0.001$m.

Figure E.39: RAOs at MP3 for $L_R = 0.2$m and draft 0.12m. Dashed lines in (a) show how estimates of natural periods of 1st sloshing mode(left) and piston mode(right) compare

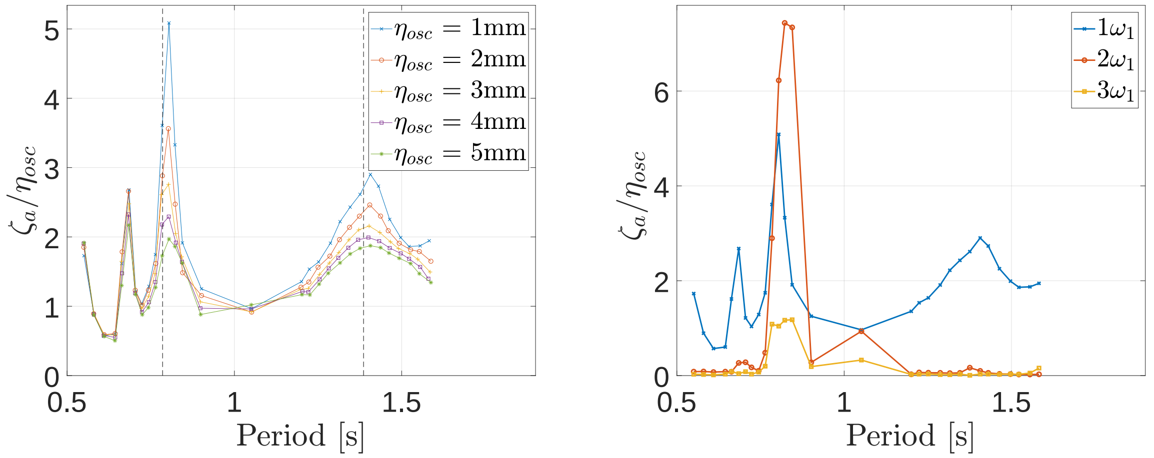

(a) RAO for all forcing amplitudes.

(b) Three first harmonics, with $\eta_{osc} = 0.001$m.

Figure E.40: RAOs at MP3 for $L_R = 0.1$m and draft 0.11m. Dashed lines in (a) show how estimates of natural periods of 1st sloshing mode(left) and piston mode(right) compare

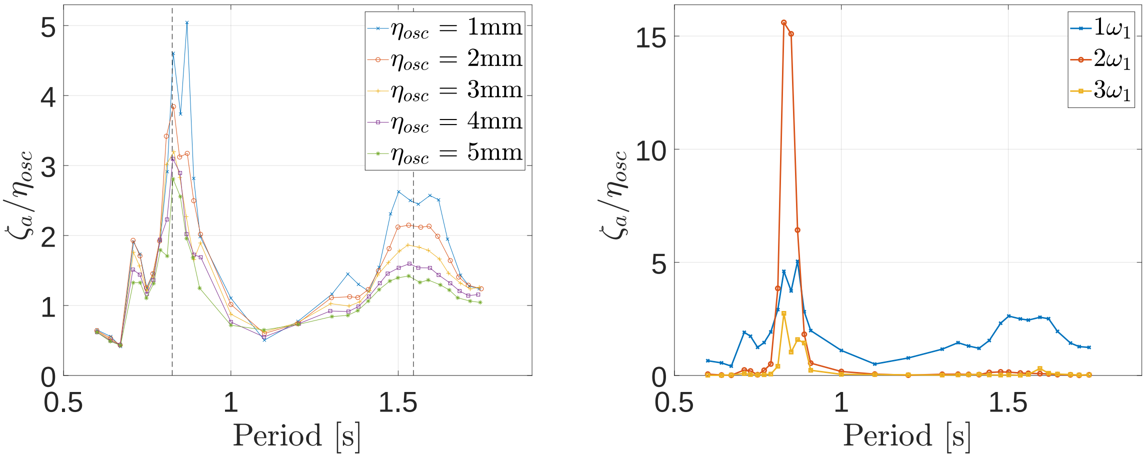

(a) RAO for all forcing amplitudes.

(b) Three first harmonics, with $\eta_{osc} = 0.001$m.

Figure E.41: RAOs at MP3 for $L_R = 0.15$m and draft 0.11m. Dashed lines in (a) show how estimates of natural periods of 1st sloshing mode(left) and piston mode(right) compare

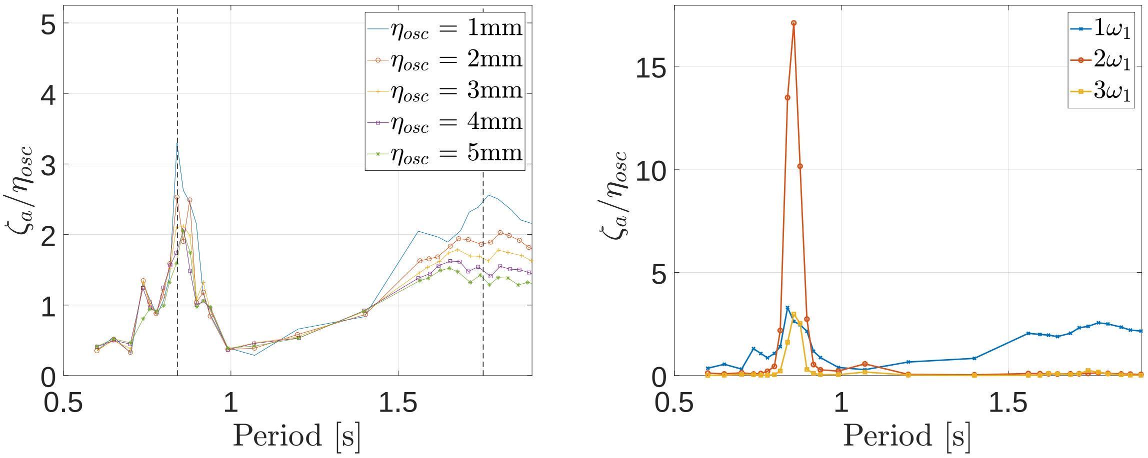

(a) RAO for all forcing amplitudes.

(b) Three first harmonics, with $\eta_{osc} = 0.001$m.

Figure E.42: RAOs at MP3 for $L_R = 0.2$m and draft 0.11m. Dashed lines in (a) show how estimates of natural periods of 1st sloshing mode(left) and piston mode(right) compare

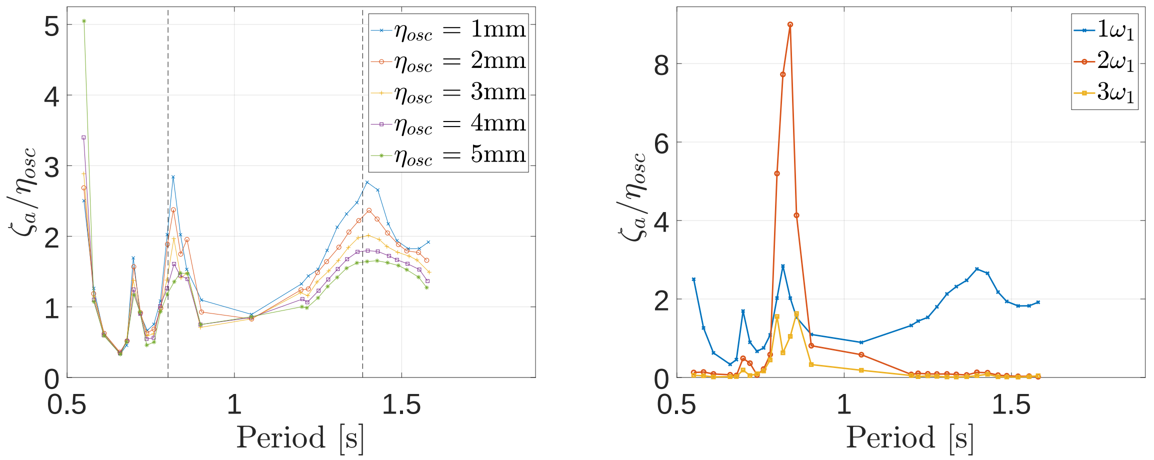

(a) RAO for all forcing amplitudes.

(b) Three first harmonics, with η_{osc} = 0.001m.

Figure E.43: RAOs at MP3 for L_R = 0.1m and draft 0.10m. Dashed lines in (a) show how estimates of natural periods of 1st sloshing mode(left) and piston mode(right) compare

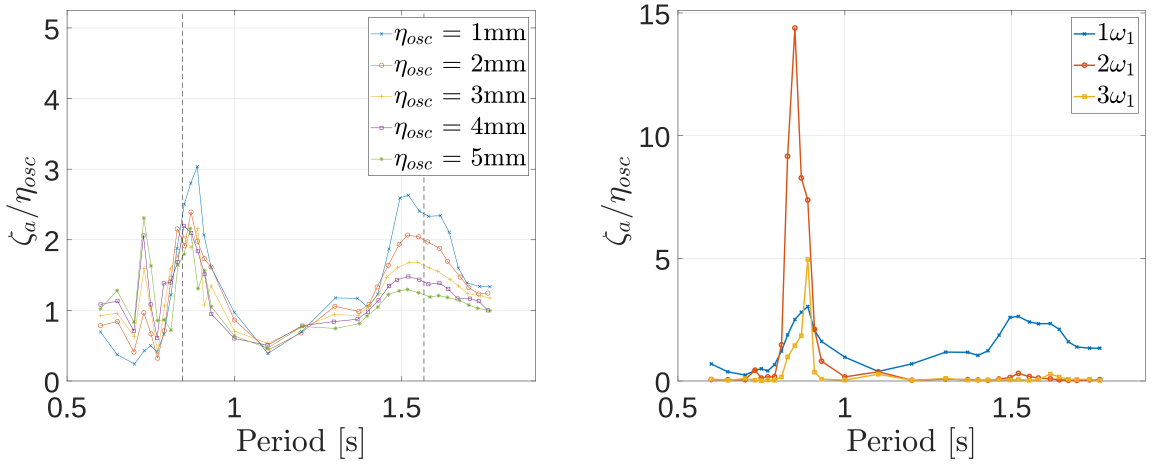

(a) RAO for all forcing amplitudes.

(b) Three first harmonics, with η_{osc} = 0.001m.

Figure E.44: RAOs at MP3 for L_R = 0.15m and draft 0.10m. Dashed lines in (a) show how estimates of natural periods of 1st sloshing mode(left) and piston mode(right) compare

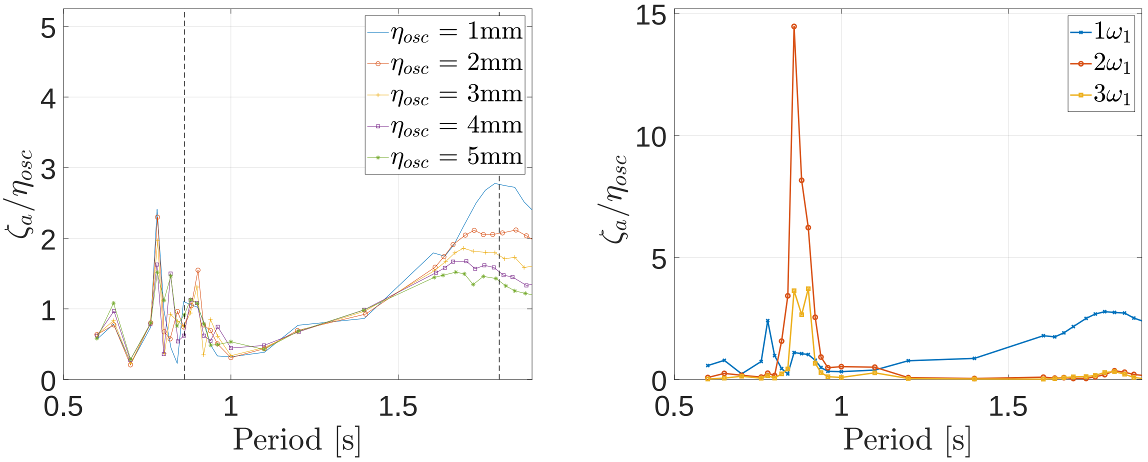

(a) RAO for all forcing amplitudes.

(b) Three first harmonics, with $\eta_{osc} = 0.001$m.

Figure E.45: RAOs at MP3 for $L_R = 0.2$m and draft 0.10m. Dashed lines in (a) show how estimates of natural periods of 1st sloshing mode(left) and piston mode(right) compare

RAOs for MP4

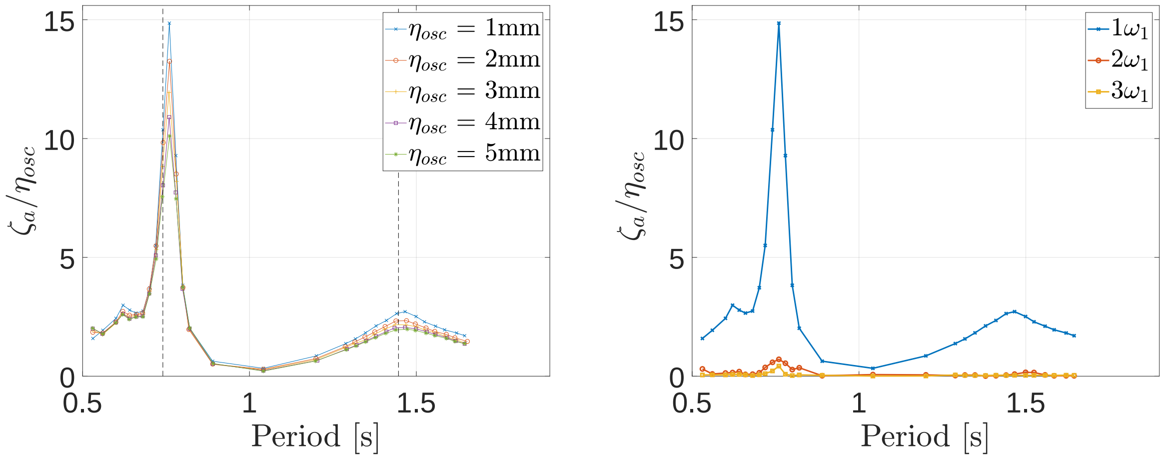

(a) RAO for all forcing amplitudes.

(b) Three first harmonics, with $\eta_{osc} = 0.001$m.

Figure E.46: RAOs at MP4 for $L_R = 0.1$m and draft 0.17m. Dashed lines in (a) show how estimates of natural periods of 1st sloshing mode(left) and piston mode(right) compare

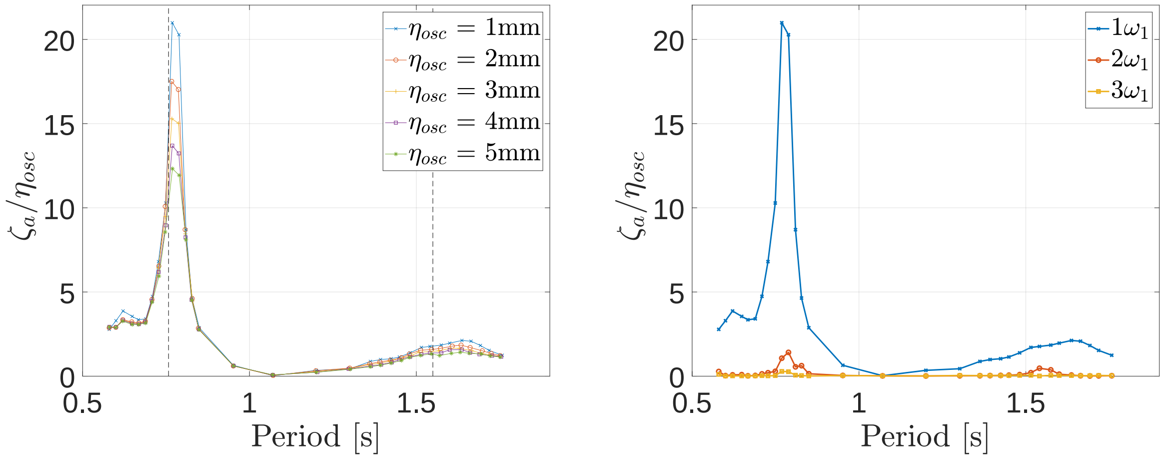

(a) RAO for all forcing amplitudes.

(b) Three first harmonics, with $\eta_{osc} = 0.001$m.

Figure E.47: RAOs at MP4 for $L_R = 0.15$m and draft 0.17m. Dashed lines in (a) show how estimates of natural periods of 1st sloshing mode(left) and piston mode(right) compare

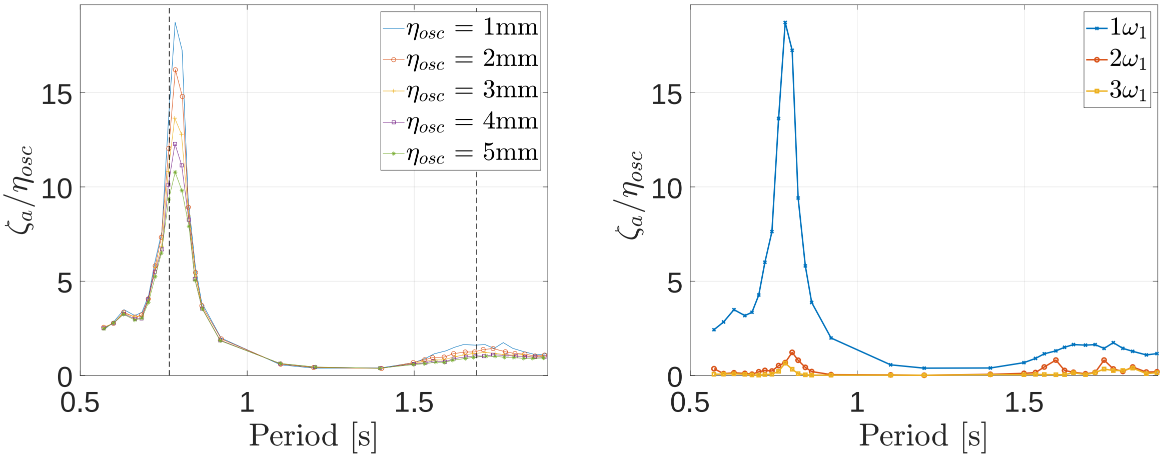

(a) RAO for all forcing amplitudes.

(b) Three first harmonics, with $\eta_{osc} = 0.001$m.

Figure E.48: RAOs at MP4 for $L_R = 0.2$m and draft 0.17m. Dashed lines in (a) show how estimates of natural periods of 1st sloshing mode(left) and piston mode(right) compare

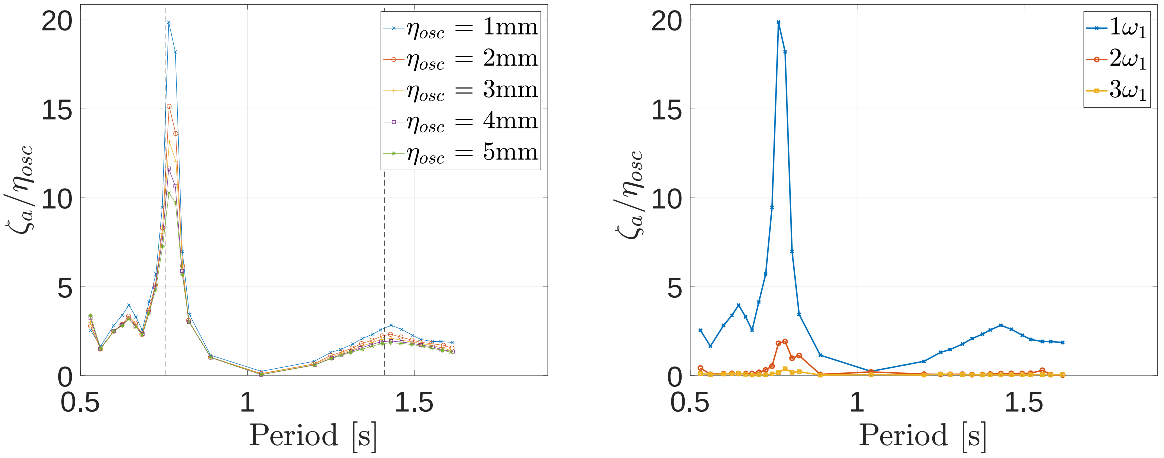

(a) RAO for all forcing amplitudes.

(b) Three first harmonics, with $\eta_{osc} = 0.001$m.

Figure E.49: RAOs at MP4 for $L_R = 0.1$m and draft 0.14m. Dashed lines in (a) show how estimates of natural periods of 1st sloshing mode(left) and piston mode(right) compare

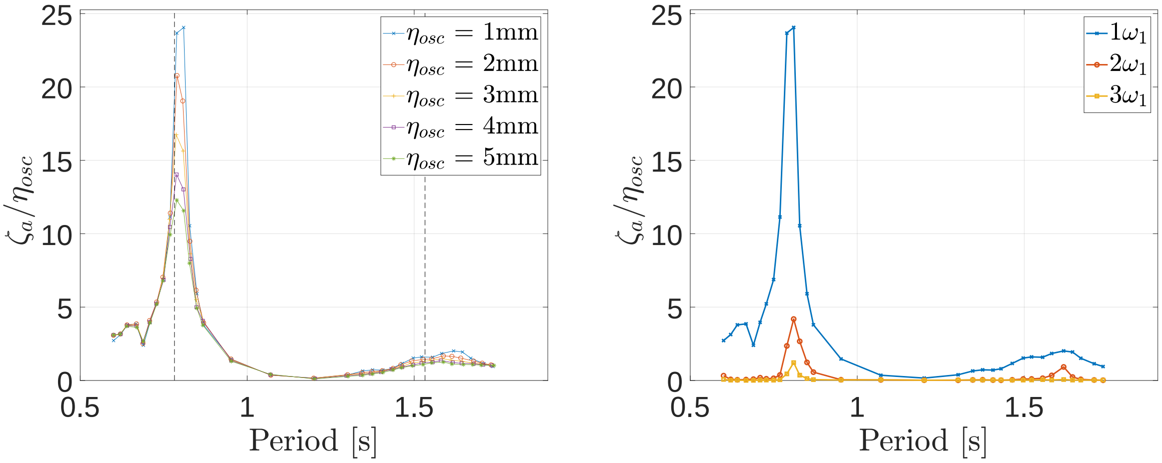

(a) RAO for all forcing amplitudes.

(b) Three first harmonics, with $\eta_{osc} = 0.001$m.

Figure E.50: RAOs at MP4 for $L_R = 0.15$m and draft 0.14m. Dashed lines in (a) show how estimates of natural periods of 1st sloshing mode(left) and piston mode(right) compare

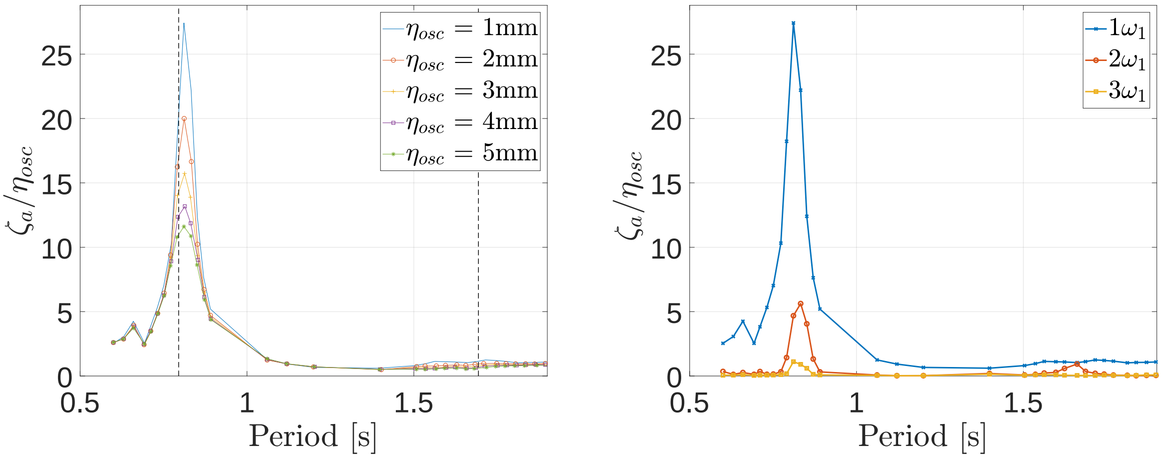

(a) RAO for all forcing amplitudes.

(b) Three first harmonics, with $\eta_{osc} = 0.001$m.

Figure E.51: RAOs at MP4 for $L_R = 0.2$m and draft 0.14m. Dashed lines in (a) show how estimates of natural periods of 1st sloshing mode(left) and piston mode(right) compare

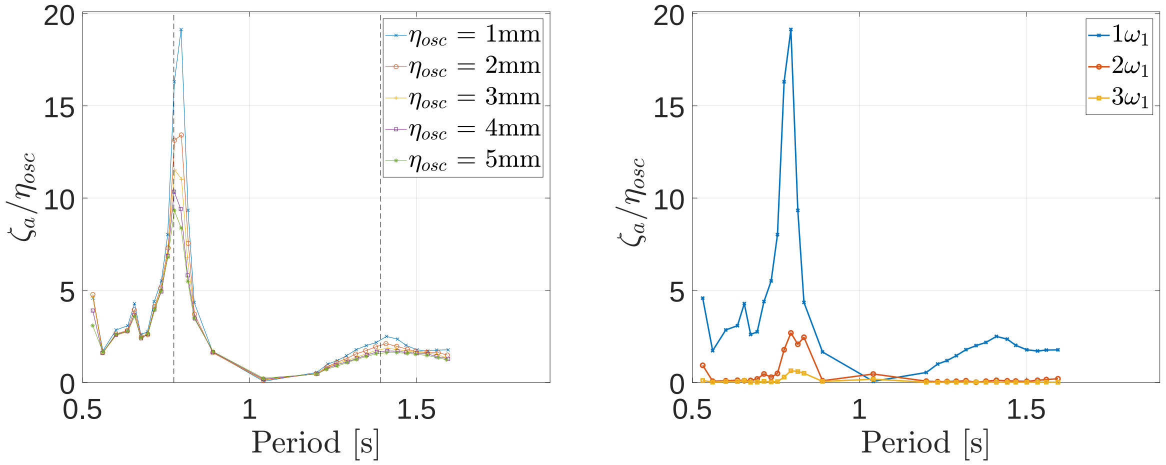

(a) RAO for all forcing amplitudes.

(b) Three first harmonics, with $\eta_{osc} = 0.001$m.

Figure E.52: RAOs at MP4 for $L_R = 0.1$m and draft 0.12m. Dashed lines in (a) show how estimates of natural periods of 1st sloshing mode(left) and piston mode(right) compare

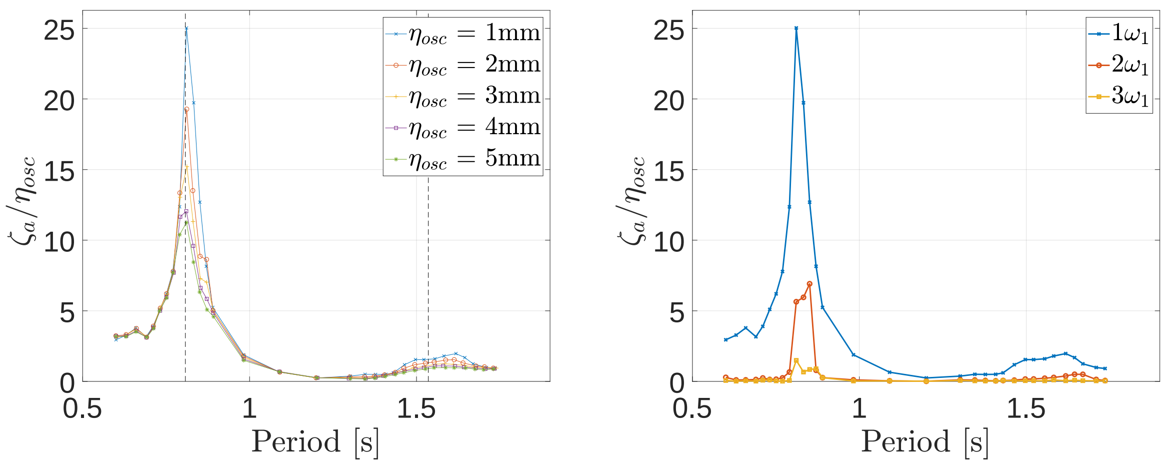

(a) RAO for all forcing amplitudes.

(b) Three first harmonics, with $\eta_{osc} = 0.001$m.

Figure E.53: RAOs at MP4 for $L_R = 0.15$m and draft 0.12m. Dashed lines in (a) show how estimates of natural periods of 1st sloshing mode(left) and piston mode(right) compare

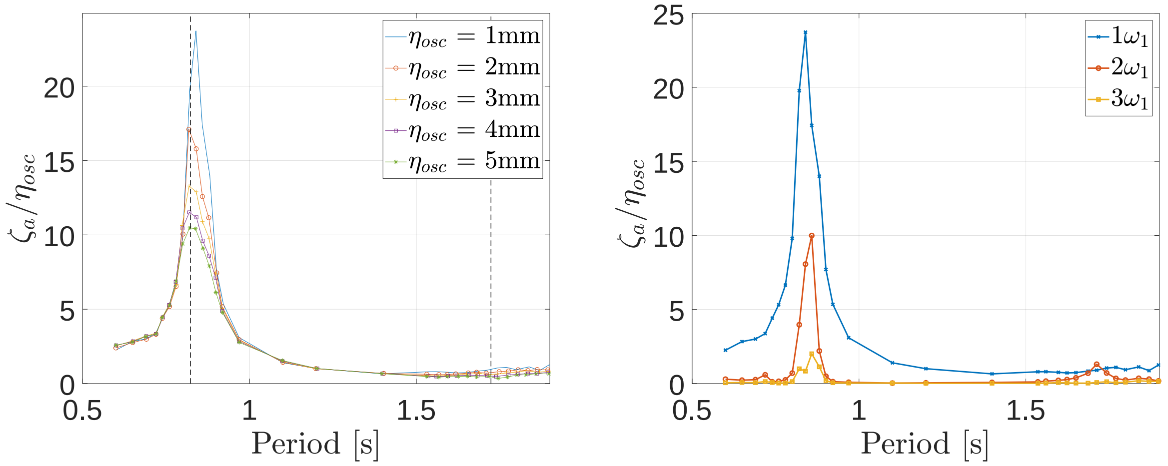

(a) RAO for all forcing amplitudes.

(b) Three first harmonics

Figure E.54: RAOs at MP4 for L_R = 0.2m and draft 0.12m. Dashed lines in (a) show how estimates of natural periods of 1st sloshing mode(left) and piston mode(right) compare

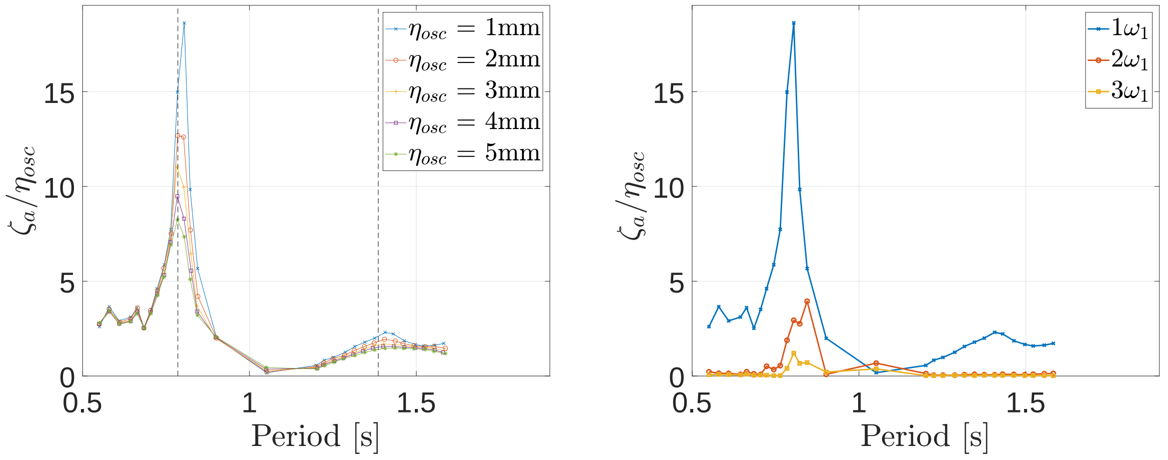

(a) RAO for all forcing amplitudes.

(b) Three first harmonics, with η_{osc} = 0.001m.

Figure E.55: RAOs at MP4 for L_R = 0.1m and draft 0.11m. Dashed lines in (a) show how estimates of natural periods of 1st sloshing mode(left) and piston mode(right) compare

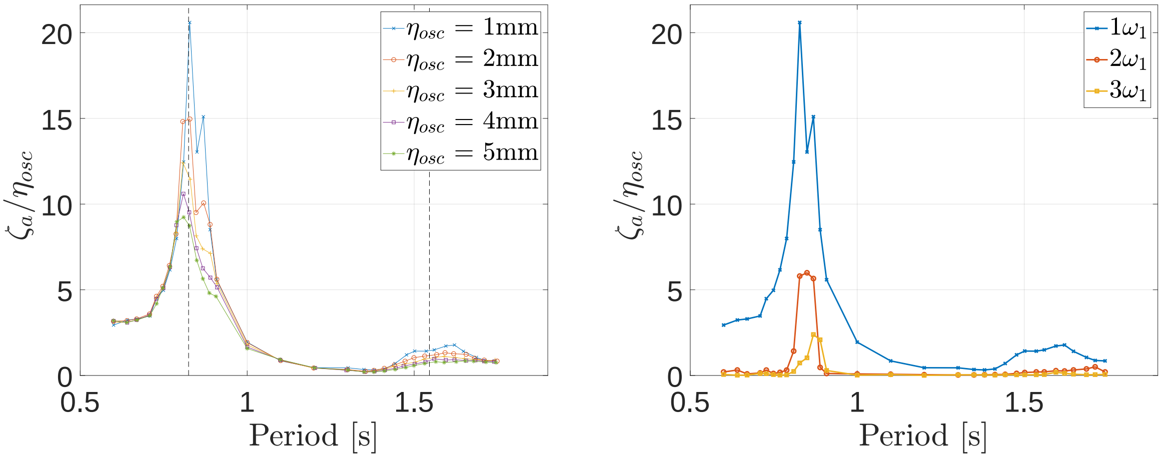

(a) RAO for all forcing amplitudes.

(b) Three first harmonics

Figure E.56: RAOs at MP4 for L_R = 0.15m and draft 0.11m. Dashed lines in (a) show how estimates of natural periods of 1st sloshing mode(left) and piston mode(right) compare

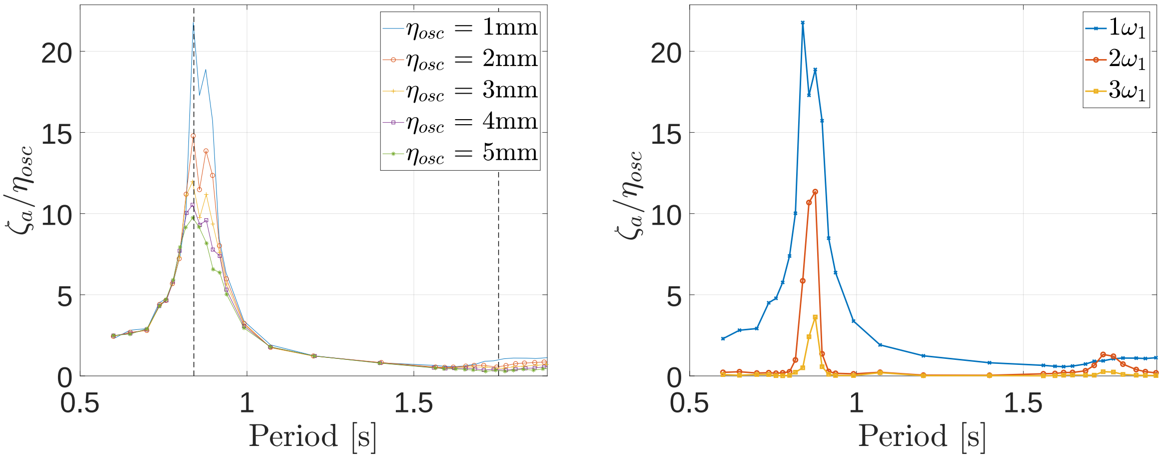

(a) RAO for all forcing amplitudes.

(b) Three first harmonics, with η_{osc} = 0.001m.

Figure E.57: RAOs at MP4 for L_R = 0.2m and draft 0.11m. Dashed lines in (a) show how estimates of natural periods of 1st sloshing mode(left) and piston mode(right) compare

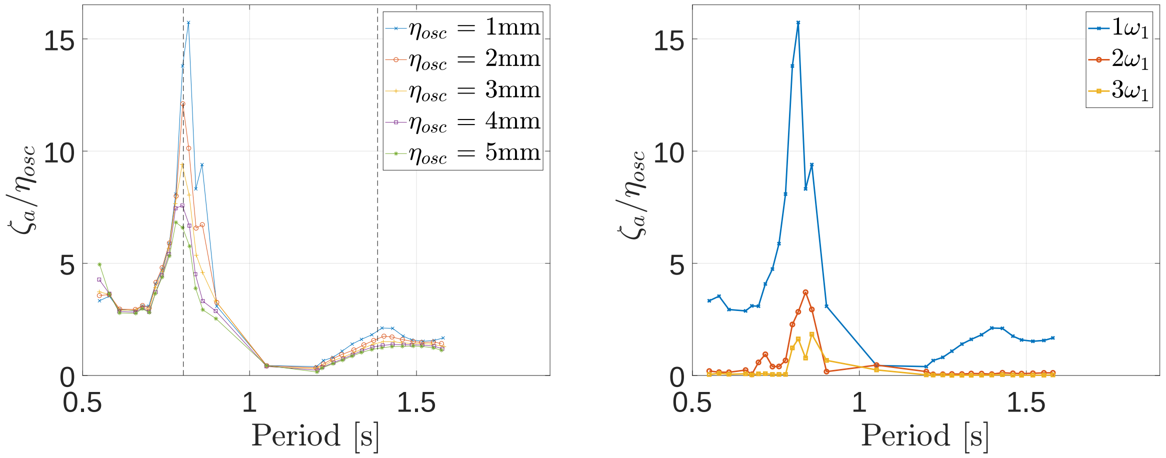

(a) RAO for all forcing amplitudes.

(b) Three first harmonics, with $\eta_{osc} = 0.001$m.

Figure E.58: RAOs at MP4 for $L_R = 0.1$m and draft 0.10m. Dashed lines in (a) show how estimates of natural periods of 1st sloshing mode(left) and piston mode(right) compare

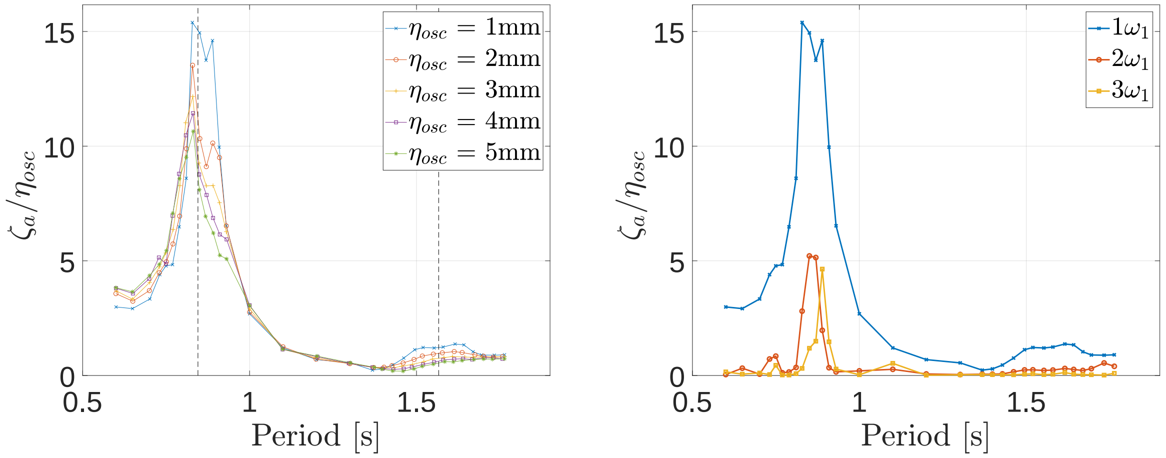

(a) RAO for all forcing amplitudes.

(b) Three first harmonics, with $\eta_{osc} = 0.001$m.

Figure E.59: RAOs at MP4 for $L_R = 0.15$m and draft 0.10m. Dashed lines in (a) show how estimates of natural periods of 1st sloshing mode(left) and piston mode(right) compare

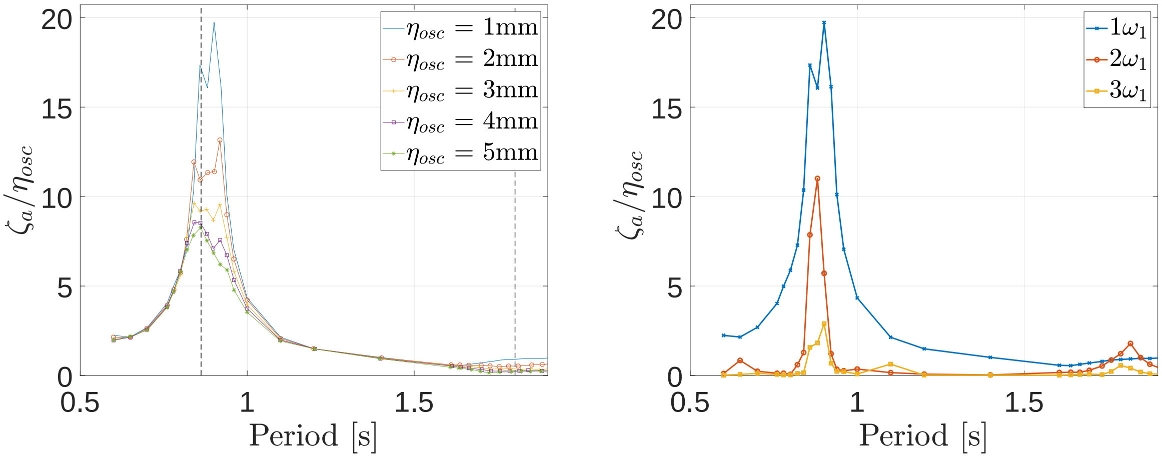

(a) RAO for all forcing amplitudes.

(b) Three first harmonics, with $\eta_{osc} = 0.001$m.

Figure E.60: RAOs at MP4 for $L_R = 0.2$m and draft 0.10m. Dashed lines in (a) show how estimates of natural periods of 1st sloshing mode(left) and piston mode(right) compare

RAOs for MP6

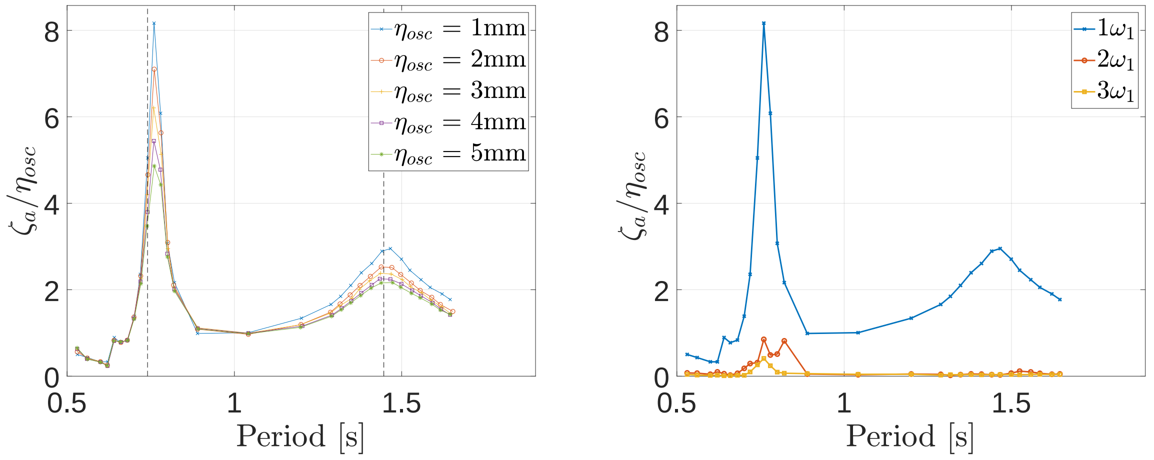

(a) RAO for all forcing amplitudes.

(b) Three first harmonics, with $\eta_{osc} = 0.001$m.

Figure E.61: RAOs at MP6 for L_R = 0.1m and draft 0.17m. Dashed lines in (a) show how estimates of natural periods of 1st sloshing mode(left) and piston mode(right) compare

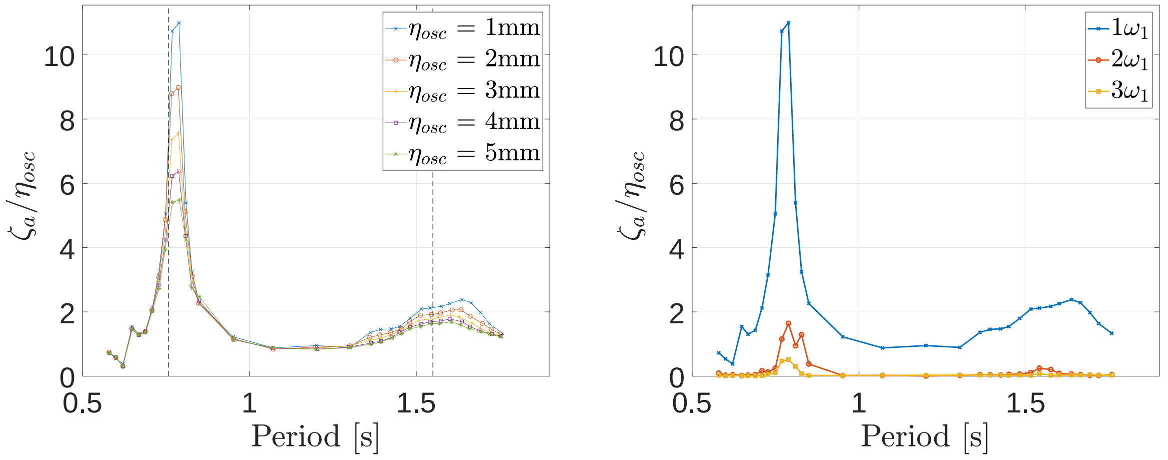

(a) RAO for all forcing amplitudes.

(b) Three first harmonics, with $\eta_{osc} = 0.001$m.

Figure E.62: RAOs at MP6 for L_R = 0.15m and draft 0.17m. Dashed lines in (a) show how estimates of natural periods of 1st sloshing mode(left) and piston mode(right) compare

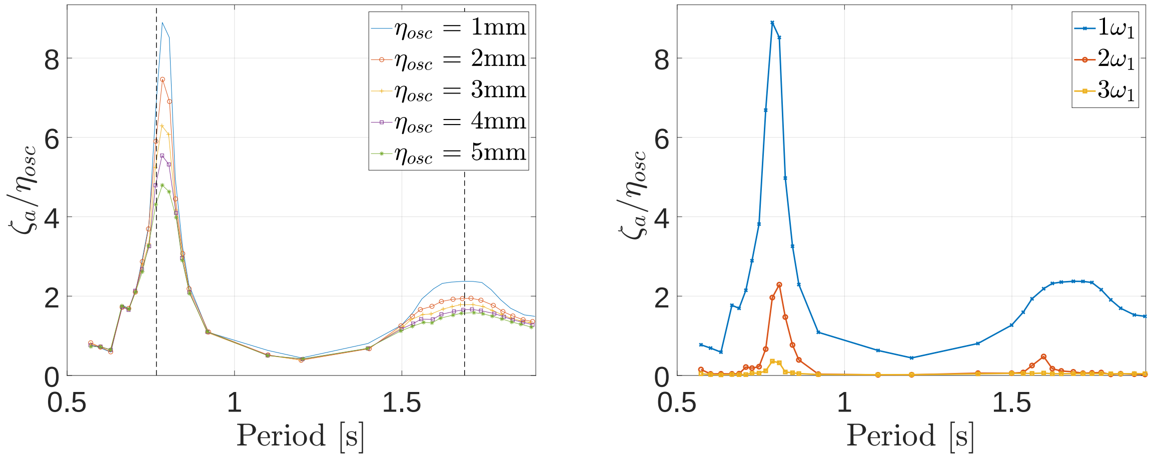

(a) RAO for all forcing amplitudes. (b) Three first harmonics, with $\eta_{osc} = 0.001$m.

Figure E.63: RAOs at MP6 for $L_R = 0.2$m and draft 0.17m. Dashed lines in (a) show how estimates of natural periods of 1st sloshing mode(left) and piston mode(right) compare

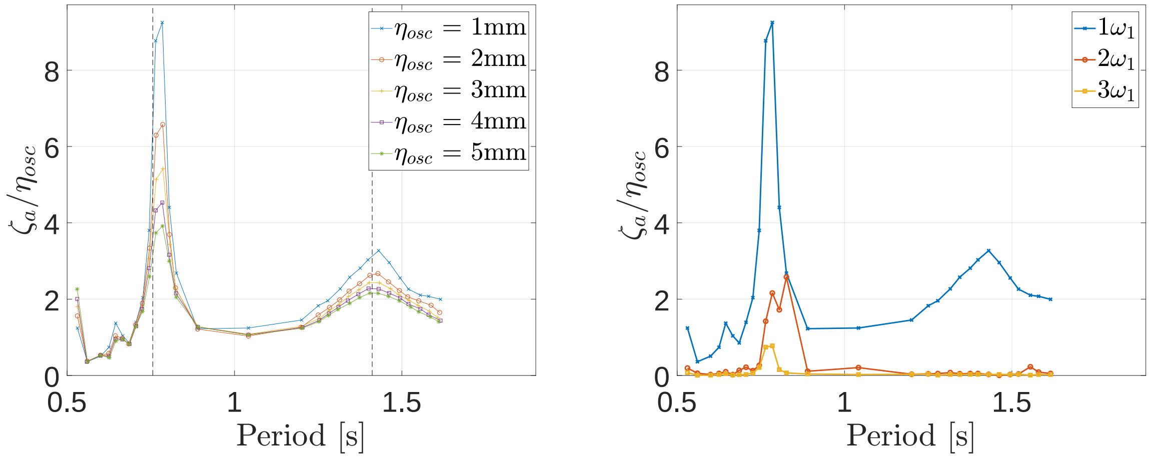

(a) RAO for all forcing amplitudes. (b) Three first harmonics, with $\eta_{osc} = 0.001$m.

Figure E.64: RAOs at MP6 for $L_R = 0.1$m and draft 0.14m. Dashed lines in (a) show how estimates of natural periods of 1st sloshing mode(left) and piston mode(right) compare

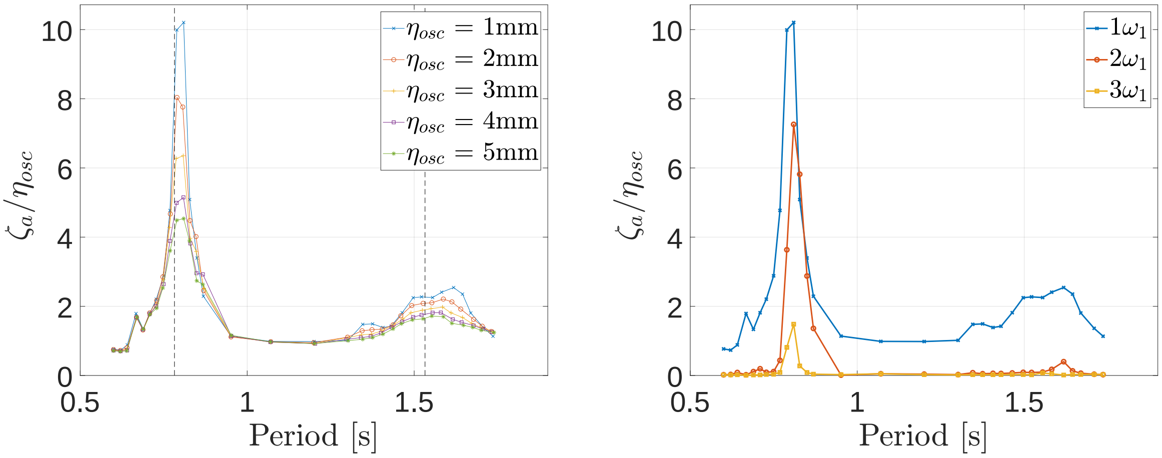

(a) RAO for all forcing amplitudes.

(b) Three first harmonics, with $\eta_{osc} = 0.001$m.

Figure E.65: RAOs at MP6 for L_R = 0.15m and draft 0.14m. Dashed lines in (a) show how estimates of natural periods of 1st sloshing mode(left) and piston mode(right) compare

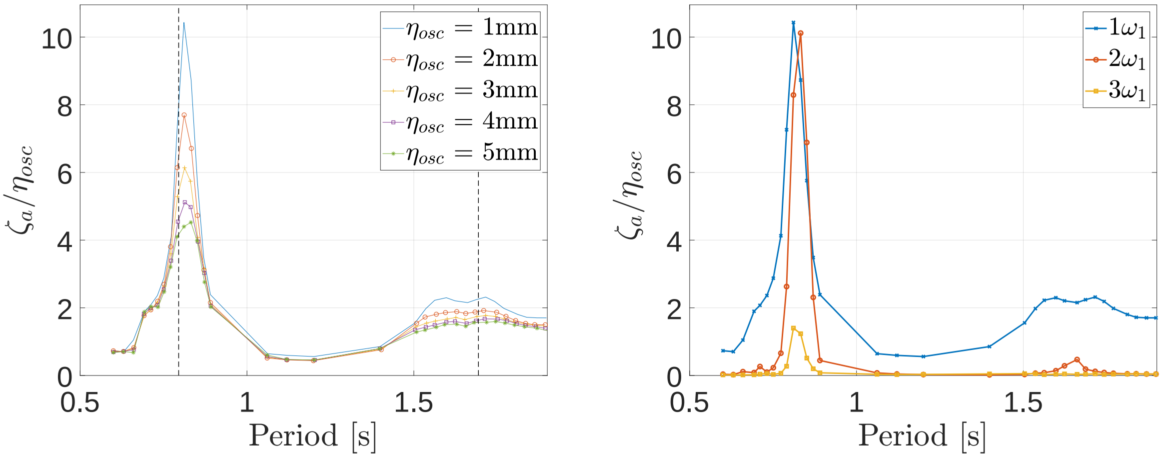

(a) RAO for all forcing amplitudes.

(b) Three first harmonics, with $\eta_{osc} = 0.001$m.

Figure E.66: RAOs at MP6 for L_R = 0.2m and draft 0.14m. Dashed lines in (a) show how estimates of natural periods of 1st sloshing mode(left) and piston mode(right) compare

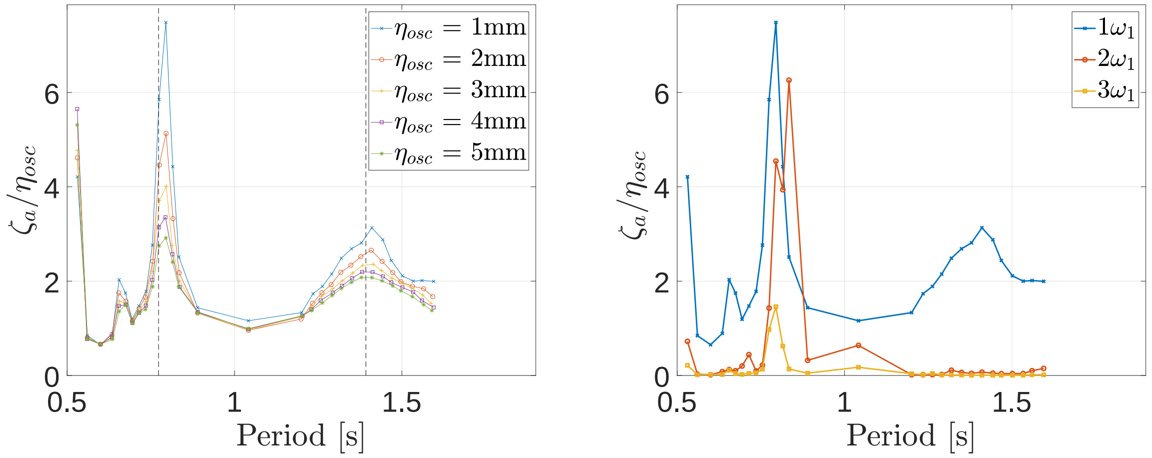

(a) RAO for all forcing amplitudes.

(b) Three first harmonics, with $\eta_{osc} = 0.001$m.

Figure E.67: RAOs at MP6 for $L_R = 0.1$m and draft 0.12m. Dashed lines in (a) show how estimates of natural periods of 1st sloshing mode(left) and piston mode(right) compare

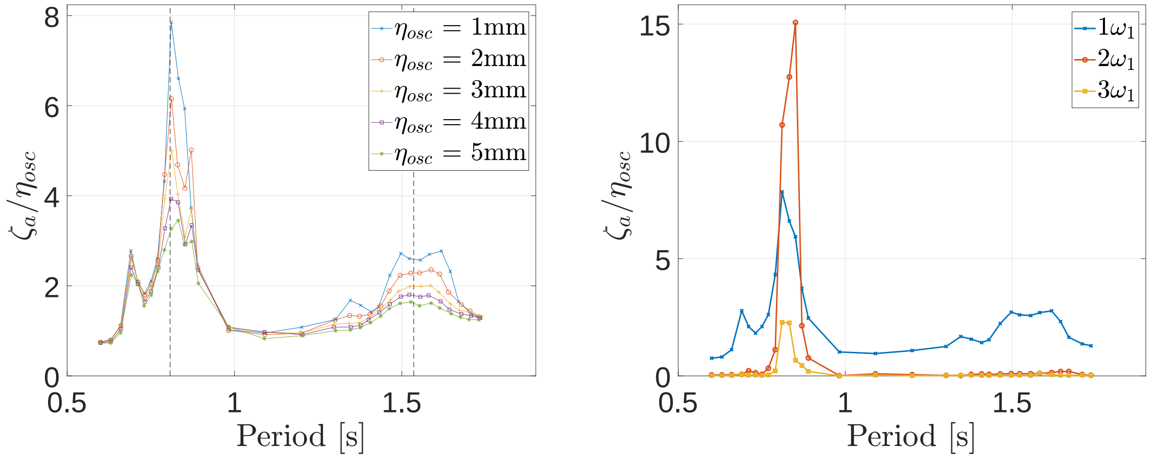

(a) RAO for all forcing amplitudes.

(b) Three first harmonics, with $\eta_{osc} = 0.001$m.

Figure E.68: RAOs at MP6 for $L_R = 0.15$m and draft 0.12m. Dashed lines in (a) show how estimates of natural periods of 1st sloshing mode(left) and piston mode(right) compare

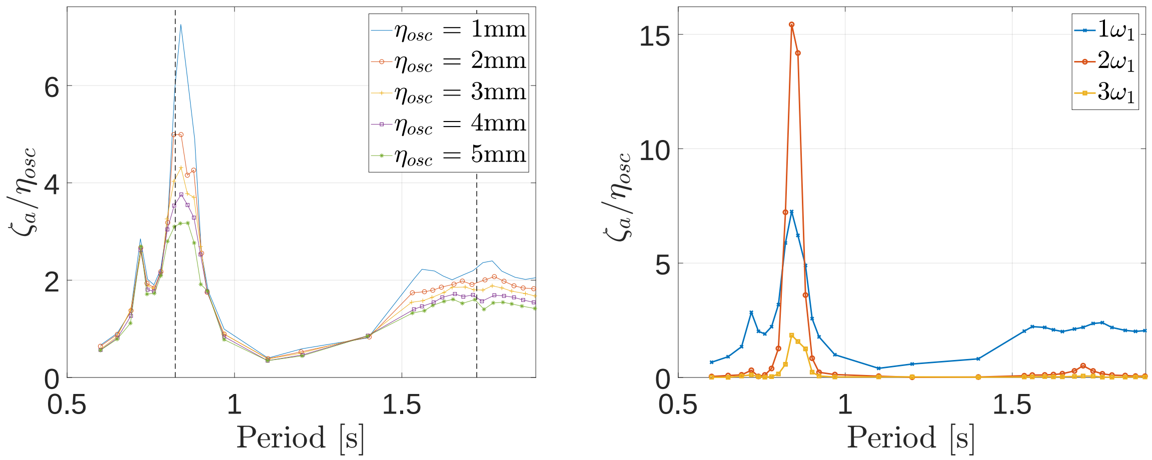

(a) RAO for all forcing amplitudes.

(b) Three first harmonics

Figure E.69: RAOs at MP6 for L_R = 0.2m and draft 0.12m. Dashed lines in (a) show how estimates of natural periods of 1st sloshing mode(left) and piston mode(right) compare

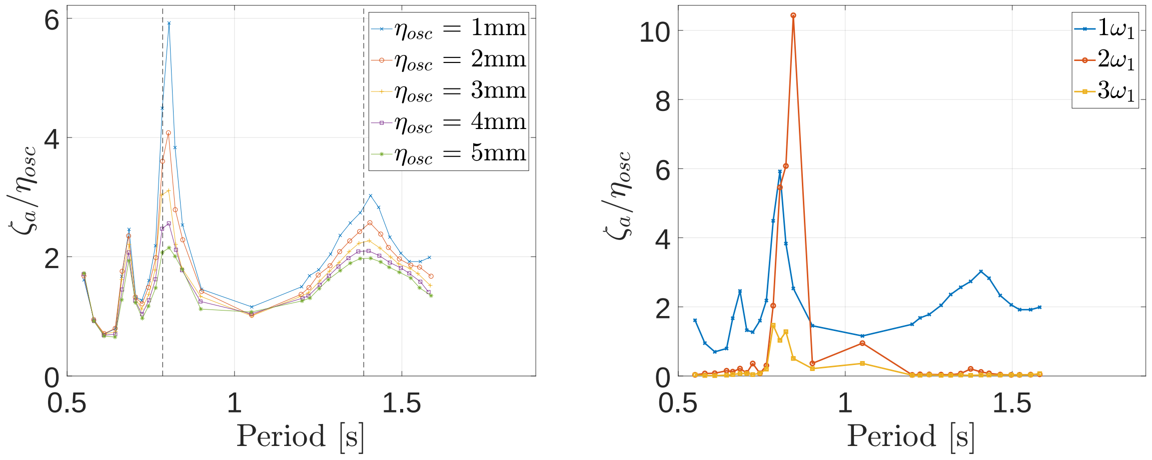

(a) RAO for all forcing amplitudes.

(b) Three first harmonics, with η_{osc} = 0.001m.

Figure E.70: RAOs at MP6 for L_R = 0.1m and draft 0.11m. Dashed lines in (a) show how estimates of natural periods of 1st sloshing mode(left) and piston mode(right) compare

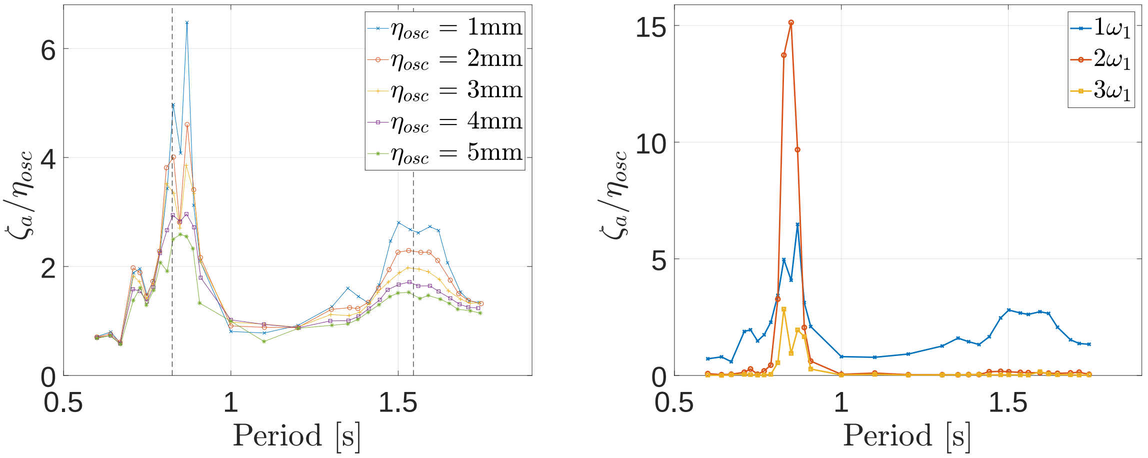

(a) RAO for all forcing amplitudes.

(b) Three first harmonics, with $\eta_{osc} = 0.001$m.

Figure E.71: RAOs at MP6 for L_R = 0.15m and draft 0.11m. Dashed lines in (a) show how estimates of natural periods of 1st sloshing mode(left) and piston mode(right) compare

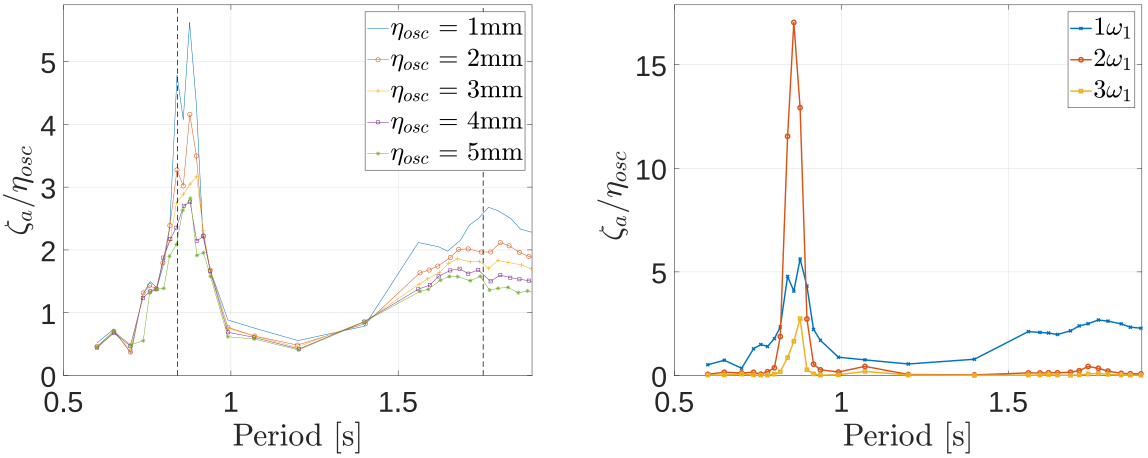

(a) RAO for all forcing amplitudes.

(b) Three first harmonics, with $\eta_{osc} = 0.001$m.

Figure E.72: RAOs at MP6 for L_R = 0.2m and draft 0.11m. Dashed lines in (a) show how estimates of natural periods of 1st sloshing mode(left) and piston mode(right) compare

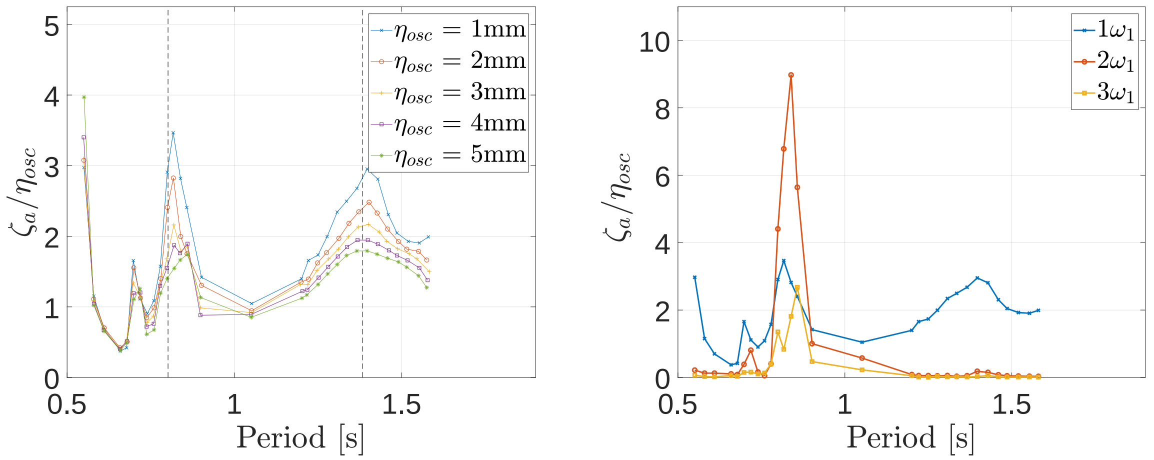

(a) RAO for all forcing amplitudes.

(b) Three first harmonics, with η_{osc} = 0.001m.

Figure E.73: RAOs at MP6 for L_R = 0.1m and draft 0.10m. Dashed lines in (a) show how estimates of natural periods of 1st sloshing mode(left) and piston mode(right) compare

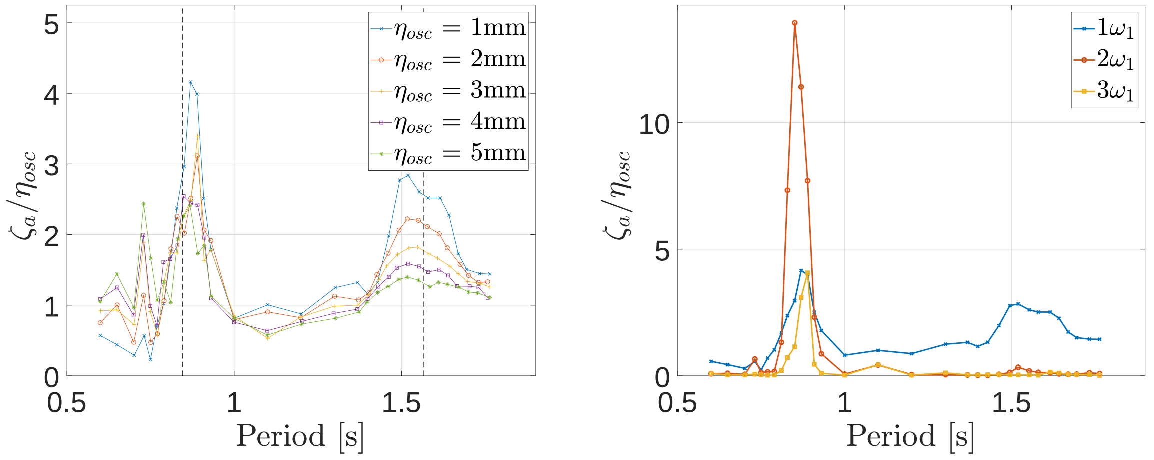

(a) RAO for all forcing amplitudes.

(b) Three first harmonics, with η_{osc} = 0.001m.

Figure E.74: RAOs at MP6 for L_R = 0.15m and draft 0.10m. Dashed lines in (a) show how estimates of natural periods of 1st sloshing mode(left) and piston mode(right) compare

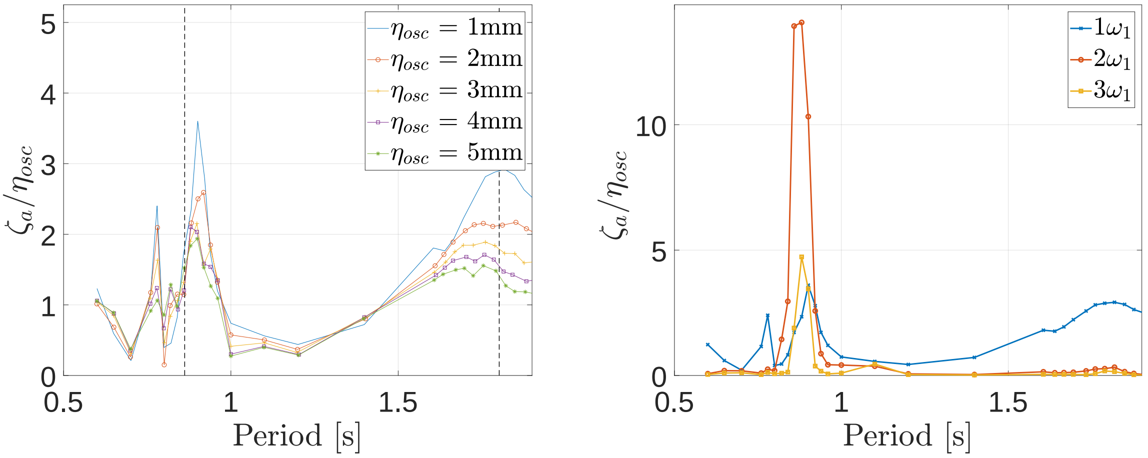

(a) RAO for all forcing amplitudes.

(b) Three first harmonics, with $\eta_{osc} = 0.001$m.

Figure E.75: RAOs at MP6 for $L_R = 0.2$m and draft 0.10m. Dashed lines in (a) show how estimates of natural periods of 1st sloshing mode(left) and piston mode(right) compare

RAOs for MP7

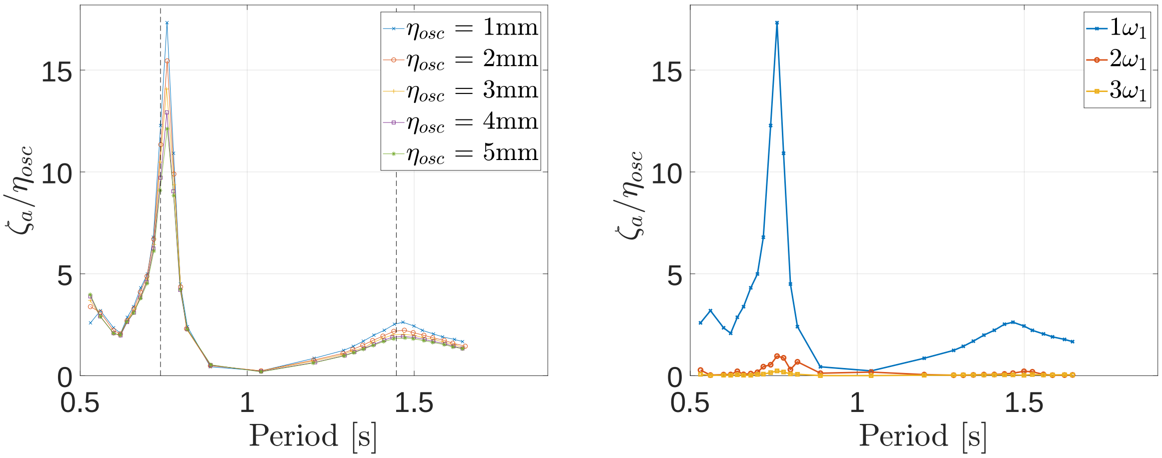

(a) RAO for all forcing amplitudes. (b) Three first harmonics, with $\eta_{osc} = 0.001$m.

Figure E.76: RAOs at MP7 for $L_R = 0.1$m and draft 0.17m. Dashed lines in (a) show how estimates of natural periods of 1st sloshing mode(left) and piston mode(right) compare

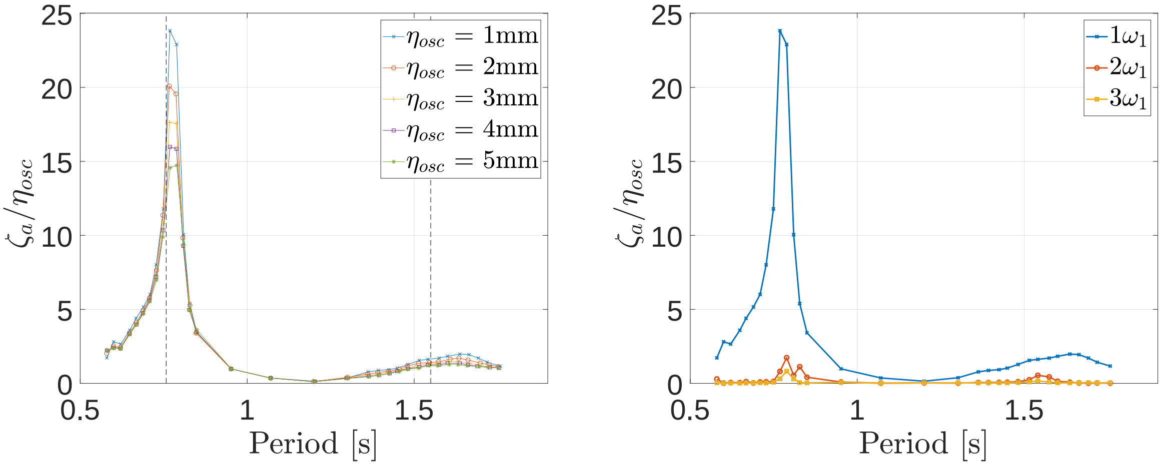

(a) RAO for all forcing amplitudes. (b) Three first harmonics, with $\eta_{osc} = 0.001$m.

Figure E.77: RAOs at MP7 for $L_R = 0.15$m and draft 0.17m. Dashed lines in (a) show how estimates of natural periods of 1st sloshing mode(left) and piston mode(right) compare

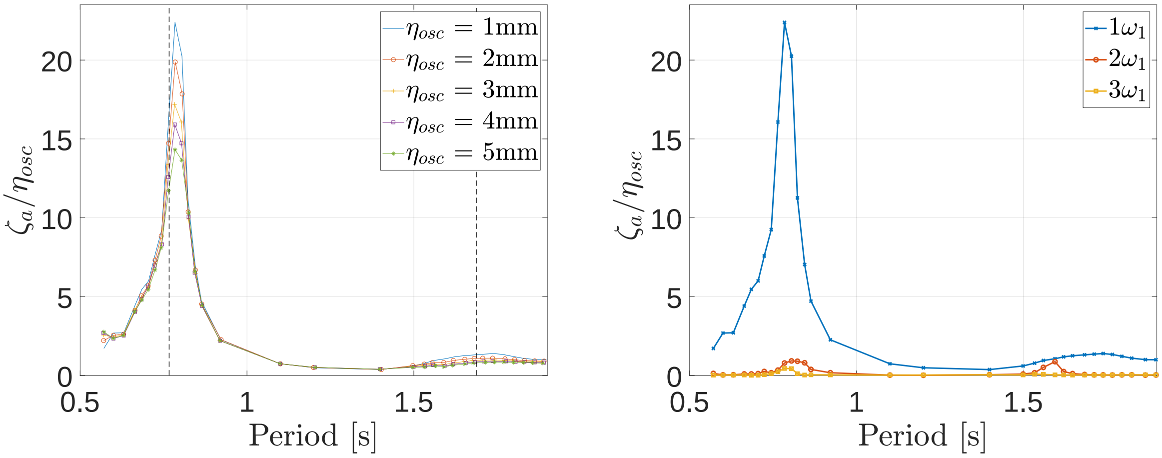

(a) RAO for all forcing amplitudes.

(b) Three first harmonics, with $\eta_{osc} = 0.001$m.

Figure E.78: RAOs at MP7 for $L_R = 0.2$m and draft 0.17m. Dashed lines in (a) show how estimates of natural periods of 1st sloshing mode(left) and piston mode(right) compare

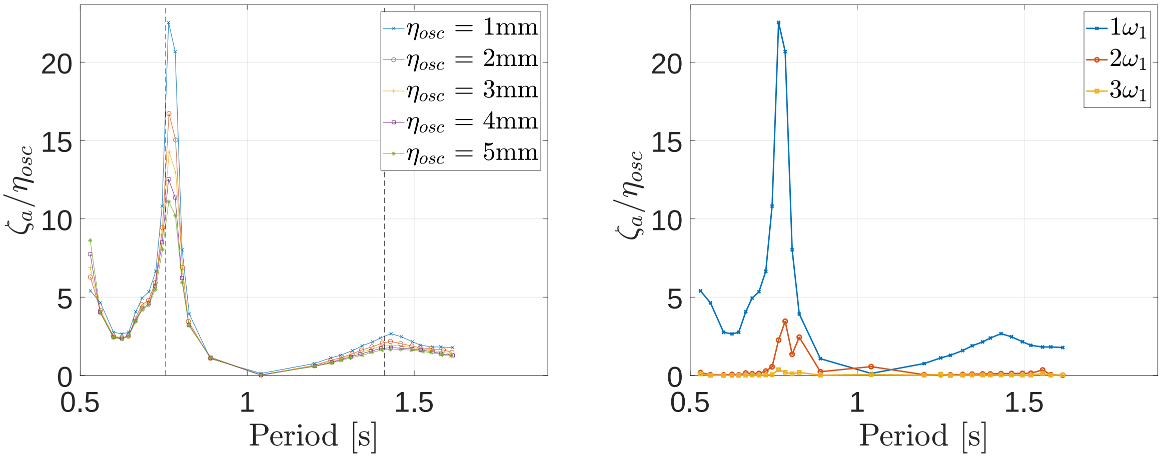

(a) RAO for all forcing amplitudes.

(b) Three first harmonics, with $\eta_{osc} = 0.001$m.

Figure E.79: RAOs at MP7 for $L_R = 0.1$m and draft 0.14m. Dashed lines in (a) show how estimates of natural periods of 1st sloshing mode(left) and piston mode(right) compare

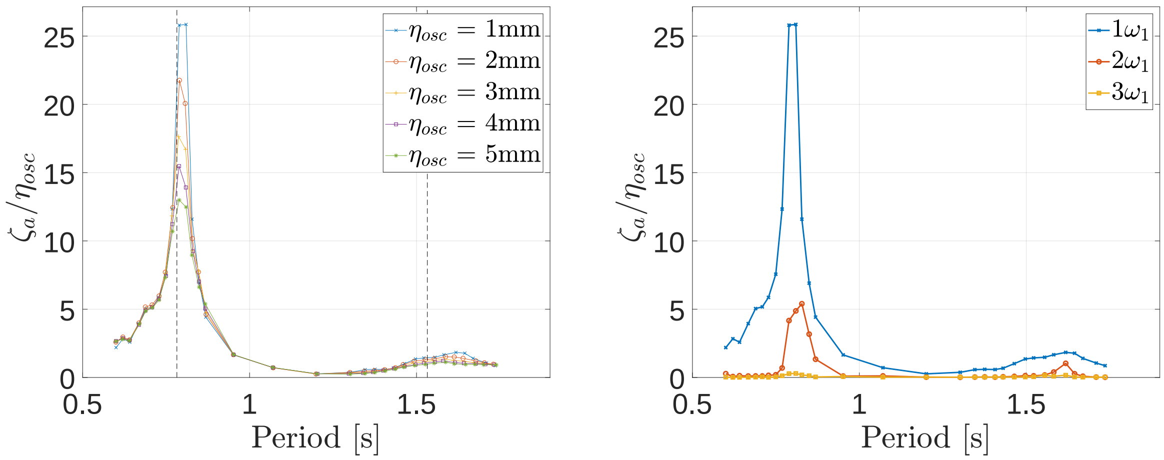

(a) RAO for all forcing amplitudes. (b) Three first harmonics, with η_{osc} = 0.001m.

Figure E.80: RAOs at MP7 for L_R = 0.15m and draft 0.14m. Dashed lines in (a) show how estimates of natural periods of 1st sloshing mode(left) and piston mode(right) compare

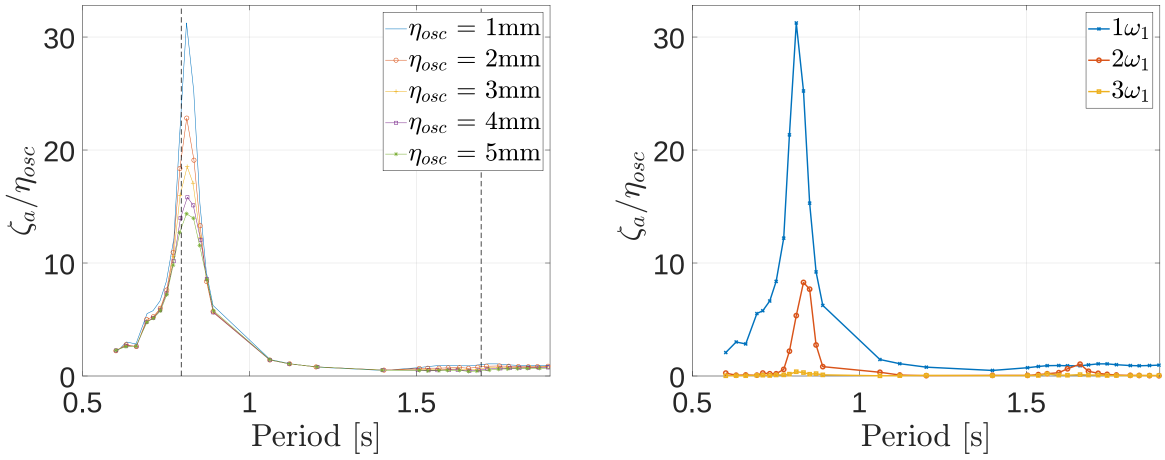

(a) RAO for all forcing amplitudes. (b) Three first harmonics, with η_{osc} = 0.001m.

Figure E.81: RAOs at MP7 for L_R = 0.2m and draft 0.14m. Dashed lines in (a) show how estimates of natural periods of 1st sloshing mode(left) and piston mode(right) compare

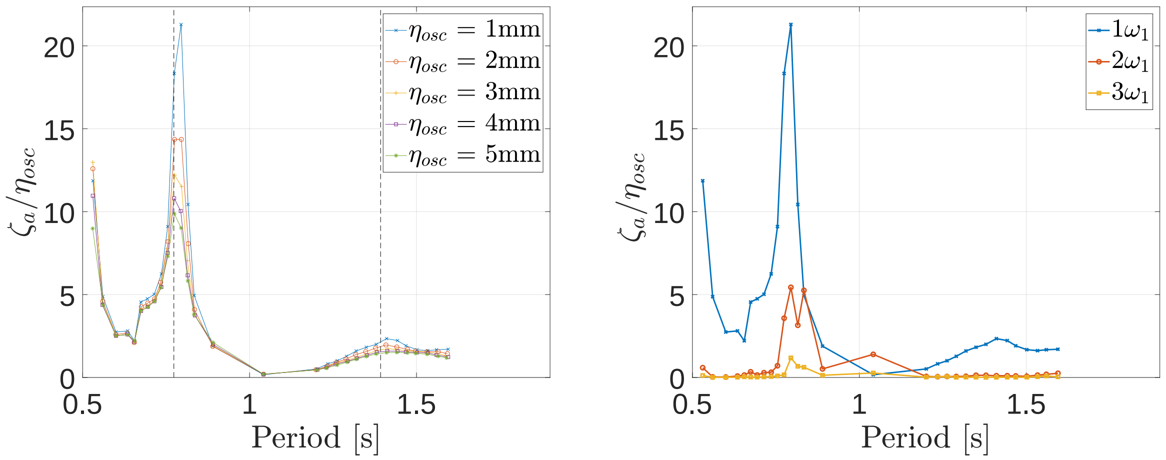

(a) RAO for all forcing amplitudes.

(b) Three first harmonics, with η_{osc} = 0.001m.

Figure E.82: RAOs at MP7 for L_R = 0.1m and draft 0.12m. Dashed lines in (a) show how estimates of natural periods of 1st sloshing mode(left) and piston mode(right) compare

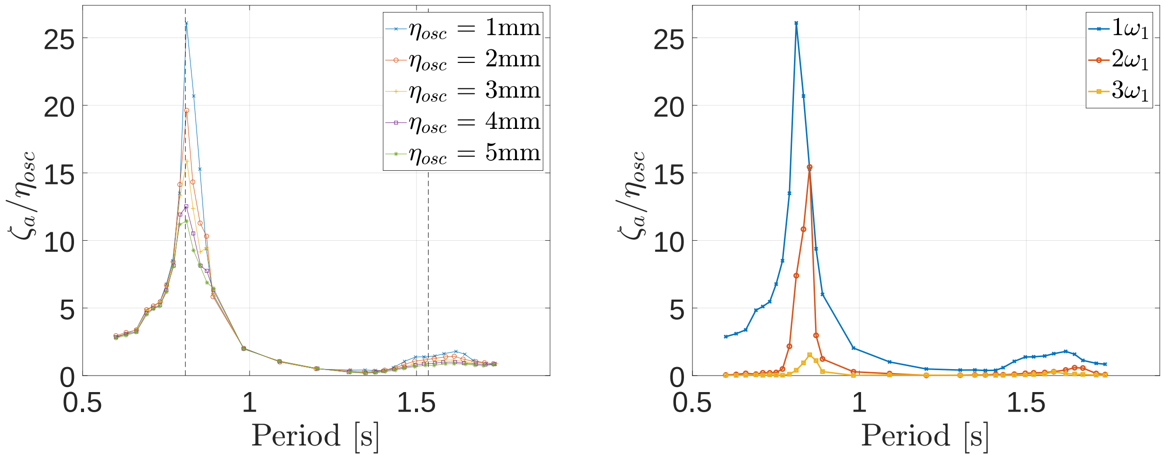

(a) RAO for all forcing amplitudes.

(b) Three first harmonics, with η_{osc} = 0.001m.

Figure E.83: RAOs at MP7 for L_R = 0.15m and draft 0.12m. Dashed lines in (a) show how estimates of natural periods of 1st sloshing mode(left) and piston mode(right) compare

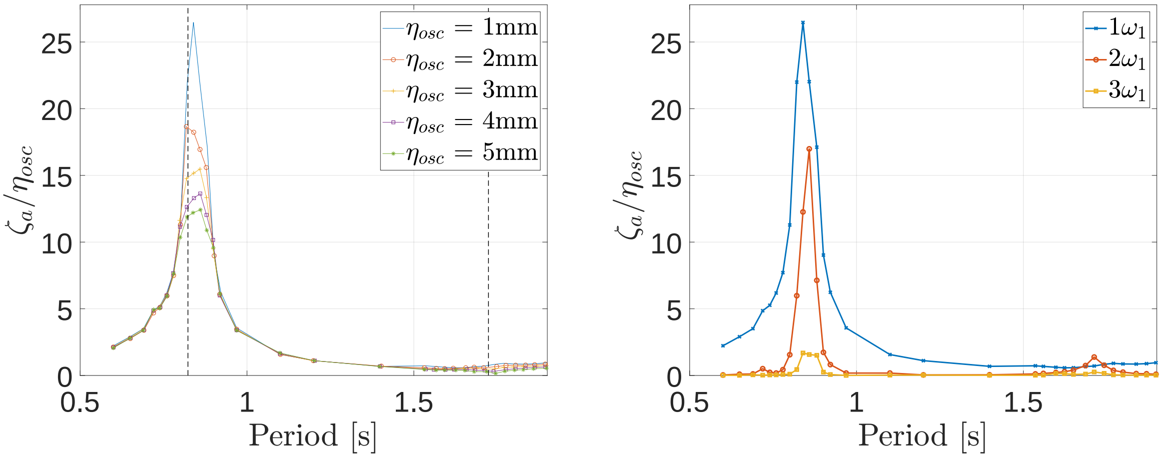

(a) RAO for all forcing amplitudes.

(b) Three first harmonics, with $\eta_{osc} = 0.001$m.

Figure E.84: RAOs at MP7 for $L_R = 0.2$m and draft 0.12m. Dashed lines in (a) show how estimates of natural periods of 1st sloshing mode(left) and piston mode(right) compare

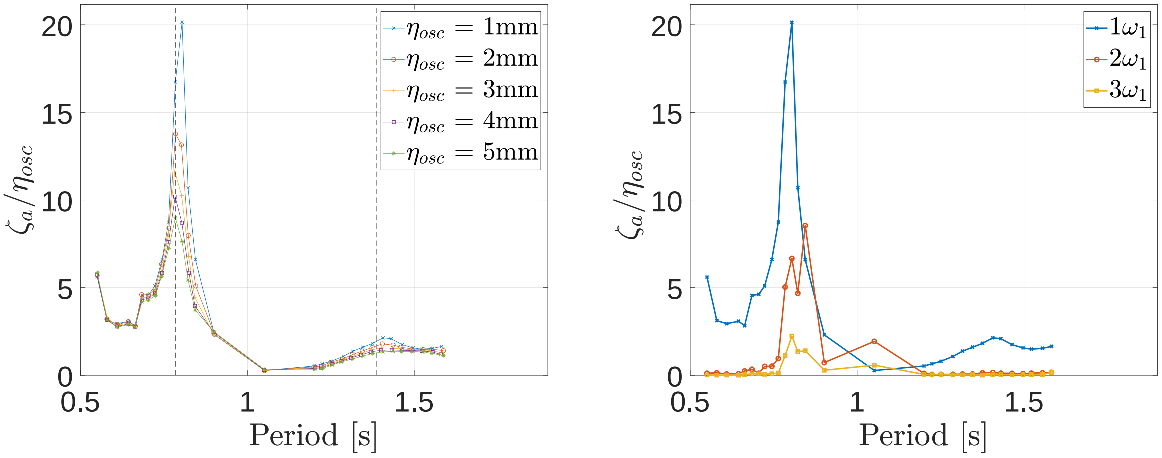

(a) RAO for all forcing amplitudes.

(b) Three first harmonics, with $\eta_{osc} = 0.001$m.

Figure E.85: RAOs at MP7 for $L_R = 0.1$m and draft 0.11m. Dashed lines in (a) show how estimates of natural periods of 1st sloshing mode(left) and piston mode(right) compare

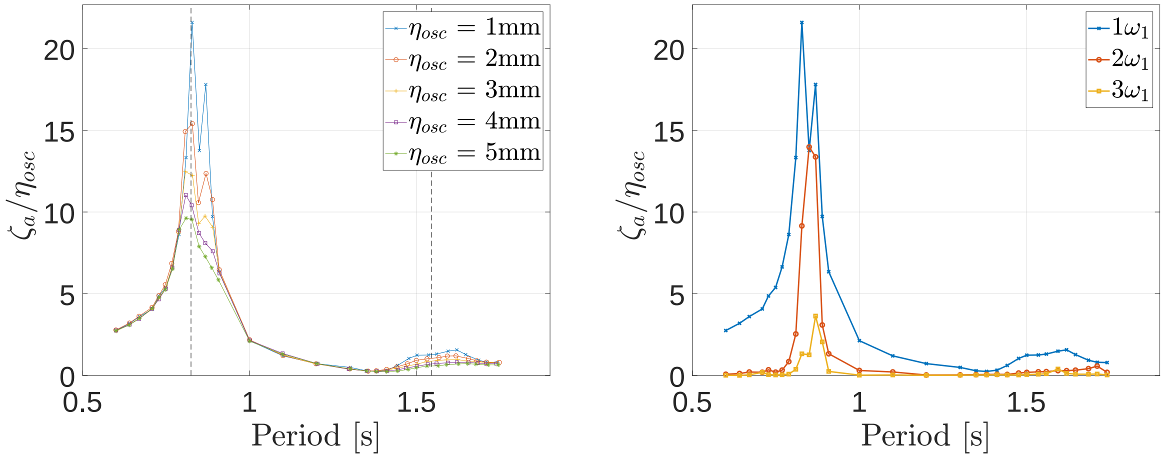

(a) RAO for all forcing amplitudes.

(b) Three first harmonics, with $\eta_{osc} = 0.001$m.

Figure E.86: RAOs at MP7 for $L_R = 0.15$m and draft 0.11m. Dashed lines in (a) show how estimates of natural periods of 1st sloshing mode(left) and piston mode(right) compare

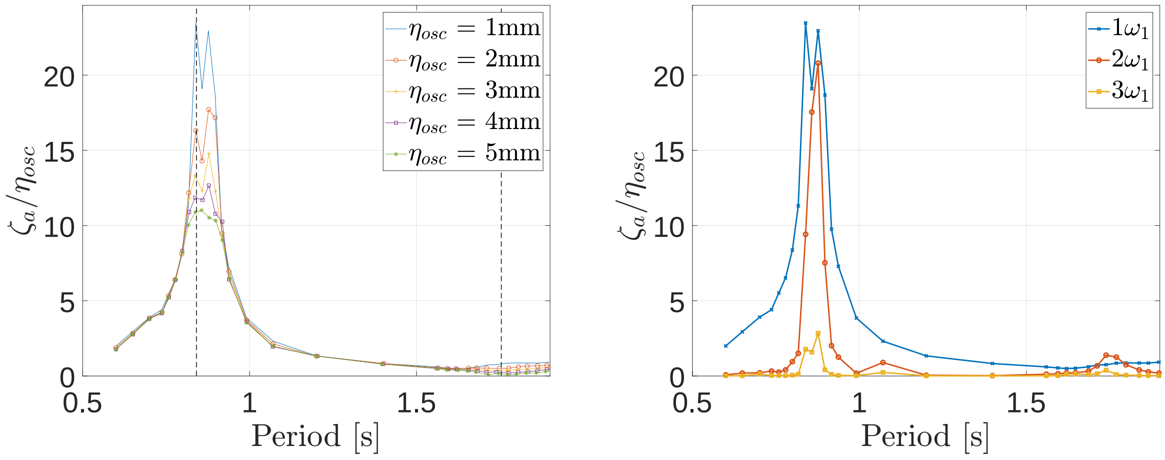

(a) RAO for all forcing amplitudes.

(b) Three first harmonics, with $\eta_{osc} = 0.001$m.

Figure E.87: RAOs at MP7 for $L_R = 0.2$m and draft 0.11m. Dashed lines in (a) show how estimates of natural periods of 1st sloshing mode(left) and piston mode(right) compare

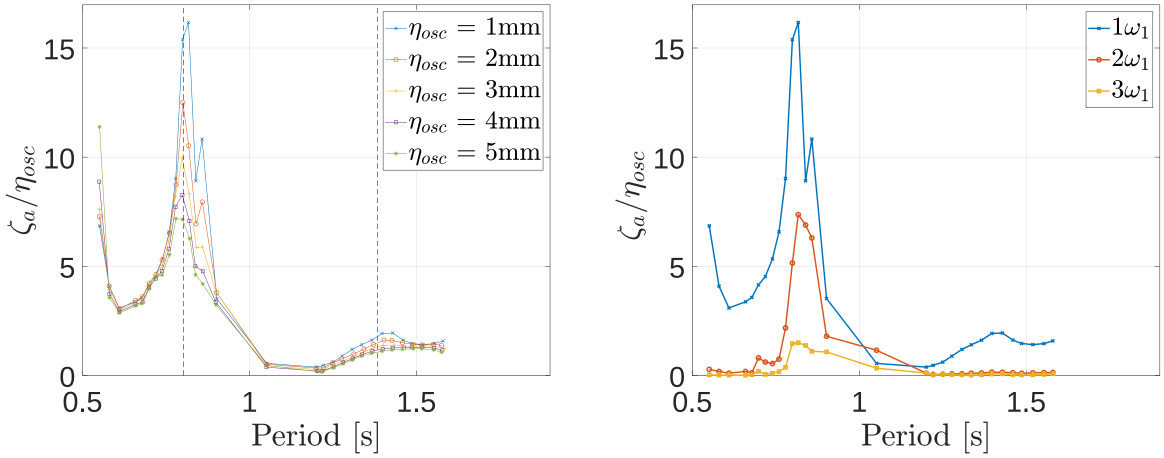

(a) RAO for all forcing amplitudes.

(b) Three first harmonics, with $\eta_{osc} = 0.001$m.

Figure E.88: RAOs at MP7 for $L_R = 0.1$m and draft 0.10m. Dashed lines in (a) show how estimates of natural periods of 1st sloshing mode(left) and piston mode(right) compare

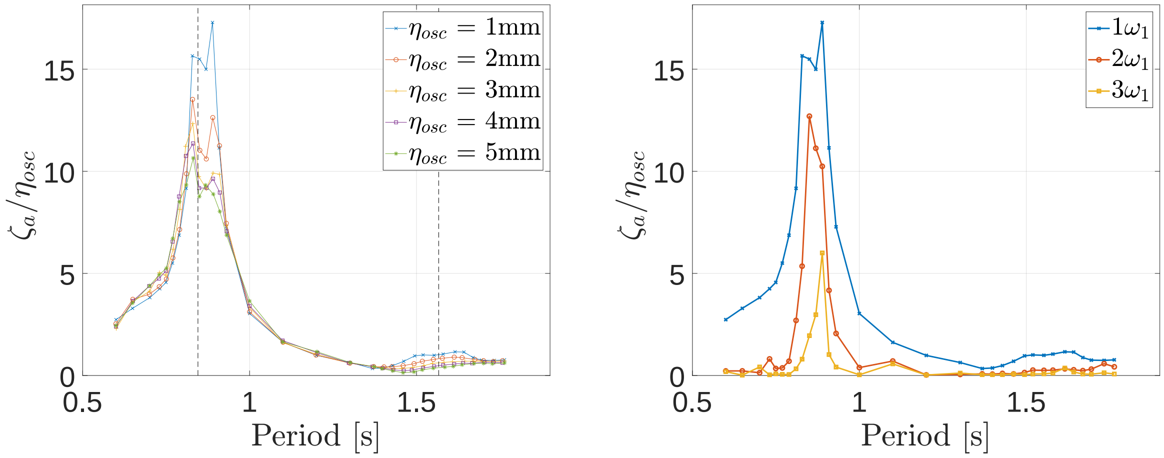

(a) RAO for all forcing amplitudes.

(b) Three first harmonics, with $\eta_{osc} = 0.001$m.

Figure E.89: RAOs at MP7 for $L_R = 0.15$m and draft 0.10m. Dashed lines in (a) show how estimates of natural periods of 1st sloshing mode(left) and piston mode(right) compare

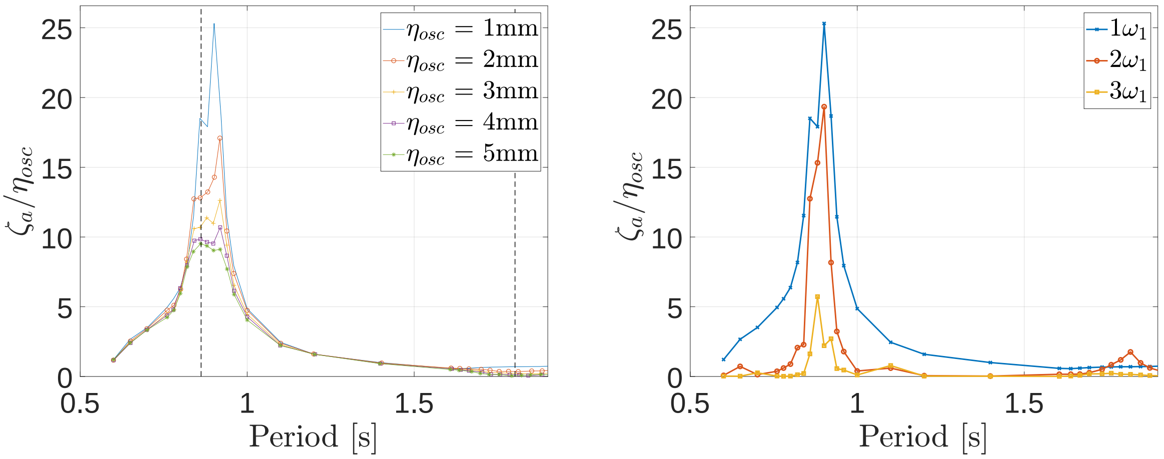

(a) RAO for all forcing amplitudes.

(b) Three first harmonics, with $\eta_{osc} = 0.001$m.

Figure E.90: RAOs at MP7 for $L_R = 0.2$m and draft 0.10m. Dashed lines in (a) show how estimates of natural periods of 1st sloshing mode(left) and piston mode(right) compare

RAOs for MP9

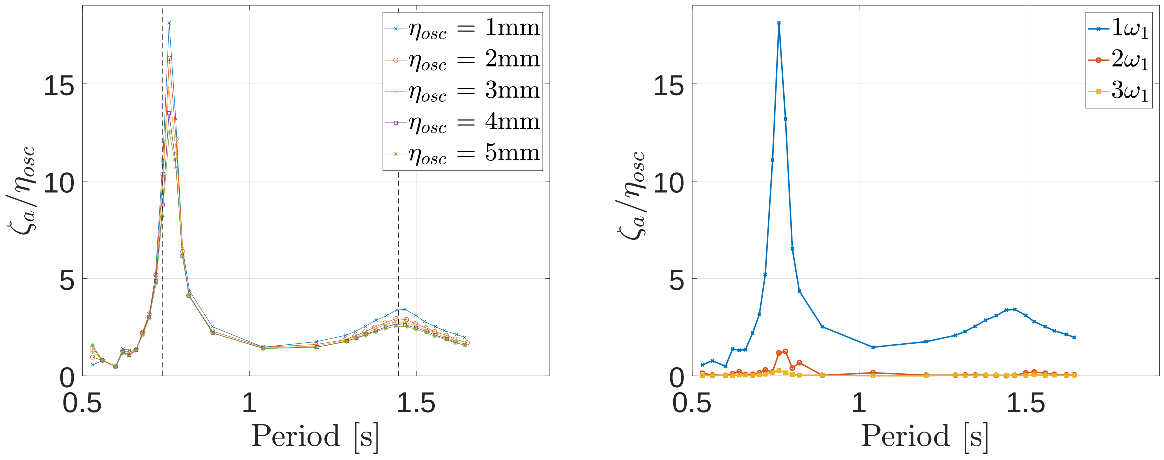

(a) RAO for all forcing amplitudes.

(b) Three first harmonics, with $\eta_{osc} = 0.001$m.

Figure E.91: RAOs at MP9 for $L_R = 0.1$m and draft 0.17m. Dashed lines in (a) show how estimates of natural periods of 1st sloshing mode(left) and piston mode(right) compare

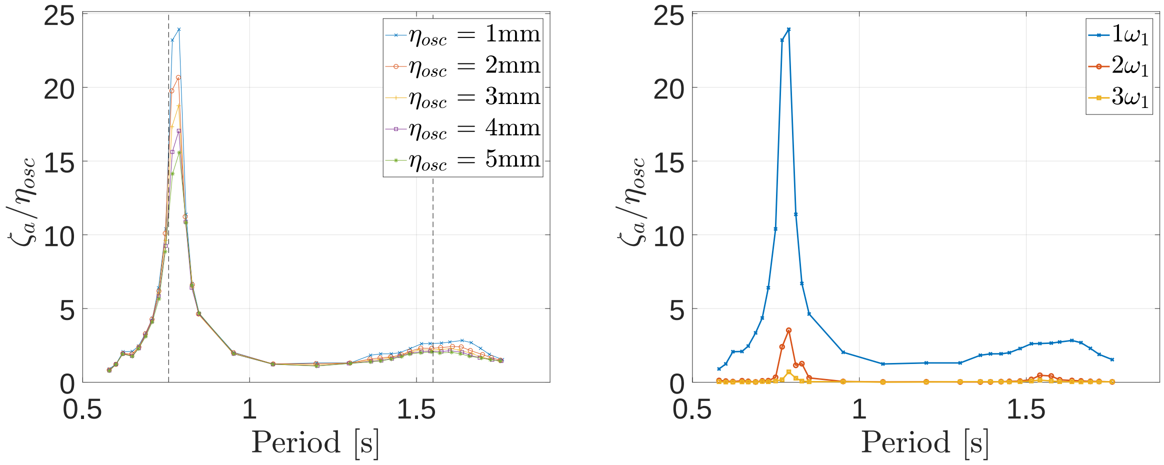

(a) RAO for all forcing amplitudes.

(b) Three first harmonics, with $\eta_{osc} = 0.001$m.

Figure E.92: RAOs at MP9 for $L_R = 0.15$m and draft 0.17m. Dashed lines in (a) show how estimates of natural periods of 1st sloshing mode(left) and piston mode(right) compare

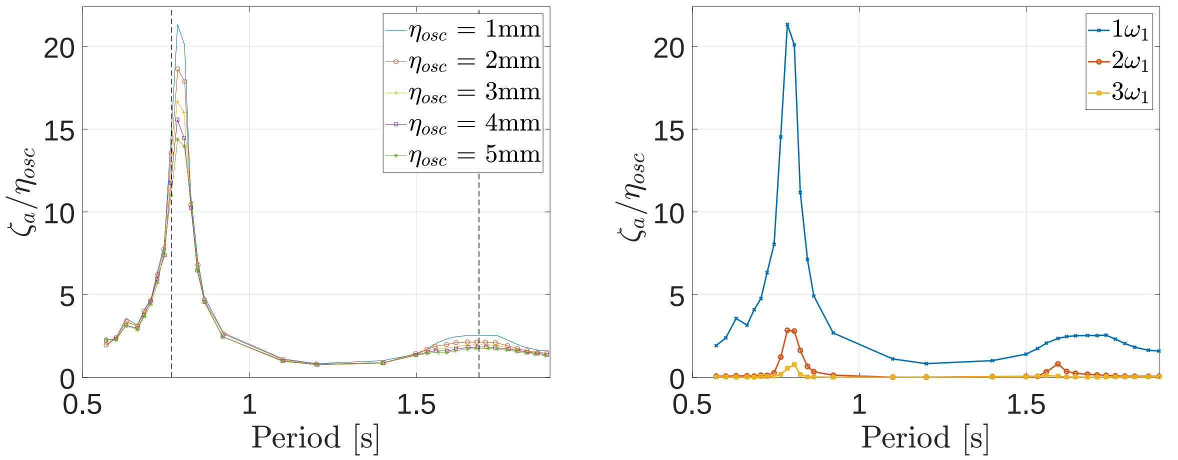

(a) RAO for all forcing amplitudes.

(b) Three first harmonics, with $\eta_{osc} = 0.001$m.

Figure E.93: RAOs at MP9 for $L_R = 0.2$m and draft 0.17m. Dashed lines in (a) show how estimates of natural periods of 1st sloshing mode(left) and piston mode(right) compare

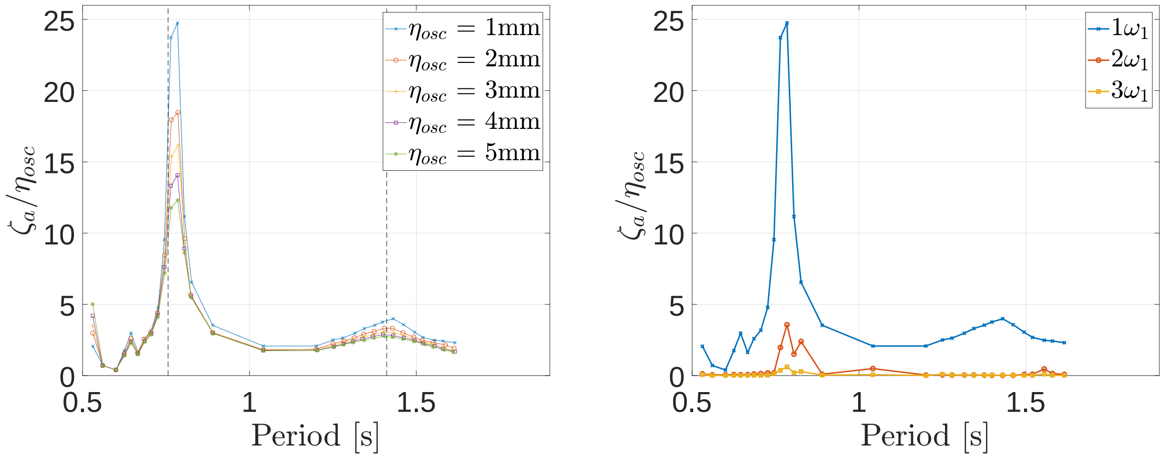

(a) RAO for all forcing amplitudes.

(b) Three first harmonics, with $\eta_{osc} = 0.001$m.

Figure E.94: RAOs at MP9 for $L_R = 0.1$m and draft 0.14m. Dashed lines in (a) show how estimates of natural periods of 1st sloshing mode(left) and piston mode(right) compare

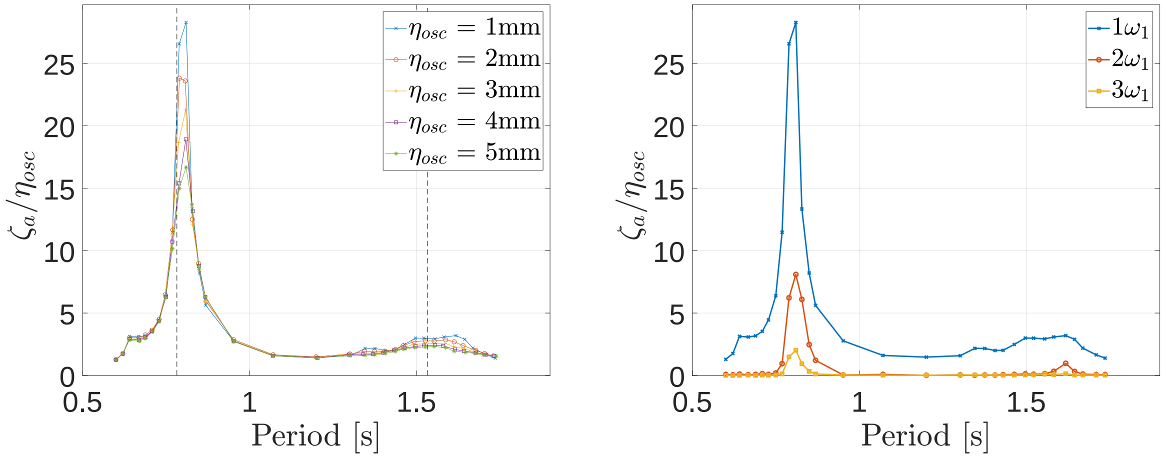

(a) RAO for all forcing amplitudes.

(b) Three first harmonics, with $\eta_{osc} = 0.001$m.

Figure E.95: RAOs at MP9 for $L_R = 0.15$m and draft 0.14m. Dashed lines in (a) show how estimates of natural periods of 1st sloshing mode(left) and piston mode(right) compare

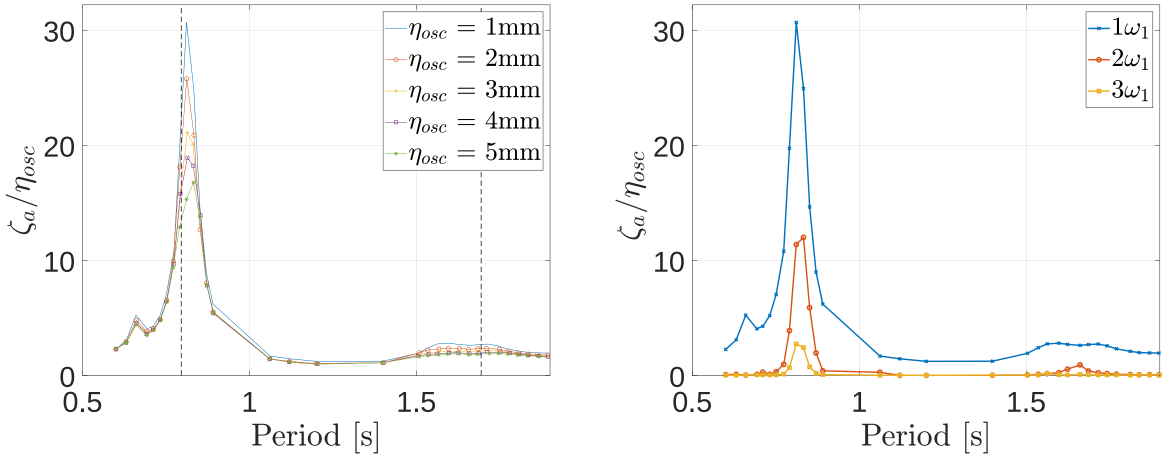

(a) RAO for all forcing amplitudes.

(b) Three first harmonics, with $\eta_{osc} = 0.001$m.

Figure E.96: RAOs at MP9 for $L_R = 0.2$m and draft 0.14m. Dashed lines in (a) show how estimates of natural periods of 1st sloshing mode(left) and piston mode(right) compare

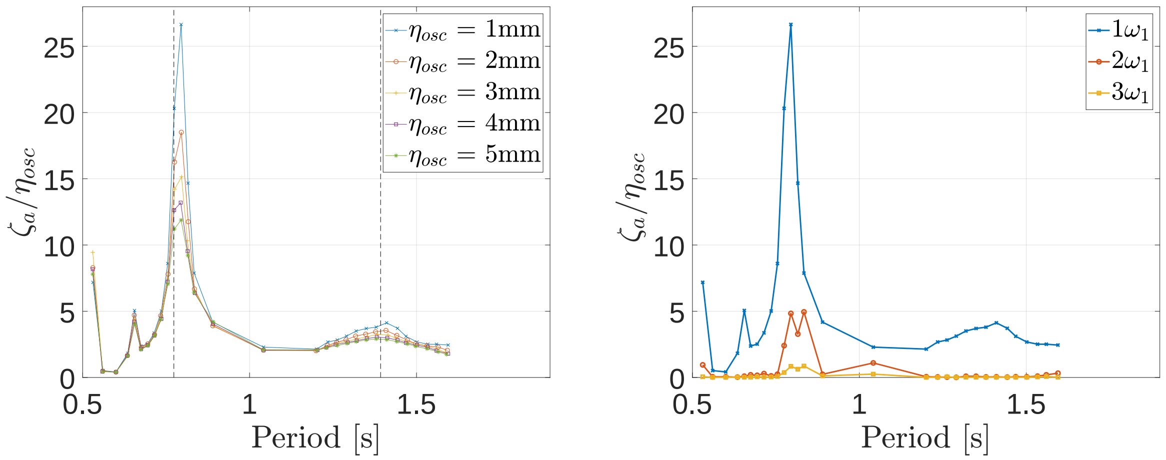

(a) RAO for all forcing amplitudes.

(b) Three first harmonics, with $\eta_{osc} = 0.001$m.

Figure E.97: RAOs at MP9 for $L_R = 0.1$m and draft 0.12m. Dashed lines in (a) show how estimates of natural periods of 1st sloshing mode(left) and piston mode(right) compare

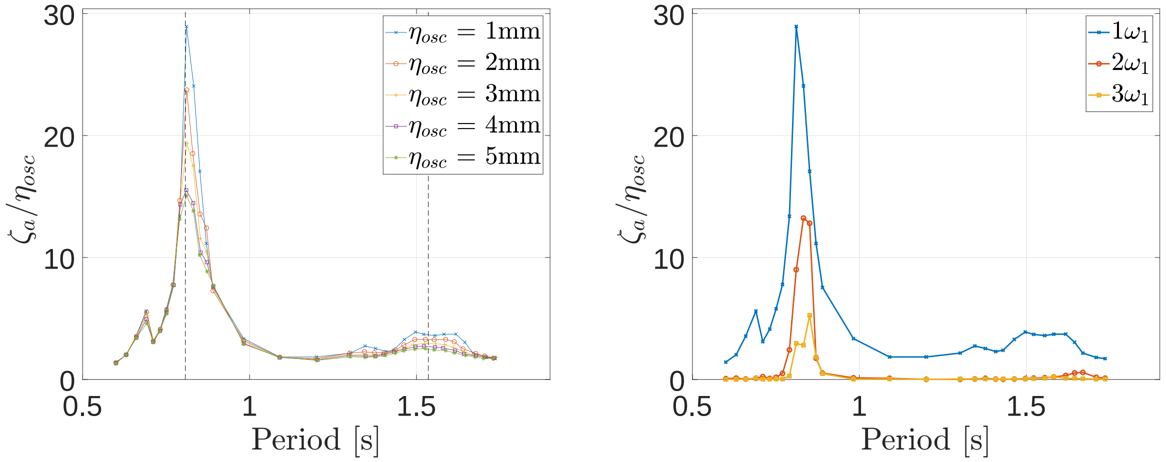

(a) RAO for all forcing amplitudes.

(b) Three first harmonics, with $\eta_{osc} = 0.001$m.

Figure E.98: RAOs at MP9 for $L_R = 0.15$m and draft 0.12m. Dashed lines in (a) show how estimates of natural periods of 1st sloshing mode(left) and piston mode(right) compare

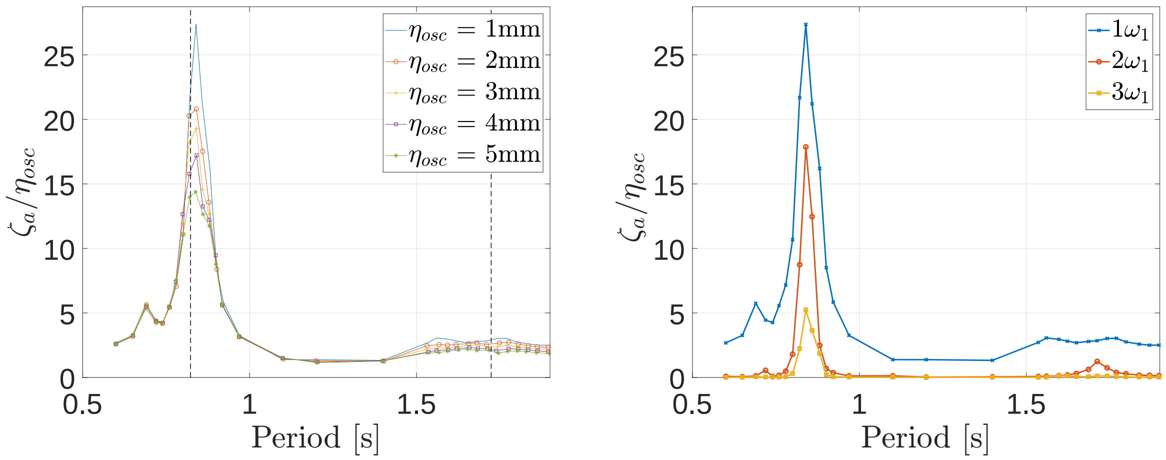

(a) RAO for all forcing amplitudes.

(b) Three first harmonics, with $\eta_{osc} = 0.001$m.

Figure E.99: RAOs at MP9 for $L_R = 0.2$m and draft 0.12m. Dashed lines in (a) show how estimates of natural periods of 1st sloshing mode(left) and piston mode(right) compare

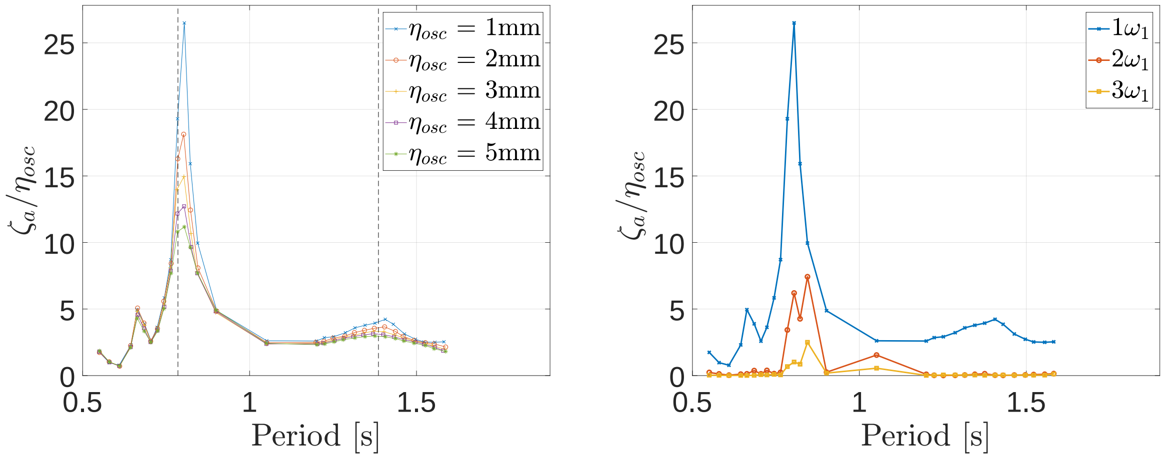

(a) RAO for all forcing amplitudes.

(b) Three first harmonics, with $\eta_{osc} = 0.001$m.

Figure E.100: RAOs at MP9 for $L_R = 0.1$m and draft 0.11m. Dashed lines in (a) show how estimates of natural periods of 1st sloshing mode(left) and piston mode(right) compare

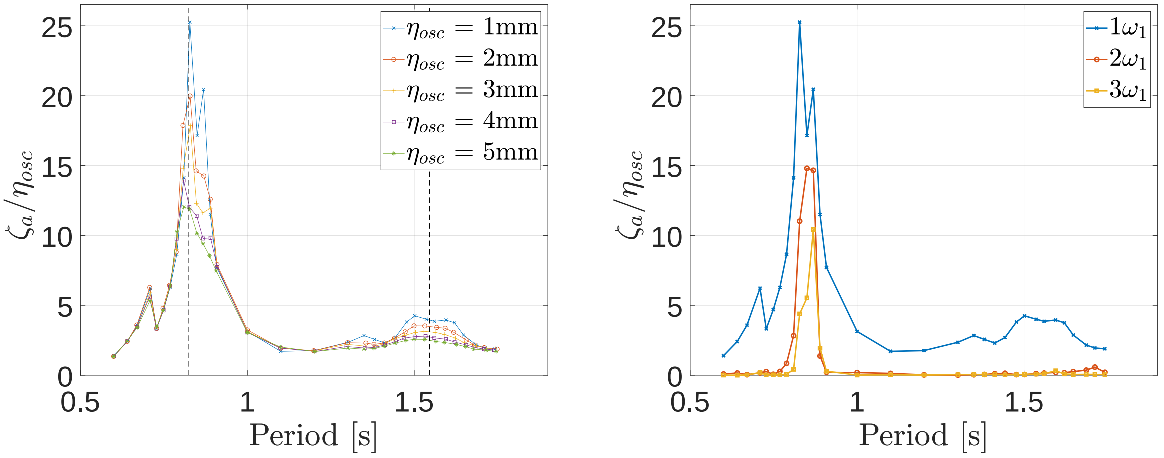

(a) RAO for all forcing amplitudes.

(b) Three first harmonics, with η_{osc} = 0.001m.

Figure E.101: RAOs at MP9 for L_R = 0.15m and draft 0.11m. Dashed lines in (a) show how estimates of natural periods of 1st sloshing mode(left) and piston mode(right) compare

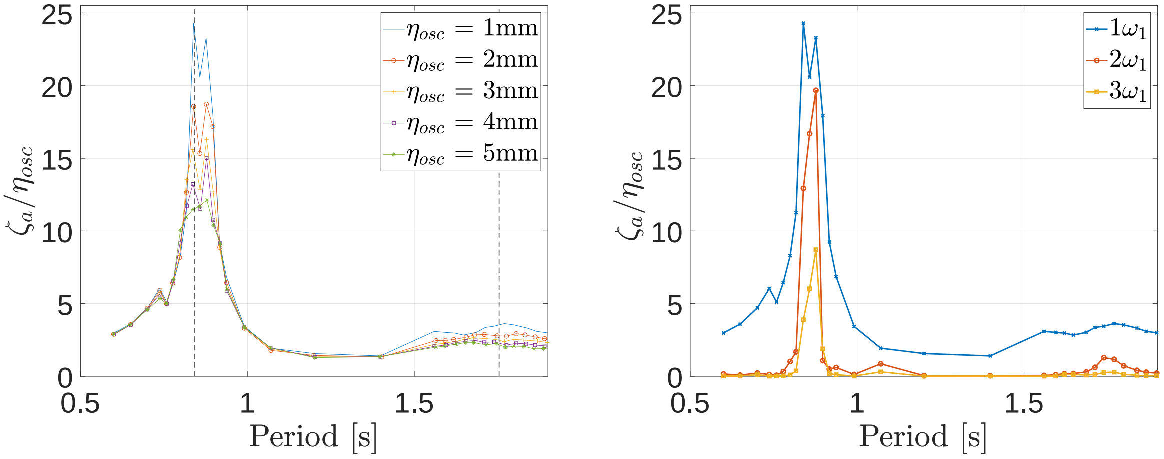

(a) RAO for all forcing amplitudes.

(b) Three first harmonics, with η_{osc} = 0.001m.

Figure E.102: RAOs at MP9 for L_R = 0.2m and draft 0.11m. Dashed lines in (a) show how estimates of natural periods of 1st sloshing mode(left) and piston mode(right) compare

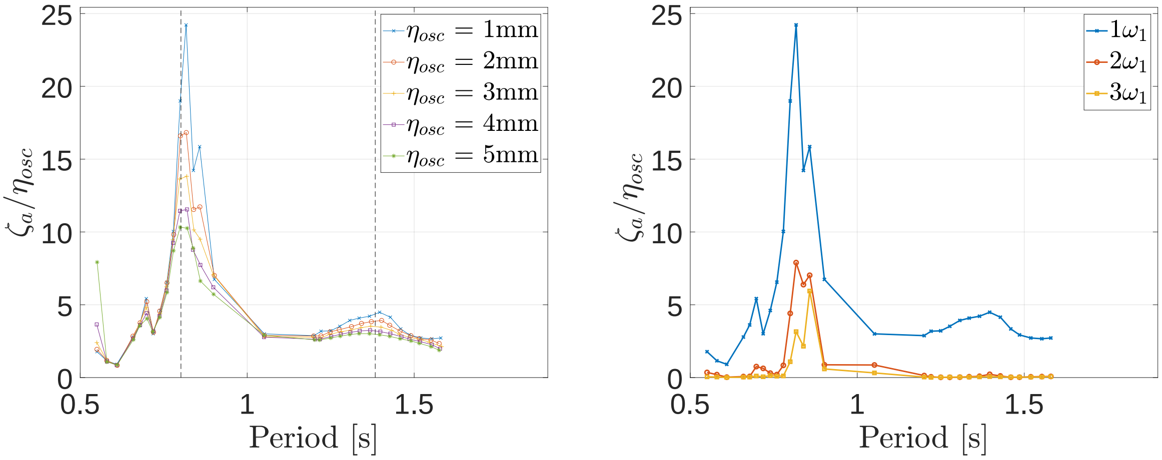

(a) RAO for all forcing amplitudes.

(b) Three first harmonics, with $\eta_{osc} = 0.001$m.

Figure E.103: RAOs at MP9 for L_R = 0.1m and draft 0.10m. Dashed lines in (a) show how estimates of natural periods of 1st sloshing mode(left) and piston mode(right) compare

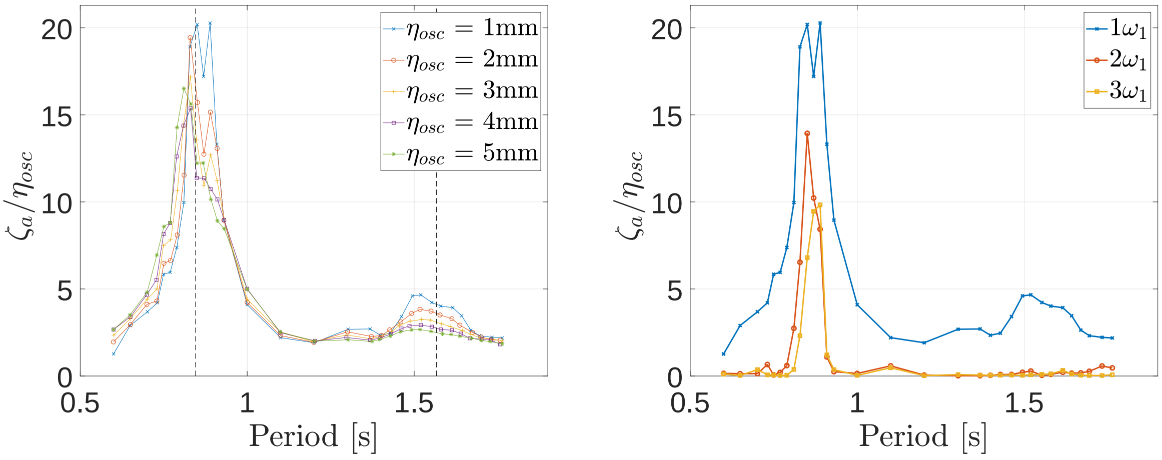

(a) RAO for all forcing amplitudes.

(b) Three first harmonics, with $\eta_{osc} = 0.001$m.

Figure E.104: RAOs at MP9 for L_R = 0.15m and draft 0.10m. Dashed lines in (a) show how estimates of natural periods of 1st sloshing mode(left) and piston mode(right) compare

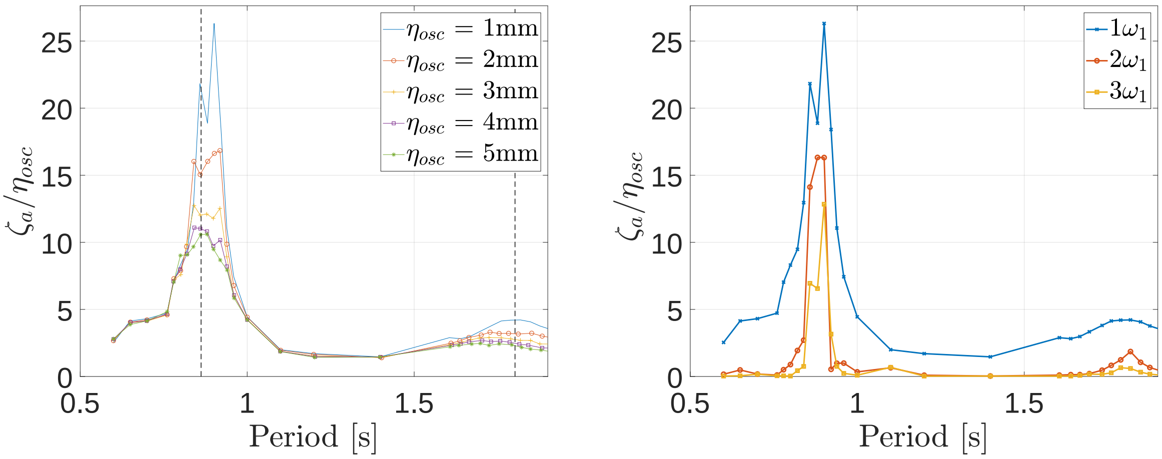

(a) RAO for all forcing amplitudes.

(b) Three first harmonics, with $\eta_{osc} = 0.001$m.

Figure E.105: RAOs at MP9 for $L_R = 0.2$m and draft 0.10m. Dashed lines in (a) show how estimates of natural periods of 1st sloshing mode(left) and piston mode(right) compare